UC Riverside

UC Riverside Electronic Theses and Dissertations

Title

Synthesis and Integration of Nanostructured Carbon: Carbon Nanotube-Polymer Nanocomposites and Graphene

Permalink

https://escholarship.org/uc/item/16386018

Author

Gulotty, Richard Stephen

Publication Date

2014

Peer reviewed|Thesis/dissertation

eScholarship.org Powered by the California Digital Library
University of California

UNIVERSITY OF CALIFORNIA
RIVERSIDE

Synthesis and Integration of Nanostructured Carbon: Carbon Nanotube-Polymer Nanocomposites and Graphene

A Dissertation submitted in partial satisfaction
of the requirements for the degree of

Doctor of Philosophy

in

Materials Science and Engineering

by

Richard Stephen Gulotty

December 2014

Dissertation Committee:
Dr. Alexander A. Balandin, Chairperson
Dr. Anirudha V. Sumant
Dr. Masaru Rao

The Dissertation of Richard Stephen Gulotty is approved by:

_____

_____

_____

Committee Chairperson

University of California, Riverside

ACKNOWLEDGEMENT

The text and figures of this dissertation, in part or in full, is a reprint or adaptation of the material as it appears in:

1. [Gulotty, R.; Castellino, M.; Jagdale, P.; Tagliaferro, A.; Balandin, A. A. Effects of Functionalization on Thermal Properties of Single-Wall and Multi-Wall Carbon Nanotube-Polymer Nanocomposites. *ACS Nano* **2013**, *7*, 5114–5121.] M. Castellino, P. Jagdale, and A. Tagliferro provided technical expertise, measuring the electrical characteristics and fabricating CNT-polymer composite samples. A. A. A. Balandin, who is listed in this publication, directed and supervised the research.
2. [Gulotty, R.; Das, S.; Liu, Y.; Sumant, A. V. Effect of Hydrogen Flow during Cooling Phase to Achieve Uniform and Repeatable Growth of Bilayer Graphene on Copper Foils over Large Area. *Carbon* **2014**, *77*, 341–350.] S. Das provided technical expertise in device fabrication. Y. Liu provided technical expertise in TEM and SAED. A. V. Sumant, who is listed in this publication, directed and supervised the research.
3. [Das, S.; Gulotty, R.; Sumant, A. V; Roelofs, A. All Two-Dimensional, Flexible, Transparent, and Thinnest Thin Film Transistor. *Nano Lett.* **2014**, *14*, 2861–2866.] S.Das designed and conducted e-beam lithography for fabrication of the devices, as well as performing electrical characterization of the devices. A. V. Roelofs and A. V. Sumant, who are listed in this publication directed and supervised the research.

As required by the copyright holder of these research articles, the copyright holder is acknowledged in each individual chapter where the material appears. Additional figures taken from already published material not attributed to the author of this dissertation are addressed individually where they appear according to the specifications of the copyright holder's agreements.

I would like to thank my research advisor Professor Alexander A. Balandin for his tremendous support and encouragement during my time in the MS&E Ph.D. program at UC-Riverside. He showed great interest in my development as an independent researcher in the Nano-device Laboratory (NDL). He gave me the opportunity to pursue research projects that best matched my interests and encouraged me to pursue and develop my own research goals, even when it lead to working outside NDL. My ability to conduct research independently was made more effective through his continuous attention to my research methodology and evaluation of my results and analysis. He provided me with the opportunities that helped me develop confidence in presenting my research. I will surely recall my experience with him at NDL as I continue my career as a research scientist.

I would also like to thank Dr. Anirudha Sumant and Prof. Masaru Rao for serving on my PhD Dissertation committee. Their contributions are helpful to my research. I would like to thank Dr. Sumant in addition for his time and effort during my appointment at Argonne National Laboratory (ANL). His guidance and supervision was instrumental in my research work there. I appreciate the financial support from the U.S. Department of

Energy, the Semiconductor Research Corporation (SRC) and the Defense Advanced Research Project Agency (DARPA) through FCRP Center for Function Accelerated nanoMaterial Engineering (FAME). I would like to thank the Carbon Group at Polytechnic of Turin for their collaboration with the fabrication and electrical measurements of the CNT-polymer composite samples, as well as the staff at the Center for Nanoscale Materials at Argonne National Laboratory for their support in the graphene synthesis research, as well as the staff at the Center for Nanoscale Science and Engineering and Central Facility for Advanced Microscopy and Microanalysis at UCR for their expertise and support. I am also thankful to my professors of the MS&E Ph.D. program at UC-Riverside.

I am thankful to my fellow members of NDL, as well as my mentors and colleagues at ANL and UCR for their guidance. In particular my sincere gratitude and thanks goes out to Dr. Saptarshi Das, Dr. Daniel Rosenmann, Dr. Sheng Tong, Dr. David Czaplewski, Alfredo Bobadilla, Dr. David Gosztola, Dr. Diana Berman, Dr. Ralu Divan, Dr. Il Woong Jung, Dr. Yuzi Liu, Suzanne Miller, Dr. Guanxiong Liu, Dr. Zhong Yan, Dr. Jie Yu, Dr. Vivek Goyal, Dr. Craig Nolen, Dr. Desalegne Teweldebrhan, Dr. Zahid Hossain, Dr. Khan M. Farhan Shahil, Dr. Jacqueline Renteria, Dr. Pradyumna Goli, and Davil Garcia.

Finally, I would like to thank my family for their love and support.

To my family

ABSTRACT OF THE DISSERTATION

Synthesis and Integration of Nanostructured Carbon:
Carbon Nanotube-Polymer Nanocomposites and Graphene

by

Richard Stephen Gulotty

Doctor of Philosophy, Graduate Program in Materials Science and Engineering
University of California, Riverside, December 2014
Dr. Alexander A. Balandin, Chairperson

Nanostructured carbon, in the form of tubes or sheets, exhibits exceptional thermal and electrical properties. Graphene, a single atomic sheet of hexagonal sp^2 bonded carbon, possesses a thermal conductivity higher than diamond, with an extremely high electron mobility. Carbon nanotubes (CNT), which are tubes composed of one or more graphene sheets, also possess high thermal conductivity and electron mobility. One of the major problems facing the application of nanomaterials is integration into already existing material systems. A second challenge is controlled synthesis of nanomaterials. In this dissertation research novel methods were investigated for coupling carbon nanotubes to polymer matrices, as well as new approaches for controlling the synthesis of graphene and reduced graphene oxide like carbon (R-GOC) on copper (Cu) foils *via* chemical vapor deposition. It was determined that carboxylic functionalization of carbon nanotubes was effective in improving the coupling of CNTs to polymer matrices, affecting the thermal transport of the resulting CNT-polymer nanocomposites. From the CVD studies it was established that the cooling phase gases flowed after deposition influence the

growth mechanics of graphene on Cu foil. Further CVD studies showed that methane may be decomposed directly onto quartz to form reduced graphene oxide like carbon thin films. The obtained thermal characterization results are important for development of CNTs as fillers for composite pastes with high thermal conductivity, and the results of the CVD studies are important for developing further understanding of growth mechanics of bilayer graphene and other nanostructured carbon. In addition to the fundamental study of CVD synthesis of graphene and R-GOC, this dissertation work includes engineering of graphene and R-GOC to various applications, including the development of the thinnest flexible transistor with active materials made from all-2D materials, as well as large-scale electron transparent windows, and transparent conducting thin films.

Table of Contents

ACKNOWLEDGEMENT.....iii

ABSTRACT OF THE DISSERTATION.....vii

Table of Contents.....ix

List of Figures.....xiii

Chapter 1. Introduction and Overview.....1

1.1 Introduction.....1

1.2 Overview.....4

REFERENCES AND NOTES.....5

Chapter 2. Studying the Effect of Carboxylic Functionalization of CNTs to Achieve CNT--Polymer Nanocomposite TIMs with Enhanced Thermal Conductivity 6

2.0 Abstract.....6

2.1 Introduction.....7

2.2 Experimental Methods.....10

2.3 Results of the Experiments.....11

2.4 Discussion.....18

2.5 Conclusions.....23

2.6 Summary.....23

2.7 Acknowledgements.....24

REFERENCES AND NOTES.....25

Chapter 3. Study of Graphene CVD Process to Synthesize Misoriented Bilayer Graphene …….....29

3.0 Abstract.....29

3.1 Introduction.....29

3.2 Experimental Methods.....31

3.3 Results of the Experiments.....35

3.4 Discussion.....50

3.5 Conclusions.....55

3.6 Acknowledgements.....55

REFERENCES AND NOTES.....57

Chapter 4. CVD Synthesis of Large Area Uniform R-GO like Carbon Films with Excellent Thermal and Electrical Conductivity and Optical Transparency 61

4.0 Abstract.....61

4.1 Introduction.....62

4.2 Experimental Methods.....66

4.3 Results of the Experiments.....69

4.4 Discussion.....80

4.5 Conclusions.....81

4.6 Acknowledgements.....81

REFERENCES AND NOTES.....83

Chapter 5. Engineering of CVD Graphene to Achieve All 2D Flexible, Transparent, and Thinnest Thin Film Transistor.....87

5.0 Abstract.....87

5.1 Introduction.....88

5.2 Experimental Methods.....89

5.3 Results of the Experiments.....91

5.4 Discussion.....103

5.5 Conclusions.....105

5.6 Acknowledgements.....105

REFERENCES AND NOTES.....107

Chapter 6. Engineering of CVD Graphene and R-GOC Films to Achieve Large Area Atomically Thin Free Standing Membranes for RF-Injector Windows.....110

6.0 Abstract.....110

6.1 Introduction.....111

6.2 Experimental Methods.....114

6.3 Results of the Experiments.....115

6.4 Discussion.....124

6.5 Conclusions.....133

6.6 Acknowledgements.....133

REFERENCES AND NOTES.....134

Conclusion.....137

REFERENCES AND NOTES 138

Appendices.....139

Appendix A.....139

List of Figures

Figure 1.1 Illustrations of atomic structure of graphene and carbon nanotube.....2

Figure 1.2 Optical images of mechanically exfoliated graphene back-gated field effect transistors.....2

Figure 2.1 Illustration of heat-sink TIM substrate interfaces and cross-section view of heat dissipation system.....8

Figure 2.2 Photograph of CNT – polymer composites and sample stage used in LFT experiments. Depiction of carboxylic groups attached to the side-wall of SW-CNT.....13

Figure 2.3 Scanning electron microscopy image of epoxy-based nanocomposite with 3 wt % of MW-CNTs (sample #14).....15

Figure 2.4 Thermal conductivity of the epoxy-based nanocomposites with functionalized and unfunctionalized SW-CNT and MW-CNT (fillers # 3, 6, 7 and 8) at 3 wt% loading fraction.....16

Figure 2.5 Thermal conductivity of PDMS with and without filler #7 at 3 wt% and epoxy composites with filler #16 at 1 and 3 wt%.....17

Figure 2.6 Thermal conductivity of epoxy-based nanocomposites with SW-CNTs and MW-CNTs of different lengths.....19

Figure 2.7 Thermal conductivity enhancement factor for epoxy composite samples as a function of the outer diameter of the MW-CNT filler at two different loading fractions of the fillers.....20

Figure 2.8 Electrical conductivity vs. the thermal conductivity enhancement for the epoxy based NCs with the functionalized and neat SW-CNT and MW-CNT fillers at 1 and 3 wt% loading fraction.....21

Figure 3.1 Bilayer graphene electron energy band diagrams unperturbed (pristine) and gated (perpendicular applied field).....32

Figure 3.2 Optical image of few-layer graphene chemical vapor deposited on nickel.....32

Figure 3.3 Photos of CVD system and 30 cm x 30 cm foils in CVD furnace tube. Process parameters for hydrogen cooling experiment.....33

Figure 3.4 Raman spectra of vacuum-cooled (single-layer) and hydrogen-cooled (bilayer) graphene on Cu by 442 nm excitation. SEM images of hydrogen-cooled bilayer and vacuum-cooled single layer graphene grown on 3 cm x 5 cm Cu foil (scale bars, 30 μm).....36

Figure 3.5 Raman spectra of single-layer and bilayer graphene on SiO_2 (514 nm excitation). Stitched optical image maps of hydrogen-cooled (bilayer) graphene and vacuum-cooled (single-layer) graphene on SiO_2 substrate. SAED of single-layer and bilayer graphene. Line profile plot of single-layer graphene SAED.....38

Figure 3.6 Histograms for 2D/G peak intensity ratio and 2D peak FWHM from Raman spectroscopy map of vacuum-cooled (single-layer) and hydrogen-cooled (bilayer) graphene on Cu with 442 nm excitation.....40

Figure 3.7 Spatial Raman spectroscopy maps of vacuum-cooled single-layer and hydrogen-cooled bilayer graphene on Cu.....41

Figure 3.8 Spatial Raman spectroscopy of vacuum-cooled single-layer and hydrogen-cooled bilayer graphene transferred to SiO_2.....42

Figure 3.9 Histograms for hydrogen-cooled (bilayer) and vacuum-cooled (single-layer) graphene transferred to SiO_2.....43

Figure 3.10 SEM image and 3-D cartoon of a prototype GFET. Plots of output and transfer characteristics of vacuum-cooled (single-layer) and hydrogen-cooled (bilayer) graphene GFETs. The table shows the calculated average carrier mobilities and the current ON-OFF ratios of the devices.....45

Figure 3.11 Graphene device channel characteristics for single and bilayer graphene on SiO_2.....47

Figure 3.12 Visible light transmittance of vacuum-cooled (single-layer) and hydrogen-cooled (bilayer) graphene transferred to quartz microscope slides.....48

Figure 3.13 Photo of 30 cm x 30 cm (~1 ft x 1 ft) Cu foil after hydrogen-cooled CVD process. Typical Raman spectra from the large area samples with 442 nm excitation. Histograms of Raman characteristics of the hydrogen-cooled CVD processed 30 cm x 30 cm foils.....49

Figure 3.14 Illustration of the vacuum-cooled single-layer and hydrogen-cooled bilayer graphene growth mechanism.....54

Figure 4.1 SEM images of aggregated few-layer R-GO produced by Hummers method.....64

Figure 4.2 Optical image of blank quartz substrate and R-GOC films on quartz and SiO_2 substrates. Line plot of film thickness with deposition time.....65

Figure 4.3 AFM of R-GOC film.....70

Figure 4.4 Comparison of visible transmittance and sheet resistance of CVD R-GOC films with literature values of ITO.....70

Figure 4.5 UV-visible light transmittance of R-GOC film on quartz.....71

Figure 4.6 Typical Raman spectra of R-GOC films suspended in air on TEM grids. Optical image of R-GOC film suspended on Cu TEM grid.....72

Figure 4.7 TEM, SAED, and EELS of R-GOC films. Table 4.1 gives the sp^3 content of the R-GOC films extracted from the EELS.....74

Figure 4.8 Normalized NEXAFS spectra of R-GOC films. Table 4.2 gives the sp^3 and relative integrated area of π^* C=O bond peaks of the R-GOC films as measured from the C-K and O-K edges.....75

Figure 4.9 XPS survey scan of R-GOC film.....77

Figure 4.10 In-plane thermal conductivity of R-GOC-Cu composites.....78

Figure 4.11 Optothermal Raman data for R-GOC film suspended on Cu TEM grid.....79

Figure 4.12 Optical images of R-GOC film on 100 mm fused silica wafer.....80

Figure 5.1 False color SEM image, 3D cartoon, and cross sectional view of an all 2D TFT with graphene as metal electrode, h-BN as gate dielectric and WSe_2 as the semiconducting channel material.....93

Figure 5.2 Back gate transfer characteristics of a WSe_2 TFT with graphene contact electrodes at the source and drain. Inset is the cross section diagram of the device.....94

Figure 5.3 Back gate transfer characteristics of a graphene FET with WSe_2 layer underneath. Inset shows colorized SEM image of the device and cross section diagram of the device.....95

Figure 5.4 Band alignment at graphene to WSe_2 contact interface.....96

Figure 5.5 Top gate transfer characteristics of all 2D TFT corresponding to V_{BG} = 10 V and -10 V.....98

Figure 5.6 Optical images of thinnest FET on flexible PET substrate and experimental setup to measure strain effect.....99

Figure 5.7 Transfer characteristics of the FET on flexible PET substrate.....100

Figure 5.8 Output characteristics of the FET on flexible PET substrate.....101

Figure 5.9 Transfer characteristics of the FET on flexible PET substrate with and without strain.....102

Figure 5.10 Transparency of WSe_2 flakes, and thinnest FET on flexible PET substrate in the visible light range.....103

Figure 6.1 Optical images of graphene membranes transferred to stainless steel without treatment and after solvent cleaning 116

Figure 6.2 Raman spectra of graphene membrane with varying degrees of solvent treatment.....117

Figure 6.3 Plot of pressure gauge readings of each chamber with transmission intensity of the laser during a differential pressure test of clean bilayer graphene membrane.....120

Figure 6.4 Optical images of graphene membrane on stainless steel aperture after differential pressure testing was completed, differential pressure and helium leak rate testing setup.....121
Figure 6.5 Optical image of bilayer graphene membrane supported by PMMA.....122
Figure 6.6 Optical images of Cu foils with extended 30 minute hydrogen anneal at 800 °C with ramp to deposition in hydrogen, without the annealing, and corresponding graphene membranes fabricated from the films on Si aperture and stainless steel aperture.....122
Figure 6.7 Optical images of R-GOC membranes transferred to apertures of various dimensions. Optical image of ablation tested R-GOC membrane.....123
Figure 6.8 Spatial Raman maps of 325nm ablated R-GOC film and typical Raman spectra (inset optical image of ablated film).....124
Figure 6.9 Helium leak rate simulation 2D surface map of PMMA + graphene membrane cross section 1 s after He is introduced, surface concentration line plot of "Helium-free side" for 0.5 mm diameter PMMA + graphene membrane 1 s after He is introduced....127
Figure 6.10 Mechanical simulation of strain distribution in PMMA-supported bilayer graphene during differential pressure test.....129
Figure 6.11 Mechanical simulation of strain distribution in the connecting edge of the PMMA-supported bilayer graphene during differential pressure test (1 mm diameter, 220 nm thickness.....130

Figure 6.12 Mechanical simulation of stress at maximum strain (2%) in the connecting edge of the PMMA-supported bilayer graphene during differential pressure test (1 mm diameter, 220 nm thickness).....131

Chapter 1. Introduction and Overview

1.1 Introduction

A nanostructured material is conventionally defined as a material that possesses at least one structural dimension that is nanoscale (less than a tenth of a micron in size).[1] Nanostructured materials, or nanomaterials, have not reached full technological implementation due to the difficulties encountered in synthesizing nanomaterials in a controlled, scalable way, as well as difficulties with integrating nanomaterials into already existing material systems while maintaining their attractive characteristics.

Graphene, a form of nanostructured carbon, is a monolayer of hexagonally packed carbon atoms. When graphene is folded into a tube shape with a nanoscale diameter, the structure is called a carbon nanotube (see Fig. 1.1).

Graphene was first synthesized by Novoselov and Geim[2] by the mechanical exfoliation of highly oriented pyrolytic graphite (HOPG) onto a silicon dioxide substrate with a tuned oxide thickness. Mechanical exfoliation forces apart the HOPG using adhesive tape repeatedly until a significant number of few layer sheets are produced. The HOPG fractures along the planar direction, where individual single atomic layers of 2D hexagonal crystals of carbon (i.e. graphene) are held by Van der Waals bonding. These flakes are then rubbed against an oxide substrate with a specially tuned thickness, typically 300 nm, so that the approximate layer number may be inferred from the color contrast of the flakes. Electron beam lithography may be used to define contacts to the

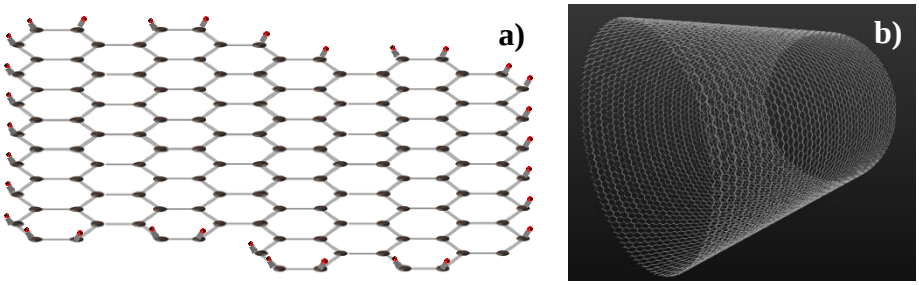


Figure 1.1. Illustrations of atomic structure of graphene (a), and carbon nanotube (b). The graphene and CNT in this figure are edge terminated by hydrogen. Both graphene and CNT are composed of carbon with 2D hexagonal crystal structure.

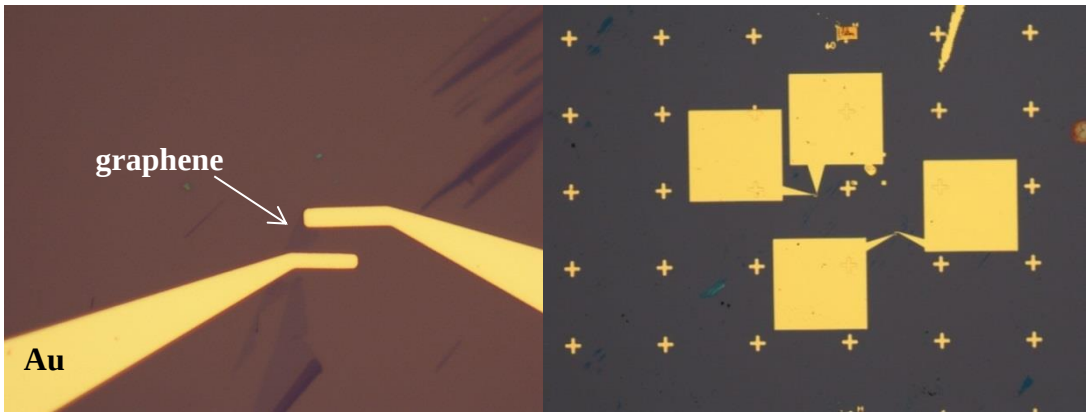


Figure 1.2. Optical images of mechanically exfoliated graphene back-gated field effect transistors. Contacts are electron beam deposited Ti/Au. This device had a low electron mobility compared to suspended graphene, only ~800 cm^2/V-s for electrons.

individual flakes, where the graphene may be used as a channel material for field effect transistors (see Fig. 1.2). Unfortunately, the carrier mobilities of the mechanically exfoliated flakes on SiO_2 do not approach the ideal suspended value.

Suspended graphene has demonstrated remarkable electrical,[3] mechanical,[4] optical,[5] and thermal properties.[6] But mechanical exfoliation is not a scalable method for producing high-quality graphene in significant quantities for actual applications as the placement

and layer number of the graphene is not well controlled. Another factor hindering application of graphene is difficulty in integrating the graphene in such a way that is not deleterious to its properties. For example, supported graphene has substantially lower thermal conductivity[7] and carrier mobility[3] than suspended graphene. Carbon nanotubes (CNTs) have superior electrical,[8] mechanical,[9] and thermal properties,[10] as they are composed of carbon with the same 2D hexagonal crystal structure as graphene.

In terms of improving placement and layer number control of graphene, controlled and sustainable processes for large-scale high-quality graphene synthesis have been pursued since the discovery of graphene. To that end, chemical vapor deposition (CVD) has been studied extensively and much progress has been achieved towards large-scale single layer graphene synthesis, but synthesis of large area uniform bilayer or trilayer graphene has not been achieved in a fast process. Like graphene, large scale fabrication of CNTs has been achieved via CVD, but further study is required to achieve wall number and chirality uniformity.

Both graphene and CNTs encounter difficulty in technological implementation, even after large-scale controlled synthesis has been achieved. For example, successful coupling of CNTs to the polymer matrix has yet to be demonstrated, and as a result CNT-polymer nanocomposite thermal interface materials have not reached their full potential. For CVD synthesized graphene, the removal of the graphene from the copper substrate, followed by the polymer handle assisted transfer, cause degradation and contamination, which in turn negatively affects the electrical and thermal properties of the graphene film.

1.2 Overview

This dissertation will describe research that addresses some areas in synthesis and technical application of nanostructured carbon materials. In chapter 2, thermal interface materials will be introduced as an engineering application of nanostructured carbon, and experiments on the effect of carboxylic functionalization of CNTs on the thermal properties of CNT-polymer nanocomposites will be described in detail. In chapter 3, graphene will be introduced as an important nanostructured carbon material for various applications, and experiments on the synthesis of large area misoriented bilayer graphene on copper will be discussed, with detailed description of characterization methods to identify layer number uniformity and methods to achieve layer number uniformity of graphene via conventional thermal CVD. In chapter 4, experiments on the synthesis and characterization of reduced graphene oxide like carbon thin films is described. In chapter 5, engineering of CVD Graphene as a contact material for flexible transparent all 2D thin film transistors is described in detail, with electrical characteristics and optical transparency results for the fabricated devices. In chapter 6, engineering of CVD graphene as atomically thin helium impermeable membranes for RF photoinjector windows is reported.

REFERENCES AND NOTES

(1) Moriarty, P. Nanostructured Materials. *Reports Prog. Phys.* **2001**, *64*, 297–381.

(2) Geim, A. K.; Novoselov, K. S. The Rise of Graphene. *Nat. Mater.* **2007**, *6*, 183–191.

(3) Bolotin, K. I.; Sikes, K. J.; Jiang, Z.; Klima, M.; Fudenberg, G.; Hone, J.; Kim, P.; Stormer, H. L. Ultrahigh Electron Mobility in Suspended Graphene. *Solid State Commun.* **2008**, *146*, 351–355.

(4) Lee, C.; Wei, X.; Kysar, J. W.; Hone, J. Measurement of the Elastic Properties and Intrinsic Strength of Monolayer Graphene. *Science* **2008**, *321*, 385–388.

(5) Wang, X.; Zhi, L.; Müllen, K. Transparent, Conductive Graphene Electrodes for Dye-Sensitized Solar Cells. *Nano Lett.* **2008**, *8*, 323–327.

(6) Balandin, A. A.; Ghosh, S.; Bao, W.; Calizo, I.; Teweldebrhan, D.; Miao, F.; Lau, C. N. Superior Thermal Conductivity of Single-Layer Graphene. *Nano Lett.* **2008**, *8*, 902–907.

(7) Seol, J. H.; Jo, I.; Moore, A. L.; Lindsay, L.; Aitken, Z. H.; Pettes, M. T.; Li, X.; Yao, Z.; Huang, R.; Broido, D.; et al. Two-Dimensional Phonon Transport in Supported Graphene. *Science (80-.).* **2010**, *328*, 213–216.

(8) Berger, C.; Yi, Y.; Wang, Z. L.; Heer, W. A. De. Multiwalled Carbon Nanotubes Are Ballistic Conductors. *Appl. Phys. A* **2002**, *74*, 363–365.

(9) Ma, P.-C.; Siddiqui, N. A.; Marom, G.; Kim, J.-K. Dispersion and Functionalization of Carbon Nanotubes for Polymer-Based Nanocomposites: A Review. *Compos. Part A Appl. Sci. Manuf.* **2010**, *41*, 1345–1367.

(10) Lee, J.; Varshney, V.; Roy, A. K.; Farmer, B. L. Single Mode Phonon Energy Transmission in Functionalized Carbon Nanotubes. *J. Chem. Phys.* **2011**, *135*, 104109.

Chapter 2. Studying the Effect of Carboxylic Functionalization of CNTs to Achieve CNT--Polymer Nanocomposite TIMs with Enhanced Thermal Conductivity

2.0 Abstract

Surface functionalization such as carboxylic functionalization (-COOH) has been shown to improve the dispersion of carbon nanotubes and reduce the electrical resistivity of carbon-nanotube—polymer nanocomposites. The effects of this type of functionalization on the thermal conduction through the nanocomposites is described in this chapter. It was found that larger loading fractions (~3 wt%) are required to enhance the thermal conductivity of the nanocomposites compared to the loading fraction required to reduce the electrical resistivity (~1wt%). Multi-wall carbon nanotubes performed the best after functionalization compared to other carbon nanotube fillers in terms of achieving enhanced thermal conduction and electrical conductivity simultaneously. The functionalization of the single-wall carbon nanotubes reduced the thermal enhancement compared to neat single-wall carbon nanotube nanocomposites. The functionalization increases coupling between the carbon nanotube and matrix, but this effect is accompanied by defect formation, which causes acoustic phonon scattering. The obtained results have an impact on engineering application of carbon nanotubes and graphene flakes as fillers for improving thermal and electrical properties of composites.

2.1 Introduction

Thermal interface materials (TIMs) are engineered to bridge the thermal barrier between the heat-sink and the integrated circuit heat spreader (ICHS). The equation of thermal resistance

$$R_{sys} = \frac{t}{kA} + R_1 + R_2 \qquad (1)\,[1]$$

may be used to describe the influence of the thermal conductivity of the TIM on the overall thermal resistance R_{sys} of the heat dissipation system in Fig. 2.1b.[1] In eq 1, *t* is the thickness of the polymer nanocomposite TIM layer, *k* is the thermal conductivity of the polymer nanocomposite TIM layer, and R_1 and R_2 are the interfacial resistances at the TIM-heat-sink and TIM-ICHS boundaries (see Fig. 2.1a) . It is clear that *k* improvement is a key target for reducing the thermal resistance of the heat dissipation system and increasing the effectiveness of heat dissipation.

Many conventional TIMs are composed of polymeric material or grease filled with silver, alumina, SiC, or BN particles. These fillers are effective, but expensive compared to the polymer, and large volume fractions ~50-70% are required to achieve the desired high thermal conduction (~ 1-5W/m-K). The volume fraction is may defined in terms of wt % using eq (2).

$$V_{filler} = \frac{W_{filler}}{[W_{filler} + \left(\rho_{matrix}/\rho_{filler}\right) * (1 - W_{filler})]} \qquad (2)$$

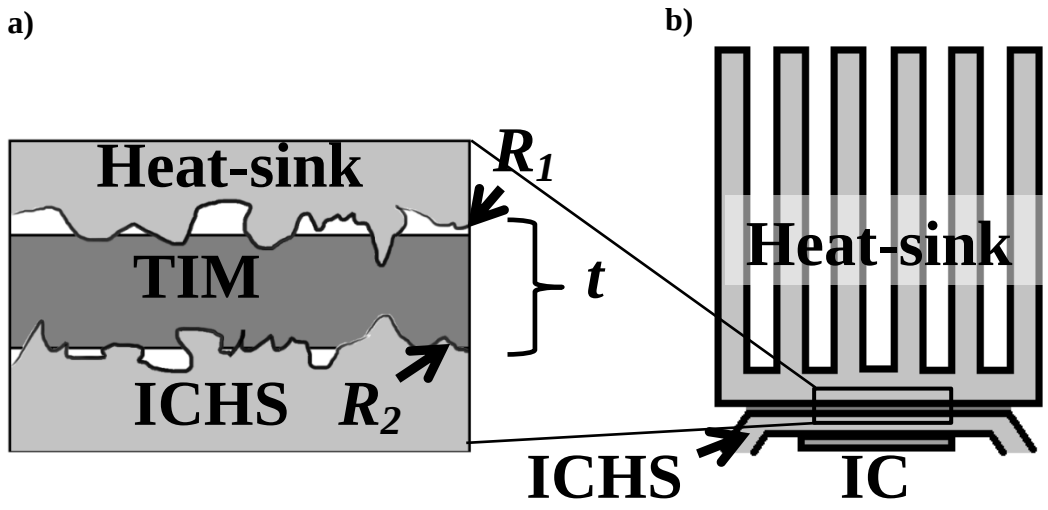


Figure 2.1. Illustration of heat-sink TIM substrate interfaces as pertains to eq (1) (a), © 2006 IEEE. Reprinted (adapted), with permission, from [Sarvar, F. C.; Whalley, D.; Conway, P. P. Thermal Interface Materials- A Review of the State of the Art. *Proceedings of the 2006 Electronics System Integration Technology Conference IEEE* 2006.] [2] The TIM adheres the metallic heat-sink to the ICHS . Cross-section view of heat dissipation system, (b) © 2006 IEEE. Reprinted (adapted), with permission, from [Prasher, R. Thermal Interface Materials: Historical Perspective, Status, and Future Directions. *Proceedings IEEE* 2006.] [1]

Where V_{filler} is the volume fraction of filler (in this case the filler is the alumina, silver, or other high conductivity material), W_{filler} is the weight fraction of filler, ρ_{matrix} is the density of the matrix (in this case the matrix is the polymeric material), and ρ_{filler} is the density of the filler.[3]

Carbon nanotubes (CNTs) and graphene are attractive as additives in nanocomposite (NC) TIM materials due to their high intrinsic electrical conductivity,[4,5] σ, thermal conductivity,[6,7] *K*, and mechanical strength.[8,9] Introducing these nanostructured carbon materials should theoretically result in an enhancement in the average σ and *K* at small loading fractions. Indeed, it was demonstrated that CNTs improved the σ of polymers by

many orders of magnitude[10] at low volume fractions of loading ~0.1 vol. %, as compared to 20-30 vol.% for metal filler additives.[11,12]

Reports on the *K* enhancement with the addition of CNT are less consistent. There have been studies reporting *K* enhancements of 50-250% at 7 vol. % of the CNT loading,[13–15] while in other cases, *K* was not improved[16] or even decreased with addition of single wall CNTs (SW-CNTs).[16] This may be because the CNTs do not couple well with the polymeric matrix material. The thermal boundary resistance (TBR) between CNTs and polymer may be as high as ~10^{-7} m^2KW^{-1}. The large TBR can be attributed to the Kapitza resistance, which is derived from the large difference in phonon density of states between the CNT and the polymer. It has also been suggested that the CNTs may not be able to achieve thermal percolation, or a continuous heat path, and thus the composite *K* suffers.

The dispersion of the CNTs within the polymer matrix is also important to achieve *K* enhancement, and chemical functionalization has been considered a possible route for achieving this goal.[17,18] Chemical functionalization may improve the coupling at the CNT-polymer interface leading to enhanced σ or *K* of the NCs. However, chemical functionalization may have different effects on different tube types, and may even be detrimental to the intrinsic transport properties of the nanostructured carbon.

In section 2.2, experiments to study the effect of carboxylic functionalization (-COOH groups) of the CNTs on the thermal properties of the resulting carbon-nanotube—polymer NCs are described. The carboxylic functionalization of CNTs was previously shown to improve the electrical properties of polymer NCs.[19] The thermal properties of

the CNT—polymer NCs result from an interplay between improved CNT—polymer coupling and degraded intrinsic *K* of functionalized CNTs.

2.2 Experimental Methods

Several different types of CNT fillers were procured from Nanothinx. The desired quantity of filler was mixed into liquid epoxy resin (or silicone rubber) and stirred vigorously (1.2 krpm for 10 min.). Ultrasonication was applied (37kHz for 15 minutes) to help remove gas pockets from the mixture. The voids were completely removed by degassing in vacuum. The resulting mixture was poured into a mold for oven curing (70°C for 4 h).

The laser flash technique (LFT) was employed to measure the heat capacity and diffusivity of the CNT—polymer NCs. In LFT the bottom of the sample is illuminated by the flash of a xenon lamp. A cryogenically cooled InSb IR detector monitors the temperature of the top of the sample. The thermal diffusivity, α, is extracted by interpreting the transient temperature curve. The thermal conductivity, *K* (W/m-K), is calculated from the equation

$$K = \alpha \rho c_p \qquad (3)$$

where ρ is the mass density of the material (kg/m^3) and c_p the specific heat (J/kg-K). The specific heat of each sample was obtained from laser flash calorimetry (LFC).[20] The temperature rise of the sample of interest is compared to a reference sample of known heat capacity and similar thermo-physical properties. In this case the neat epoxy with no CNT filler was used as reference. The sample and the reference are assumed to absorb equal amounts of energy from equal light flashes because they are treated with graphite

spray and were fabricated the same methods and have similar surface roughnesses. The LFT system was calibrated using pyroceram and copper and returned values within ± 5% of the literature value in each case. Further details of LFT and LFC have been described elsewhere.[20–22]

Table 2.1.

Sample #	Filler type	Diameter (nm)	Length (μm)	Purity (weight %)
1	Multi-Wall	30-50	10-20	> 95
2	Multi-Wall	< 8	10-30	> 95
3	Short Thin MW	9.5	1.5	> 95
4	Single-Wall	1-2	5-30	> 90
5	Single-Wall	1-2	0.5-2	> 90
6	Single-Wall	2	several	> 70
7	-COOH Functional SW	2	several	> 70
8	-COOH Functional MW	9.5	1.5	> 95
14	Multi-Wall	18-35	>10	97
15	Multi-Wall	25-45	>10	98.5
16	Multi-Wall	6-10	>10	>90

2.3 Results of the Experiments

Polydimethylsiloxane (PDMS) is a silicone rubber which is widely used for bio-applications and as thermal interface materials (TIMs). Epoxy resin is a thermoset polymer utilized in the automobile industry and as a TIM. These two polymeric materials were prepared with the SW-CNT and MW-CNT filler at different weight fractions. A summary of the filler types and associated sample names is given in Table 2.1. As may be

seen in the Table 2.1, the prepared composites contained various carbon materials as fillers, including SW-CNTs and MW-CNTs with variable diameter and length. For the purpose of determining the effects of carboxylic functionalization on thermal properties of CNT-polymer composites, a set of SW-CNTs and MW-CNTs were subjected to carboxylic (-COOH) functionalization before addition to the composites, while others were added as grown (see Table 2.1). The amount of nanostructured carbon added was varied from 0 to 3 wt %. Fig. 2.2a) shows CNT-polymer NCs prepared for LFT and LFC analysis. The samples are 12 mm diameter and 1-2 mm thick.

A single crystal SW-CNT is composed of a hexagonal crystal lattice of sp^2 bonded carbon. The structure has high intrinsic *K* (~3000 W/m-K) at 22 ºC.[23] The strong carbon bonds in CNTs allow acoustic phonons to carrier heat effectively, and these phonons dominate the thermal conduction in all CNTs. Only graphene has a higher *K* than CNTs.[7,24,25] In practice, CNTs contain defects. MW-CNTs have a larger radius of curvature than SW-CNTs, and this creates a lower in-plane strain. The strain is large enough to cause defect formation in SW-CNTs due to their smaller radius of curvature. During the functionalization, the oxidation occurs at the defects. It is expected that SW-CNTs would have more sidewall functionalization sites than the MW-CNT due to their inherently higher defect density.[19,26] The functionalization can adversely affect the electronic properties of CNTs,[4] and with only one wall, the effect can be more dramatic on SW-CNTs. MW-CNTs may redistribute current among unaffected walls. Carboxylic functionalization reduces the hydrophobicity of the CNTs, improving the dispersion of

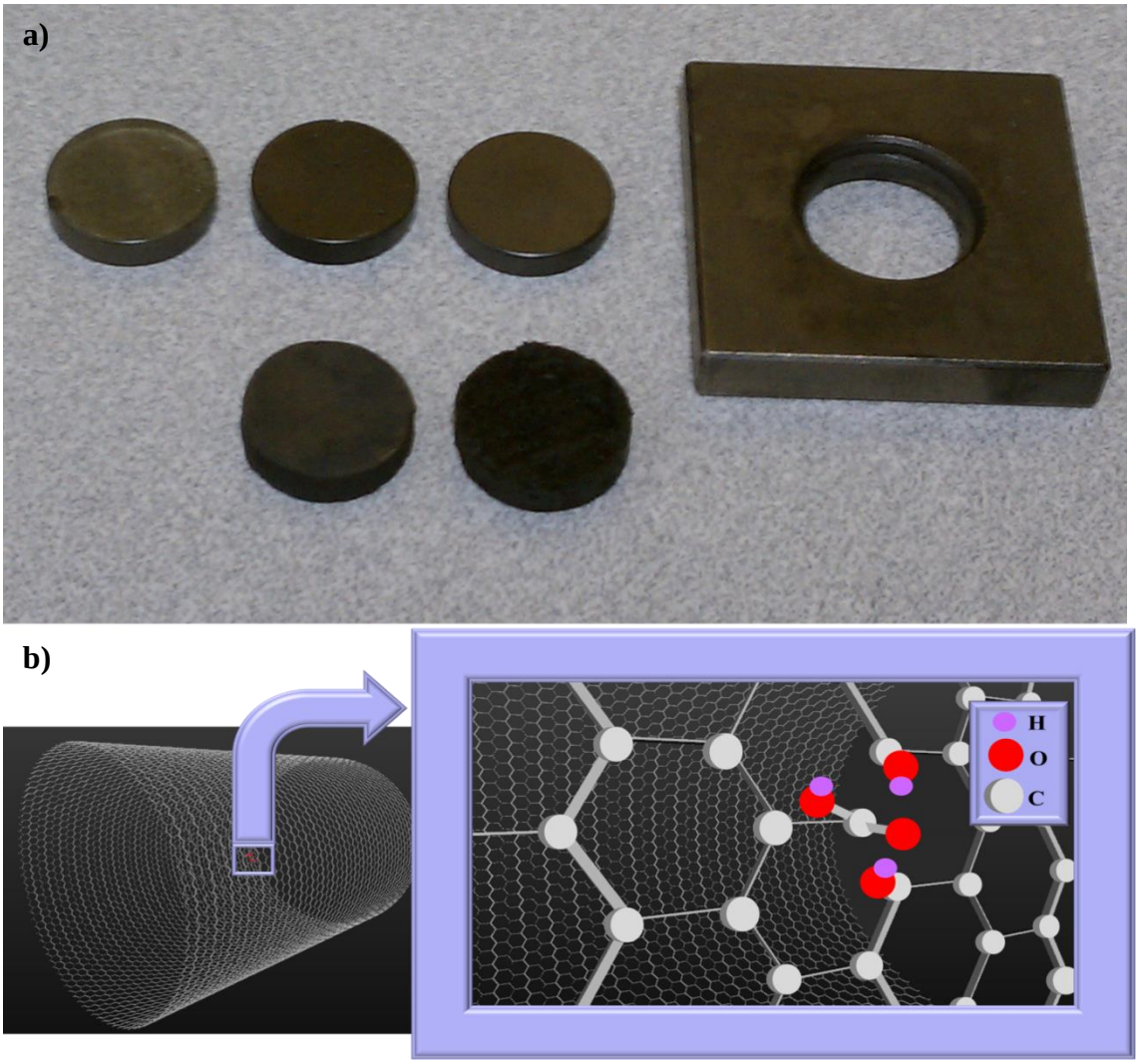


Figure 2.2. (a) Photograph of CNT – polymer composites and sample stage used in LFT experiments. (b) Depiction of carboxylic groups attached to the side-wall of SW-CNT. The new bond interrupts the continuous hexagonal crystal lattice of the CNT. While increasing the CNT – matrix coupling, the attachment of functionalized groups creates scattering centers for acoustic phonons carrying heat in CNTs.

necessarily disrupts the crystal structure of the CNTs, forming sp^3 bonds that act as scattering centers for acoustic phonons propagating along the length of the CNTs (see Fig. 2.2b).

Polymer NCs prepared by the same method with the same CNT filler types were observed to have isotropic electrical properties. From this it was inferred that the CNTs are uniformly dispersed without orientation.[17,18] The dispersion and misorientation of the CNTs was confirmed via electron microscopy (see Fig. 2.3). The effect of introducing CNTs (SW-CNT or MW-CNT) on the σ of the NCs was dramatic, an increase from essentially insulating (~10^{-11} S/cm) to 6×10^{-7} S/cm at 3 wt% SW-CNT (filler #6) and 10^{-5} S/cm and 2×10^{-2} S/cm at 1 and 3 wt% MW-CNT (filler #3), respectively. The effect of carboxylic functionalization depended on the CNT type. For MW-CNT NCs the σ increased by a factor of 7 at 1 wt% filler and by an additional ~20% at 3 wt% filler when carboxylic functionalization is applied (relative to MW-CNT NCs with unfunctionalized CNTs of the same type), whereas σ increased by 34% at 1 wt% filler but decreased by a factor of ~3 at 3 wt% filler when carboxylic functionalization is applied (relative to SW-CNT NCs with unfunctionalized CNTs of the same type).[27,28]

The cross-plane *K* of the CNT—polymer NCs were performed using LFT. Figure 2.4 shows *K* as a function of temperature for the neat epoxy, NC with SW-CNT (filler #6), NC with functionalized SW-CNT (filler #7), NC with MW-CNT (filler 3) and NC with functionalized MW-CNT (filler #8). In Fig. 2.4 all NCs had 3 wt% of the CNT filler. The addition of as grown SW-CNTs to the epoxy enhances *K* by ~25%. Functionalization is detrimental to the *K* of the SW-CNT fillers. The thermal conductivity drops almost to the neat epoxy value. This suggests that the improvement in heat conduction caused by increasing the SW-CNT coupling to the polymer was outweighed by the impediment to

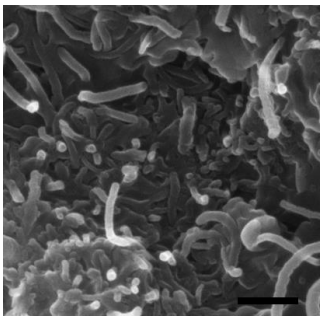


Figure 2.3. Scanning electron microscopy image of epoxy-based nanocomposite with 3 wt % of MW-CNTs (sample #14) showing the random orientation of CNTs. The scale bar in the image is 300 nm.

acoustic phonon transport along the SW-CNT caused by the introduction of sidewall defects that occurs during the functionalization. The addition of neat MW-CNTs enhances the *K*, but not as strongly as neat SW-CNTs. Functionalization of the MW-CNTs does not produce a noticeable effect on *K*. The latter can indicate that the contribution of the outer wall to the heat conduction in MW-CNTs is marginal and the heat transport occurs through the inside walls, which are not affected by the defects created by functionalization on the outer wall. It is illustrative to compare the functionalization effect on thermal and electrical properties of the NCs to achieve the optimal combination of properties. For the NC with 3 wt% loading of SW-CNT (filler #7), functionalization reduced the *K* and decreased the σ. However at 3 wt% loading of MW-CNT (filler #8), the functionalization had little effect on the *K* while increasing the σ by an additional ~20% compared to the unfunctionalized MW-CNT of the same type.

The SW-CNT with functionalization (filler #7) was added to PDMS. The *K* characterization results are given in Fig. 2.5 with epoxy with 1 and 3 wt% MW-CNT (filler #16) added for comparison of the *K* enhancement magnitude. The Results of this plot are in line with expectations; the addition of larger wt% filler results in larger *K*

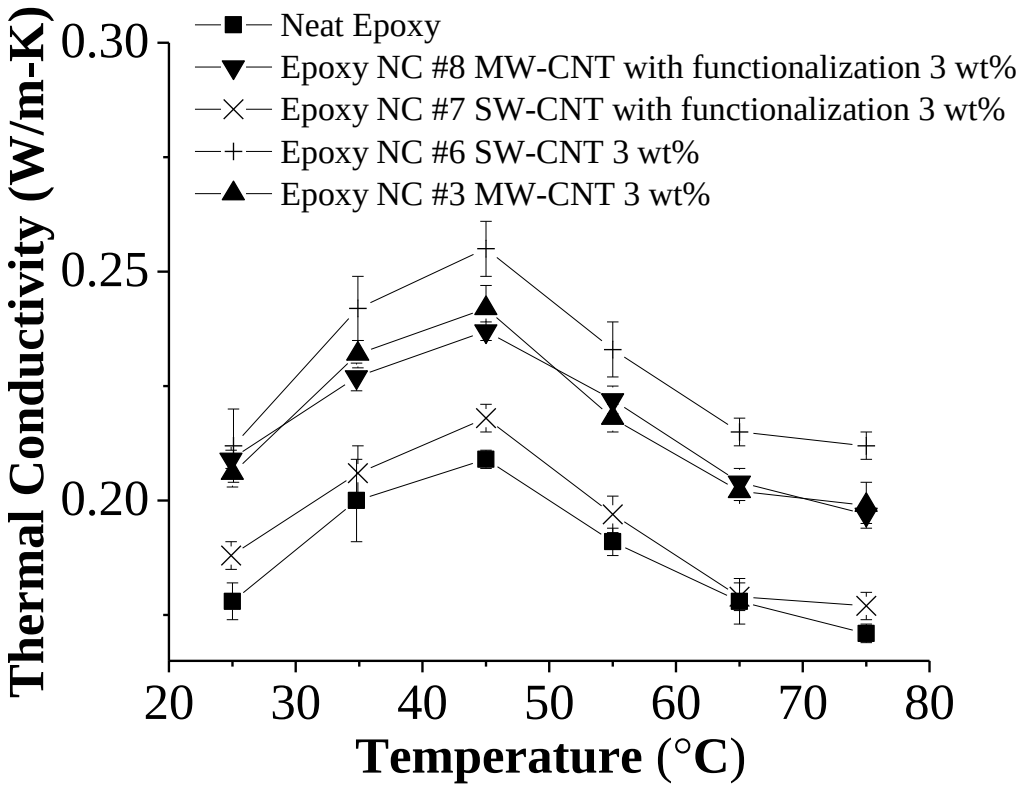


Figure 2.4. Thermal conductivity of the epoxy-based nanocomposites with functionalized and unfunctionalized SW-CNT and MW-CNT (fillers # 3, 6, 7 and 8) at 3 wt% loading fraction. Note that functionalization produces little effect on the *K* in case of MW-CNT filers. The *K* enhancement is degraded by functionalization of SW-CNT fillers.

enhancement. The PDMS NCs show higher *K* than epoxy, as the neat *K* is intrinsically higher than the epoxy value. The observed temperature dependent *K* is a reflection of the non-monotonic heat capacity dependence of the epoxy. The specific heat of epoxy can change with temperature owing to the loss of the water absorbed from the ambient or additional curing during heating. The epoxy tends to absorb more water than PDMS, saturating at 1.5-6 wt%.[29] The thickness of the samples is sufficiently small to allow for humidity absorption during the sample storage. The effect of the absorbed water on

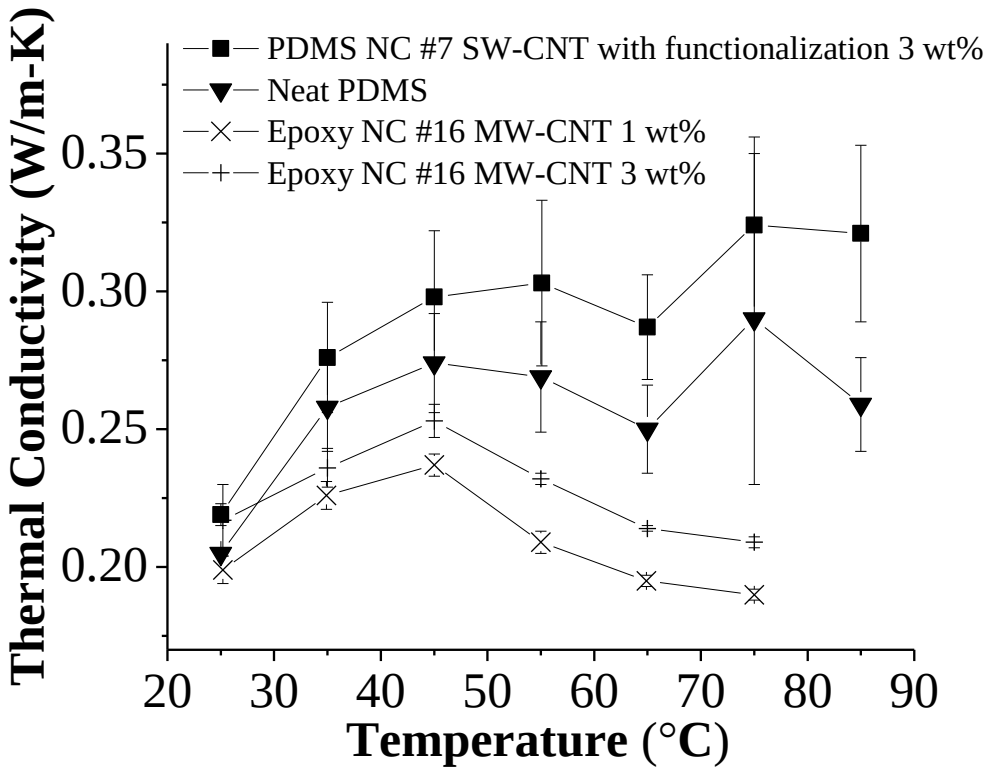


Figure 2.5. Thermal conductivity of PDMS with and without filler #7 at 3 wt% as a function of temperature. The thermal conductivity of epoxy composites with 1 and 3 wt% filler #16 is also plotted for comparison.

properties varies with the chemistry of the epoxy resin and hardener. The loss of water during the LFT and LFC at elevated temperature would lower the specific heat, resulting in a valley around 65-75 °C. The specific heat of PDMS increases more monotonically with increasing temperature in comparison with epoxy.

In Fig. 2.6, the effect of length of the as-grown CNT on *K* of resulting epoxy NC is illustrated . The weight fraction in the NCs are all 3 wt%. The "long" SW-CNTs (filler #4) show stronger *K* enhancement than "short" SW-CNTS (filler #5) (See Fig. 2.6a). The same trend is observed for the MW-CNTs presented in Fig. 2.6b. There is an order of

magnitude difference in the CNT length between "short" and "long" CNTs. The length, *L*, to diameter, *D*, ratio *L/D* was ~10^4 for the "long" SW-CNTs and ~10^3 for the "short" SW-CNTs. In the case of the "long" MW-CNTs, the *L/D* was above ~10^3 for "long" and ~10^2 for "short". The Longer CNTs with larger *L/D* are more efficient in improving the heat conduction properties of CNT—polymer NCs. This conclusion is supported by the calculations reported for MW-CNT NCs using the Hatta-Taya model for randomly distributed fibers.[30]

Figure 2.7 shows the *K* enhancement as a function of diameter, *D*, at two different MW-CNT loading fractions. The trend indicates that larger *D* is beneficial for enhanced *K* of MW-CNT-polymer NCs. It was found that the enhancement trend depends more on diameter of the filler rather than *L/D* ratio

2.4 Discussion

For certain engineering applications, it is important to identify which CNT fillers and loading fractions improve σ while also enhancing *K*. Figure 2.8 presents the σ data and our measured *K* enhancement for the epoxy-based NCs with as-grown SW-CNTs (filler#6), functionalized SW-CNTs (filler #7), as-grown MW-CNTs (filler #3), and functionalized MW-CNTs (filler #8). The results indicate that addition of 1 wt% of CNTs is not sufficient to improve *K* of epoxy NC and can result in degradation of *K*. Two data points with negative *K* enhancement are shown in Fig. 2.8. Four of the 11 tested fillers (sample #4, 5, 7, and 8) revealed a decrease in the average *K* at 1 wt% compared to the neat epoxy over the examined temperature range. It is interesting that in the epoxy NC

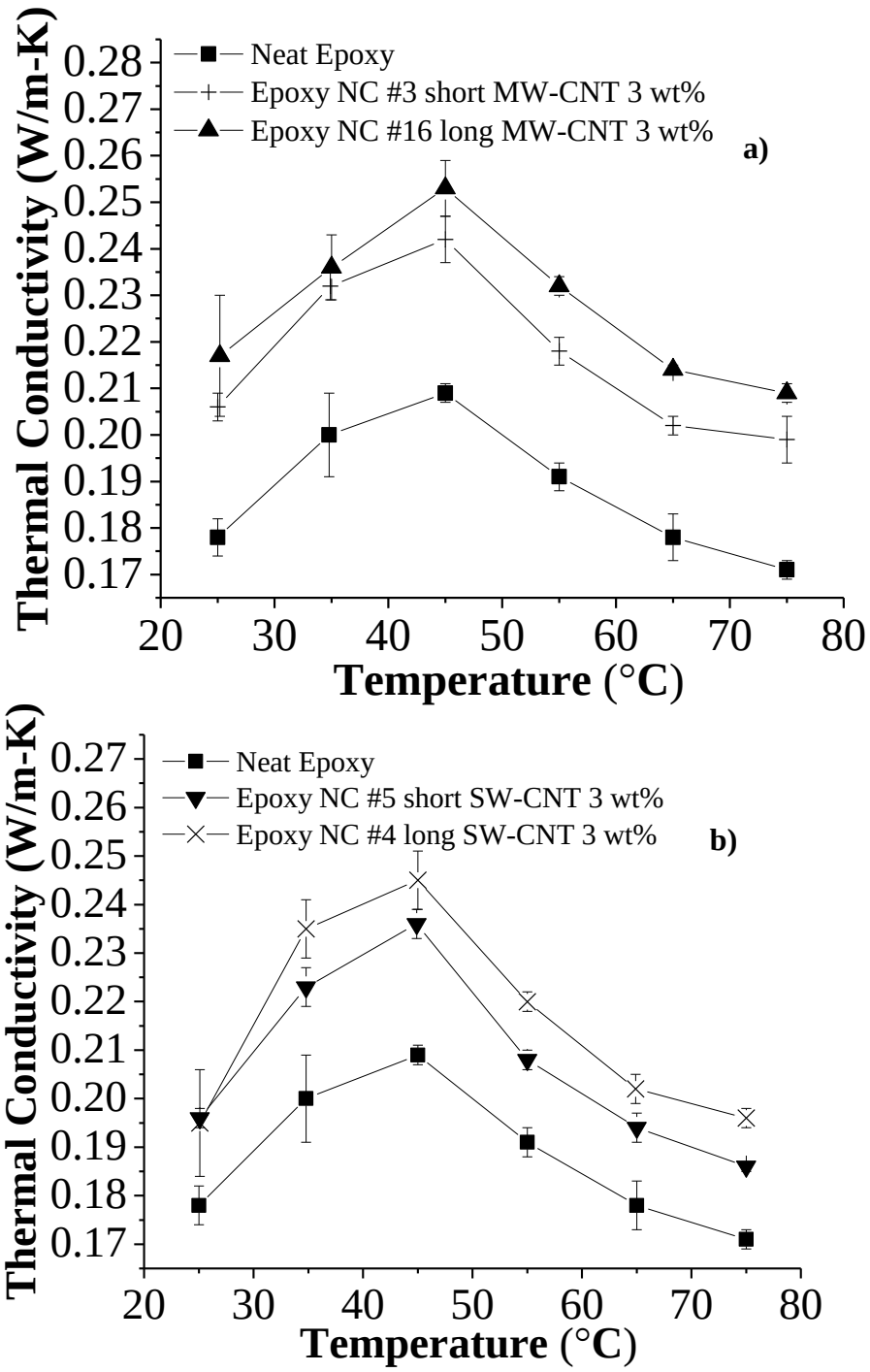


Figure 2.6. (a) Thermal conductivity of epoxy-based nanocomposites with SW-CNTs a) and MW-CNTs (b) of different lengths. Note that longer CNTs perform better in terms of the *K* enhancement in both cases.

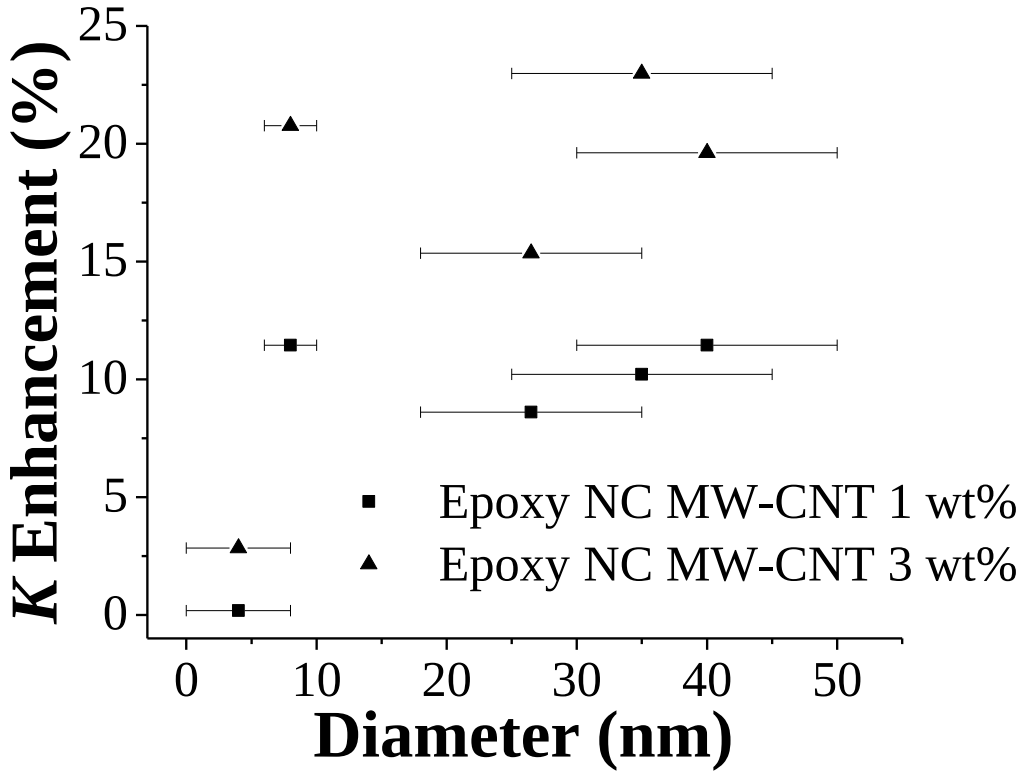


Figure 2.7. Thermal conductivity enhancement factor for epoxy composite samples as a function of the outer diameter of the MW-CNT filler at two different loading fractions of the fillers. Each pair of points with the same diameter on the graph corresponds to the same filler type. In order of increasing diameter the data points correspond to the fillers #2, #16, #14, #15 and #1, respectively.

with filler #8 MW-CNTs at 1 wt% improved σ substantially while slightly decreasing *K* relative to the neat epoxy. One can conclude from this data that in order to preserve or enhance *K* of CNT—polymer NCs the filler loading should be above 1 wt%, preferably closer to 3 wt%.

In addition, Fig. 2.8 shows that functionalization has a detrimental effect on the properties of the SW-CNTs. This may be because carboxylic functional groups improve

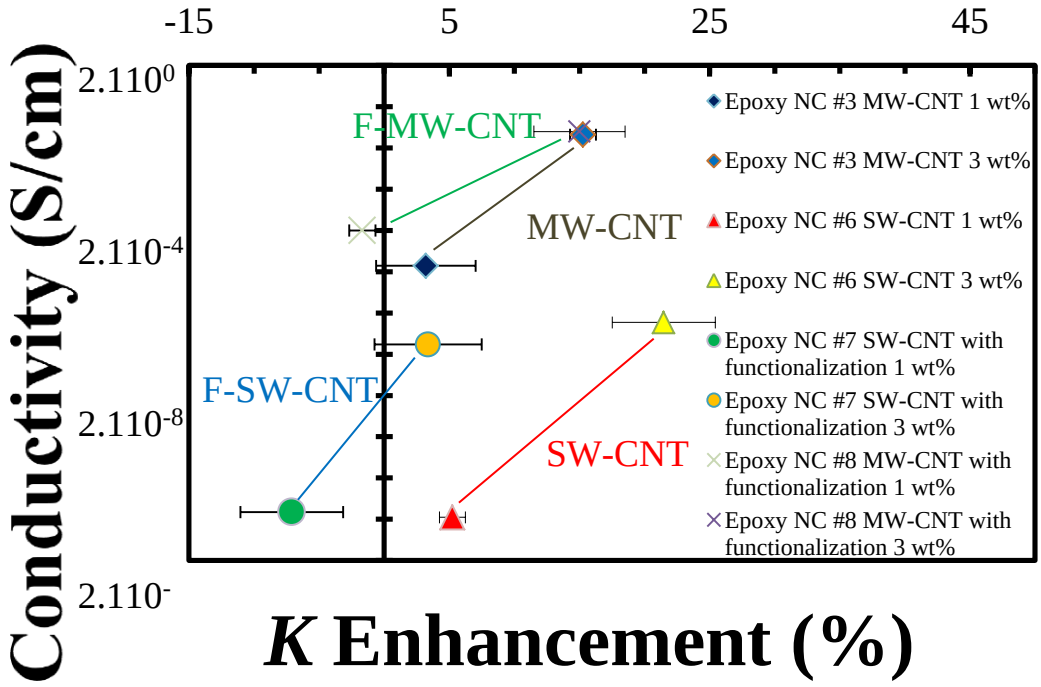


Figure 2.8. Electrical conductivity vs. the thermal conductivity enhancement for the epoxy based NCs with the functionalized and neat SW-CNT and MW-CNT fillers at 1 and 3 wt% loading fraction. The electrical conductivity is shown in the logarithmic scale. The data points correspond to the fillers # 3, 6, 7 and 8.

the SW-CNT coupling to the polymer matrix, but deteriorate the intrinsic thermal conductivity of the SW-CNT itself. The defects act as scattering centers for acoustic phonons that carry the bulk of the heat in all CNTs.[7,24,31] In the MW-CNT—polymer NCs, however, the functionalization improves coupling and σ without degrading *K*. In fact, the epoxy NC #8 with the functionalized MWCNT filler at 3 wt% loading demonstrated the highest σ of 25 mS/cm with *K* enhanced by 15%. The latter can be explained assuming that all walls contribute to the phonon transport. In this case the

increase in defectiveness of the external wall caused by functionalization leads to only a slight decrease in thermal conductivity overwhelmed by the decrease in thermal contact resistance due to functionalization. Thus, carboxylic functionalized MW-CNTs appear to be the optimum filler for the epoxy NCs when simultaneous enhancement of σ and K is desired.

The thermal conductivity cannot be improved simply by increasing the CNT wt% loading. At higher loading the CNTs clump and aggregate, and the mixing and dispersing of the filler becomes impossible. The solution to achieving higher K and σ lies in pursuing improved coupling of the CNT to the polymer matrix while maintaining the intrinsic phonon transport properties of the CNTs.

The results of these experiments cannot be directly compared to other studies due to differences in composition and preparation methods, but it is illustrative to discuss the data in context of prior studies.[26,32–34] Triethylenetetramine (TETA) grafting was observed to improve coupling between CNTs and epoxy and enhance the K and mechanical strength of the resulting NC.[26] Another study reported enhancement of a silicone with 2 vol% of MW-CNTs.[35] The CNT lengths in the silicone NC study were much shorter, resulting in much lower CNT-CNT distances. Our results correspond well with the data reported in Ref.[35] The thermal conductivity of purified SW-CNT—epoxy NCs using N, N-Dimethylformamide (DMF) suspension and surfactant stabilized aqueous SW-CNT suspensions revealed K enhancement at (~1 wt%),[32] however, the SW-

CNTs in that study were not subjected to functionalization, and were much shorter length than the CNT fillers characterized here.

2.5 Conclusions

The effect of carboxylic functionalization of CNTs on the *K* of polymer NCs were studied. It was found that *K* of polymers with functionalized CNTs is maintained or enhanced for MW-CNTs, while it is reduced for SW-CNTs. Thermal conductivity enhancement requires larger wt % loading than those needed for σ enhancement. Longer and larger diameter CNTs are more efficient for enhancing *K* of polymer NCs. The observed trends were concluded to be the result of differences in acoustic phonon transport in SW-CNTs and MW-CNTs after functionalization. Though the functionalization may increase the coupling between CNTs and the polymer matrix, it also causes surface defects which impede acoustic phonon transport. The MW-CNTs are less affected by the introduction of surface defects, maintaining their phonon transport through unaffected interior walls, whereas SW-CNTs are very sensitive to surface defects and the phonon transport is severely degraded by functionalization.

2.6 Summary

In this chapter, TIMs were introduced as an important part of the integrated circuit packaging system. A relatively new material filler, nanostructured carbon--in particular CNTs--were introduced as a filler material for TIM polymer NCs. Efforts to improve the coupling between the CNTs and the polymer matrix were described in detail, including experiments to characterize the thermal properties of functionalized SW-CNT and MWCNT epoxy and PDMS NCs.

2.7 Acknowledgements

Chapter 2 was reprinted (adapted) with permission from (Gulotty, R.; Castellino, M.; Jagdale, P.; Tagliaferro, A.; Balandin, A. A. Effects of Functionalization on Thermal Properties of Single-Wall and Multi-Wall Carbon Nanotube-Polymer Nanocomposites. *ACS Nano* **2013**, *7*, 5114–5121.). Copyright (2013) American Chemical Society. This work was performed at the Nano-device Laboratory at the University of California, Riverside.

REFERENCES AND NOTES

(1) Prasher, R. Thermal Interface Materials: Historical Perspective, Status, and Future Directions. In *Proceedings IEEE*; 2006; pp. 1571–1585.

(2) Sarvar, F. C.; Whalley, D.; Conway, P. P. Thermal Interface Materials- A Review of the State of the Art. In *Proceedings of the 2006 Electronics System Integration Technology Conference IEEE*; 2006; pp. 1292–1302.

(3) Callister, W. *Materials Science and Engineering: An Introduction*; 7th ed.; Wiley, 2006.

(4) Berger, C.; Yi, Y.; Wang, Z. L.; Heer, W. A. De. Multiwalled Carbon Nanotubes Are Ballistic Conductors. *Appl. Phys. A* **2002**, *74*, 363–365.

(5) Geim, A. K.; Novoselov, K. S. The Rise of Graphene. *Nat. Mater.* **2007**, *6*, 183–191.

(6) Fujii, M.; Zhang, X.; Xie, H.; Ago, H.; Takahashi, K.; Ikuta, T.; Abe, H.; Shimizu, T. Measuring the Thermal Conductivity of a Single Carbon Nanotube. *Phys. Rev. Lett.* **2005**, *95*, 065502.

(7) Balandin, A. A. Thermal Properties of Graphene and Nanostructured Carbon Materials. *Nat. Mater.* **2011**, *10*, 569–581.

(8) Yu, M.-F.; Files, B. S.; Arepalli, S.; Ruoff, R. S. Tensile Loading of Ropes of Single Wall Carbon Nanotubes and Their Mechanical Properties. *Phys. Rev. Lett.* **2000**, *84*, 5552–5555.

(9) Kim, Y.; Lee, J.; Yeom, M. S.; Shin, J. W.; Kim, H.; Cui, Y.; Kysar, J. W.; Hone, J.; Jung, Y.; Jeon, S.; et al. Strengthening Effect of Single-Atomic-Layer Graphene in Metal-Graphene Nanolayered Composites. *Nat. Commun.* **2013**, *4*, 2114.

(10) MacDiarmid, A. G. "Synthetic Metals": A Novel Role for Organic Polymers. *Angew. Chem. Int. Ed. Engl.* **2001**, *40*, 2581–2590.

(11) Felba, J. Thermally Conductive Nanocomposites. In *Nano-Bio-Electronic, Photonic and MEMS Packaging*; Wong, C. P.; Moon, K. S.; Li, Y., Eds.; Springer Science: New York, 2010; pp. 277–314.

(12) Shenogina, N.; Shenogin, S.; Xue, L.; Keblinski, P. On the Lack of Thermal Percolation in Carbon Nanotube Composites. *Appl. Phys. Lett.* **2005**, *87*, 133106.

(13) Yu, A.; Itkis, M. E.; Bekyarova, E.; Haddon, R. C. Effect of Single-Walled Carbon Nanotube Purity on the Thermal Conductivity of Carbon Nanotube-Based Composites. *Appl. Phys. Lett.* **2006**, *89*, 133102.

(14) Bonnet, P.; Sireude, D.; Garnier, B.; Chauvet, O. Thermal Properties and Percolation in Carbon Nanotube-Polymer Composites. *Appl. Phys. Lett.* **2007**, *91*, 201910.

(15) Choi, S. U. S.; Zhang, Z. G.; Yu, W.; Lockwood, F. E.; Grulke, E. A. Anomalous Thermal Conductivity Enhancement in Nanotube Suspensions. *Appl. Phys. Lett.* **2001**, *79*, 2252.

(16) MOISALA, A.; LI, Q.; KINLOCH, I.; WINDLE, A. Thermal and Electrical Conductivity of Single- and Multi-Walled Carbon Nanotube-Epoxy Composites. *Compos. Sci. Technol.* **2006**, *66*, 1285–1288.

(17) Ostojic, G. N.; Hersam, M. C. Biomolecule-Directed Assembly of Self-Supported, Nanoporous, Conductive, and Luminescent Single-Walled Carbon Nanotube Scaffolds. *Small* **2012**, *8*, 1840–1845.

(18) Ma, P.-C.; Siddiqui, N. A.; Marom, G.; Kim, J.-K. Dispersion and Functionalization of Carbon Nanotubes for Polymer-Based Nanocomposites: A Review. *Compos. Part A Appl. Sci. Manuf.* **2010**, *41*, 1345–1367.

(19) Kwon, J.-Y.; Kim, H.-D. Preparation and Properties of Acid-Treated Multiwalled Carbon Nanotube/waterborne Polyurethane Nanocomposites. *J. Appl. Polym. Sci.* **2005**, *96*, 595–604.

(20) Göbel, A.; Hemberger, F.; Vidi, S.; Ebert, H. P. A New Method for the Determination of the Specific Heat Capacity Using Laser-Flash Calorimetry Down to 77K. *Int. J. Thermophys.* **2012**, *34*, 883–893.

(21) Ghosh, S.; Teweldebrhan, D.; Morales, J. R.; Garay, J. E.; Balandin, A. A. Thermal Properties of the Optically Transparent Pore-Free Nanostructured Yttria-Stabilized Zirconia. *J. Appl. Phys.* **2009**, *106*, 113507.

(22) Yan, Z.; Liu, G.; Khan, J. M.; Balandin, A. a. Graphene Quilts for Thermal Management of High-Power GaN Transistors. *Nat. Commun.* **2012**, *3*, 827.

(23) Kim, P.; Shi, L.; Majumdar, a.; McEuen, P. Thermal Transport Measurements of Individual Multiwalled Nanotubes. *Phys. Rev. Lett.* **2001**, *87*, 215502.

(24) Nika, D. L.; Balandin, A. A. Two-Dimensional Phonon Transport in Graphene. *J. Phys. Condens. matter an Inst. Phys. J.* **2012**, *24*, 233203.

(25) Balandin, A. A.; Nika, D. L. Phonons in Low-Dimensions: Engineering Phonons in Nanostructures and Graphene. *Materials Today*. 2012, p. http://www.materialstoday.com.

(26) Yang, K.; Gu, M.; Guo, Y.; Pan, X.; Mu, G. Effects of Carbon Nanotube Functionalization on the Mechanical and Thermal Properties of Epoxy Composites. *Carbon N. Y.* **2009**, *47*, 1723–1737.

(27) Chiolerio, A.; Castellino, M.; Jagdale, P.; Bianco, S.; Tagliaferro, A.; Torino, P. Electrical Properties of CNT-Based Polymeric Matrix NanoComposites. **2004**, 1–16.

(28) Castellino, M.; Chiolerio, A.; Shahzad, M. I.; Jagdale, P.; Tagliaferro, A. Electrical Conductivity Phenomena in an Epoxy Resin-Carbon-Based Materials Composite. *submitted*.

(29) Voo, R.; Mariatti, M.; Sim, L. C. Thermal Properties and Moisture Absorption of Nanofillers-Filled Epoxy Composite Thin Film for Electronic Application. *Polym. Adv. Technol.* **2012**, *23*, 1620–1627.

(30) Gojny, F. H.; Wichmann, M. H. G.; Fiedler, B.; Kinloch, I. a.; Bauhofer, W.; Windle, A. H.; Schulte, K. Evaluation and Identification of Electrical and Thermal Conduction Mechanisms in Carbon Nanotube/epoxy Composites. *Polymer (Guildf).* **2006**, *47*, 2036–2045.

(31) Lee, J.; Varshney, V.; Roy, A. K.; Farmer, B. L. Single Mode Phonon Energy Transmission in Functionalized Carbon Nanotubes. *J. Chem. Phys.* **2011**, *135*, 104109.

(32) Bryning, M. B.; Milkie, D. E.; Islam, M. F.; Kikkawa, J. M.; Yodh, A. G. Thermal Conductivity and Interfacial Resistance in Single-Wall Carbon Nanotube Epoxy Composites. *Appl. Phys. Lett.* **2005**, *87*, 161909.

(33) Bryning, M. B.; Islam, M. F.; Kikkawa, J. M.; Yodh, A. G. Very Low Conductivity Threshold in Bulk Isotropic Single-Walled Carbon Nanotube-Epoxy Composites. *Adv. Mater.* **2005**, *17*, 1186–1191.

(34) Kilbride, B. E.; Coleman, J. N.; Fraysse, J.; Fournet, P.; Cadek, M.; Drury, A.; Hutzler, S.; Roth, S.; Blau, W. J. Experimental Observation of Scaling Laws for Alternating Current and Direct Current Conductivity in Polymer-Carbon Nanotube Composite Thin Films. *J. Appl. Phys.* **2002**, *92*, 4024.

(35) Lee, G.; Lee, J. I.; Lee, M. P.; Kim, J. Comparisons of Thermal Properties between Inorganic Filler and Acid-Treated Multiwall Nanotube/Polymer Composites. *J. Mat. Sci.* **2005**, *40*, 1259–1263.

Chapter 3. Study of Graphene CVD Process to Synthesize Misoriented Bilayer Graphene

3.0 Abstract

Single-layer graphene is readily produced on copper (Cu) foil by conventional thermal chemical vapor deposition (CVD) method. However, a process for achieving bilayer graphene over large area with a similar fast and reproducible process has proved elusive despite extensive investigation by several groups. In this chapter the cooling phase is investigated to achieve uniform and continuous growth of both single and bilayer graphene on Cu foils with the growth phase sharply reduced in duration (5-60 times faster than previous methods). Large area growth of bilayer graphene is demonstrated on 30 cm x 30 cm Cu foils. Vacuum cooling is shown to be selective for single-layer graphene growth, while cooling in hydrogen gas was selective to bilayer graphene growth. Extensive characterization of the single and bilayer graphene was conducted including Raman spectroscopy, SAED, as well as electrical characterization by the fabrication of graphene field effect transistors.

3.1 Introduction

Graphene is a single atomic layer of carbon in a 2D hexagonal crystal lattice. Discovered by Novoselov and Geim,[1] graphene has been shown to have remarkable electrical,[2] mechanical,[3] optical,[4] and thermal properties.[5] Graphene has intrinsically better electron mobility than other transparent conducting materials, but facile synthesis of graphene over large area has been a challenge. For application as a channel material for nanoelectronics, again graphene possesses a high carrier mobility compared to

conventional semiconductors, but without layer number control on the wafer scale, the band gap of the film will vary from device to device. Bilayer graphene has a tunable bandgap with perpendicular applied field (see Figure 3.1), where single layer graphene has no bandgap.

Chemical vapor deposition (CVD) has been developed as a method for large area synthesis of graphene on metallic substrates such as Cu or nickel. The graphene may be transferred to dielectric substrates by coating the graphene with a polymeric handle and chemically etching the metallic substrate away. After the graphene and handle are transferred to the dielectric, solvents are used to dissolve the polymer, and the graphene--typically with polymer residue--remains. To increase the crystallite size and remove surface imperfections, the metallic substrate may be annealed at high temperature. Hydrogen may be flowed during the anneal to remove native oxide layers. After the annealing is complete, the substrates are ramped to the deposition temperature, and a carbon precursor gas (typically methane) is flowed. There is a window of pressure and carbon concentration where graphene flakes will nucleate and grow to cover the entire surface that depends on the CVD system and configuration.

The layer number of graphene depends on the ability of carbon to diffuse into the substrate, as well as the mechanics of deposition of the carbon from the gas phase to the substrate surface. For Cu, the carbon solubility is low (0.001 atomic %),[7] so very little carbon may diffuse into the substrate, and as the Cu cools very little carbon precipitates from the substrate to the surface. Typically on Cu the graphene grains will nucleate from

a defect, and the lateral growth is more energetically favorable than adlayer growth. Once the active Cu surface is entirely covered with the first graphene layer, the methane no longer decomposes and the result is single layer graphene with relatively small bi- or few-layer graphene patches at the nucleation points. For nickel, carbon solubility is higher (>0.1 atomic % solubility),[7] and carbon may diffuse into the substrate, and instead of single-layer graphene, few-layer graphene forms during the cooling phase, but the layer number varies from one area to another (see Fig. 3.2).

Different processes and methods have been developed to achieve graphene synthesis with layer number control, but they are slow[8–10] and or limited to small growth areas.[10,11] They rely on changing the post-growth cooling rate, or using an impure Cu or Cu-Ni alloy to tune the carbon solubility. Other studies have investigated the effect of increasing the hydrogen partial pressure during the growth phase.[12–14] Vlassiouk et al. demonstrated hydrogen during the growth phase may hinder adlayer growth via etching, encouraging single layer graphene growth.[12] Recent studies suggest that the cooling environment for atmospheric-pressure CVD on platinum effects the graphene layer number.[15]

3.2 Experimental Methods

Copper foil (Alfa Aesar 25 μm, 99.8%) was cut into rectangular pieces about the same area as the 3 cm x 5 cm quartz block used as a sample chuck in the CVD tube. Four larger area foils (3 cm x 15 cm and 30 cm x 30 cm) were placed on two quartz blocks or placed directly on the furnace tube, or rolled around a quartz wafer carrier. The growth process (see Fig. 3.3) for both cooling experiments includes annealing in hydrogen, followed directly by growth at high temperature, and then cooling to ambient temperature. This process is based on the

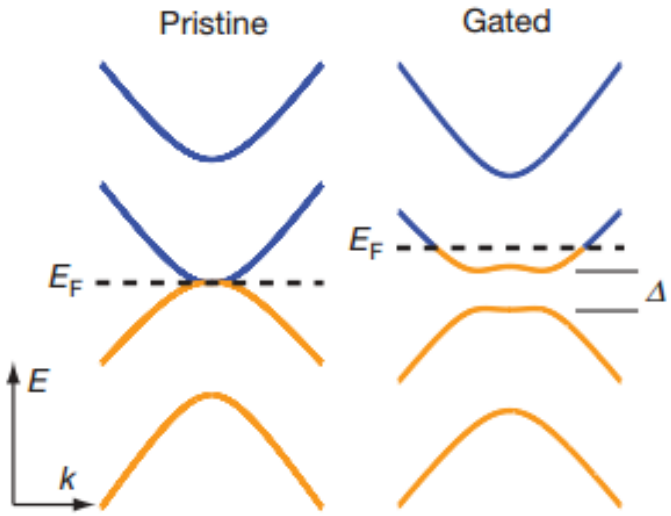


Figure 3.1. Bilayer graphene electron energy band diagrams unperturbed (pristine) and gated (perpendicular applied field). Δ is the electron band gap energy. © 2009 Macmillan Publishers Ltd. Reprinted, with permission, from [Zhang, Y.; Tang, T-T.; Girit, C.; Hao, Z.; Martin, M. C.; Zettl, A.; Crommie, M. F.; Shen, Y. R.; Wang, F. Direct Observation of a Widely Tunable Bandgap in Bilayer Graphene. *Nature* 2009.][6]

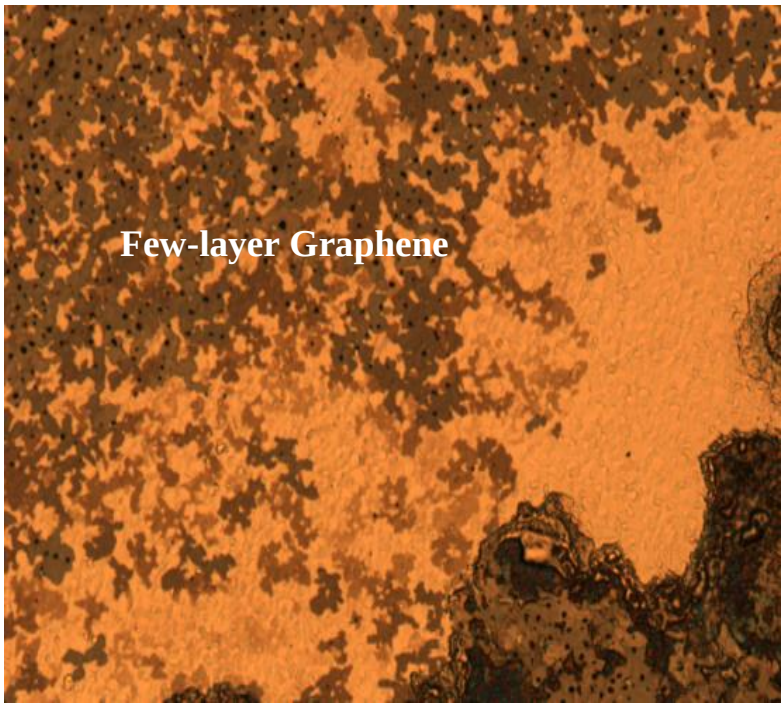


Figure 3.2. Optical image of few-layer graphene chemical vapor deposited on nickel.

methods developed by Li et al.[16] The Cu foil is annealed in 1000 sccm hydrogen at 800 °C for 30 min. and 300 Torr chamber pressure prior to the growth. The temperature is increased to 1000 °C, the chamber is purged to 0.1 Torr pressure, and methane is flowed

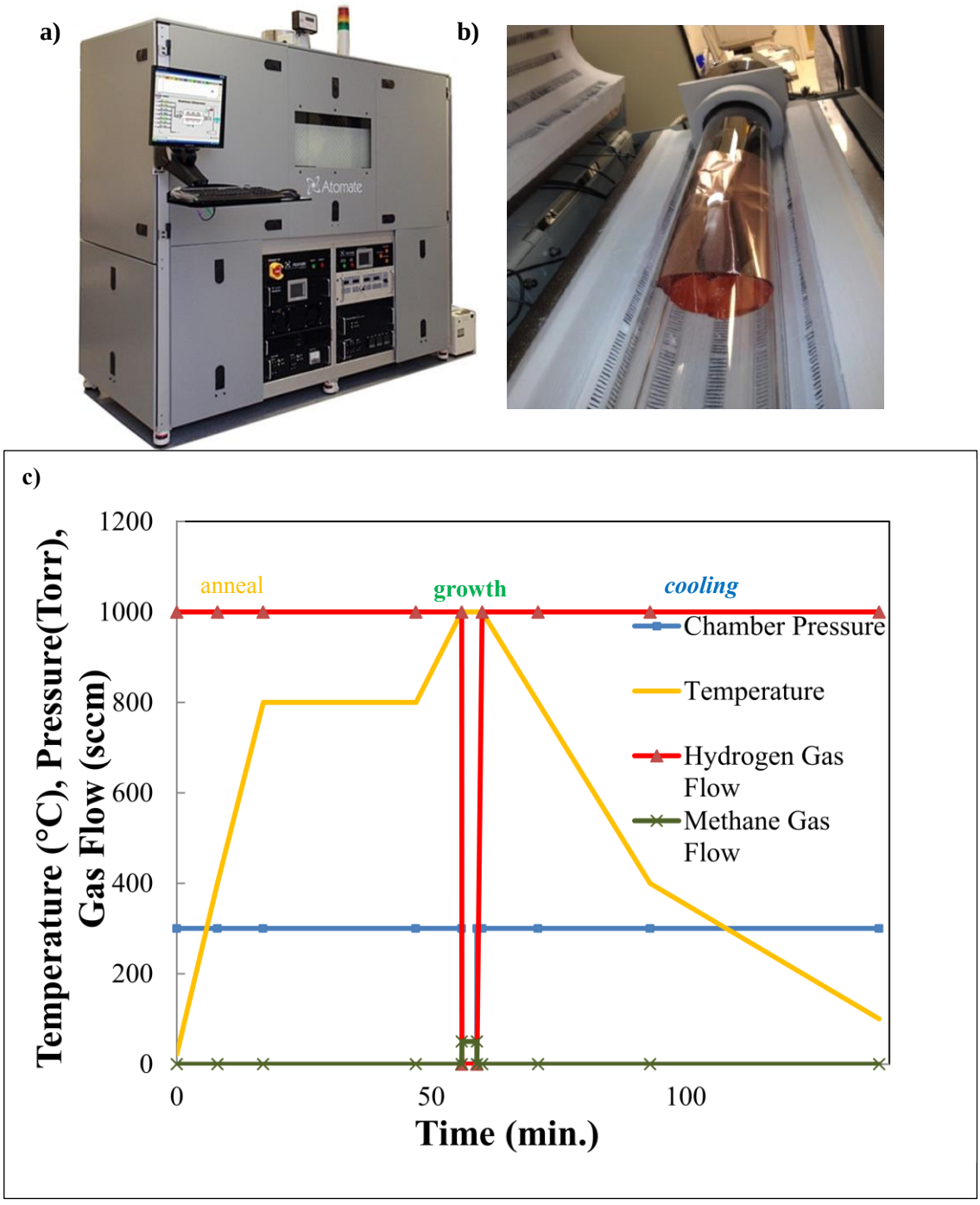


Figure 3.3. Photos of (a) CVD system and (b) 30 cm x 30 cm foils in CVD furnace tube. Process parameters for (c) hydrogen cooling experiment.

at 50 sccm and 1 Torr chamber pressure for 3 min. The chamber is purged to 0.01 Torr pressure, then set to 300 Torr. The temperature is set to ambient, and hydrogen and argon are flowed at 1000 sccm. When chamber pressure reaches 300 Torr (~3 minutes, ~920 °C), the argon flow is ceased. Once the temperature reaches ≤100 °C, the chamber is purged to 0.01 Torr, and the samples are removed from the chamber using nitrogen as a purging gas. For vacuum-cooling experiment, the chamber remains purged at 0.01 Torr for the entire cooling process to ambient temperature.

A micro-Raman spectrometer was used with 442 nm excitation at ~30 mW for graphene on the Cu foil samples, and 514 nm excitation at ~ 7.7 mW for the graphene on SiO_2 device samples. The laser power was optimized for signal-to-noise ratio. These laser powers did not damage the graphene on Cu or SiO_2. SEM images were taken using a focused ion beam/SEM in SEM mode at 5 kV and ~5 mm working distance. Light transmittance tests were carried out using a UV/VIS spectrophotometer.

Graphene was transferred from Cu by spinning A4 PMMA (950k molecular weight) at 3 krpm onto the Cu foil, followed by baking (5 min at 180 ºC) on a hotplate. The foil was then backside etched in 10% HNO_3 acid solution for 10 min, and optical microscopy was used to confirm the etching. Ferric chloride acid was used to etch the Cu away for ~10 minutes, and a clean piece of SiO_2/Si was submerged into the acid bath to retrieve the PMMA-graphene films and place them into water for a minute. The rinse was repeated with two fresh baths of water, a minute each. Then, the test SiO_2/Si substrates were submerged into the water bath to retrieve the PMMA-graphene film. The substrates were

baked at 115 ºC to remove the water for 1 min, and the substrates were placed onto a hotplate at 180 ºC for one minute to flatten out the film. The substrates were cleaned in an acetone:dichloroethane solution for 12 hours and dried with an N_2 gun, followed by an additional minute on a hotplate at 70 ºC to drive off the solvents that remained. The same transfer process was used for the quartz slides used in the light transmission tests, as well as for the TEM grid samples.

Graphene from each of the CVD cooling experiments was transferred onto 100 nm thick SiO_2 with the highly doped Si substrate as the back gate using the standard graphene transfer process.[17] Electron beam lithography (e-beam) was used to pattern the source/drain contact electrodes, and electron beam evaporation was used to deposit the desired metal contact (Ni). The channel lengths and widths for the GFETs were subsequently defined by electron beam lithography followed by oxygen plasma etching.

3.3 Results of the Experiments

Graphene films were synthesized on Cu foils by thermal CVD process (at 1000 °C) using intermediate methane flow (50 sccm) as a carbon source at intermediate pressure (1 Torr). Single-layer graphene was grown by cooling from the growth temperature in vacuum (0.01 Torr), and bilayer graphene by cooling from the growth temperature in hydrogen at high pressure (300 Torr). These graphene films were transferred to Si substrates with 300-nm-thick SiO_2 for optical microscopy and Raman characterization and to transmission electron microscopy (TEM) grids for selected area electron diffraction (SAED) measurement. Figure 3.4a and b show stitched optical images of the vacuum- and hydrogen-cooled graphene on SiO_2, respectively. The transferred graphene

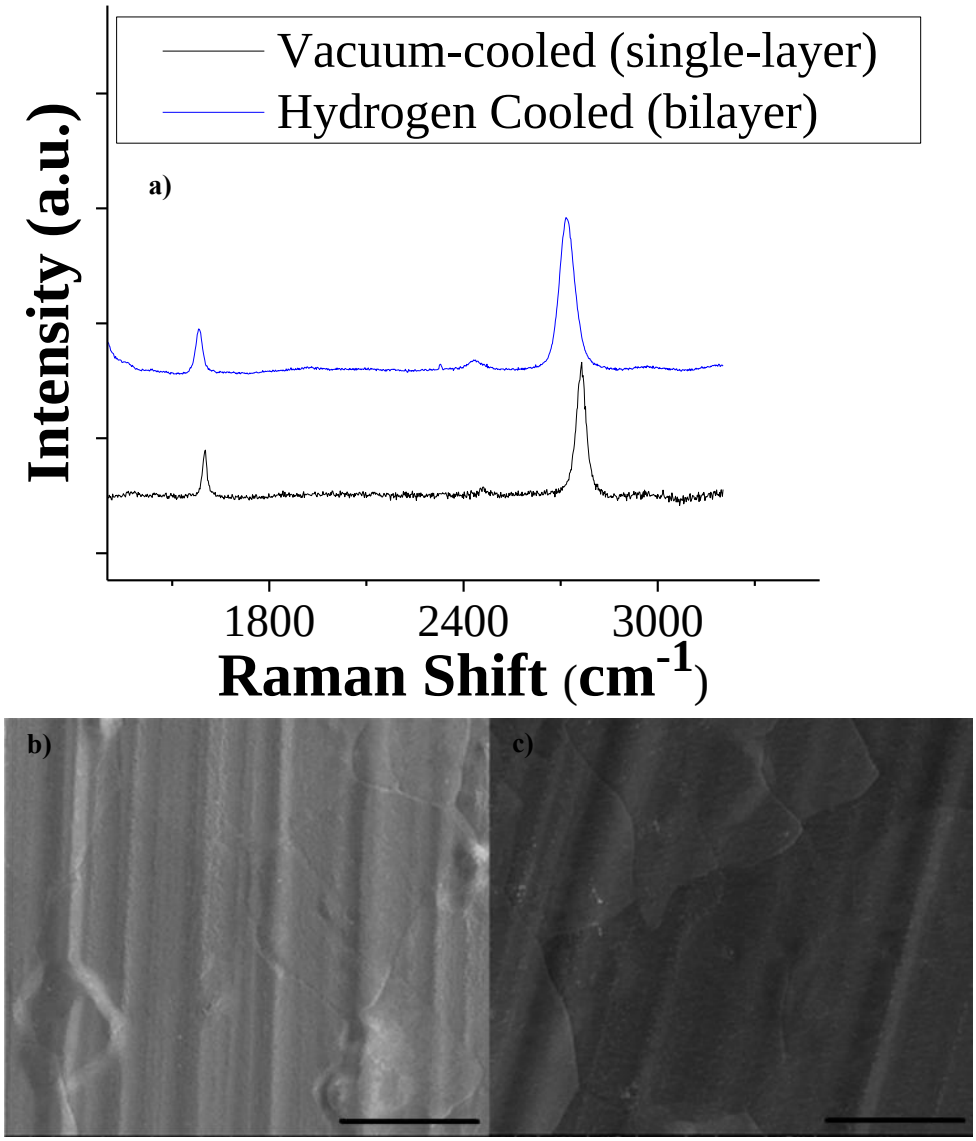


Figure 3.4. (a) Raman spectra of vacuum-cooled (single-layer) and hydrogen-cooled (bilayer) graphene on Cu by 442 nm excitation. SEM images of (b) hydrogen-cooled bilayer and (c) vacuum-cooled single layer, grown on 3 cm x 5 cm Cu foil (scale bars, 30 μm).

films appear to be continuous on the centimeter scale (limited only by the size of the Cu foil), with occasional tears and residue from the transfer process. Common graphene characterization practice is to transfer the graphene onto a SiO_2 substrate by using ferric

chloride or ammonium persulfate etching of Cu[18] and then to characterize the graphene by Raman spectroscopy at 514 nm laser excitation. This transfer process can introduce variable amounts of contamination or degradation of the as-grown CVD graphene and adds uncertainty to Raman and other material property characterization. To avoid this ambiguity, Raman characterization was performed before and after the graphene was transferred (see Figs.3.4a and 3.5a).The differing 2D/G intensity ratios for the vacuum and hydrogen-cooled samples in the Raman spectra (Fig. 3.5a) at 514 nm emission indicate growth of single- and bilayer graphene, respectively. Close inspection of the symmetric nature of the 2D peak reveals that the blue curve in Fig. 3.5a is misoriented, rather than AB-stacked, bilayer graphene. The Raman mapping results carried out in this study indicate that the hydrogen-cooled graphene possesses a range of 2D/G ratios over the sample area (see Figs. 3.6 and 3.7), suggesting a range of stacking angles and degrees of coupling between layers in the bilayer film. Further experiments, including SAED (Fig. 3.5 e, f) were conducted to confirm the graphene layer number for each cooling condition.

The bilayer graphene SAED (Fig. 3.5f) shows 27º misorientation between layers.

Scanning electron microscopy (see Fig. 3.4b and c) indicates that the films on Cu foil are continuous over the entire sample area, and Raman mapping was employed to further investigate the graphene layer number, uniformity and continuity. In both cases, the graphene forms grains that are less than 5 microns in size. The graphene coverage is greater than 90% after 3 minutes of growth. The graphene grows along the terraced Cu foil surface.

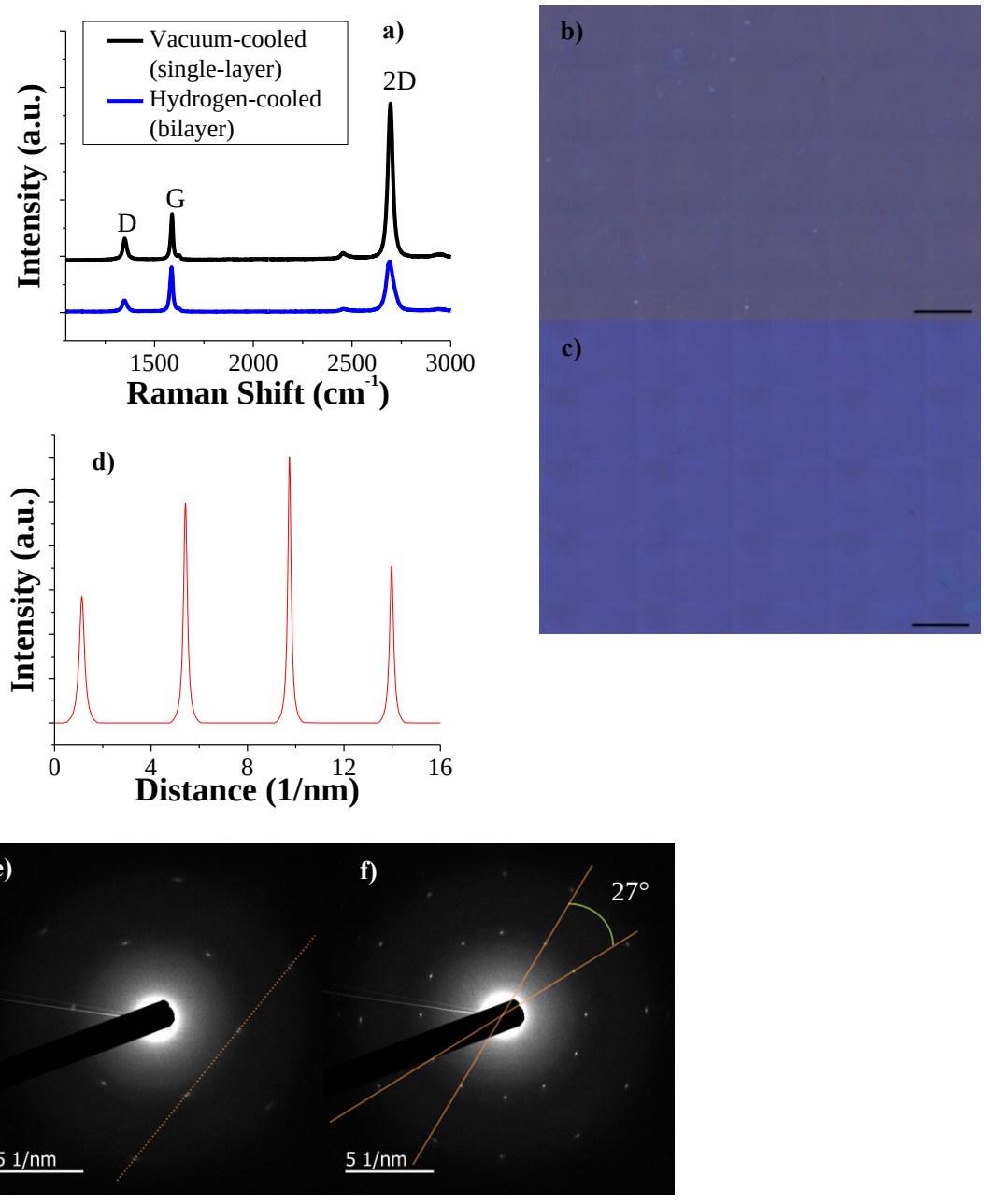


Figure 3.5. Raman spectra (a) of single-layer and bilayer graphene on SiO_2 (514 nm excitation). Stitched optical image maps of (b) hydrogen-cooled (bilayer) graphene and (c) vacuum-cooled (single-layer) graphene on SiO_2 substrate. Scale bar is 200 µm. SAED of single-layer (e) and bilayer (f) graphene. Line profile plot (d) of single-layer graphene SAED along dashed line in (e)

The Raman spectra in Fig. 3.5a (514 nm emission with SiO_2) and Fig. 3.4a (442 emission with Cu foil) differ in important ways. In Fig. 3.4a, with 442 nm excitation on Cu foil, there is no apparent defect peak (the D peak centered about 1350 cm^{-1}) for the Raman spectra of graphene for either cooling condition. Whereas in Fig. 3.5a the D peak is apparent in both the hydrogen and vacuum-cooled graphene Raman spectra. The intensity ratio for the 2D peak (centered about 2700 cm^{-1}) to the G peak (centered about 1580 cm^{-1}) is generally equal to or greater than 2:1 for both cooling conditions on Cu foil. While the single-layer graphene film has the typical 2D-to-G peak intensity ratio of 2:1, that of the bilayer graphene varies from 2:1 to 5:1. The average full width at half maximum (FWHM) of the 2D peak of the bilayer graphene film is slightly greater than that of the single-layer graphene (Raman spectra in Fig. 3.4a and histogram in 3.6b). Also, in Fig. 3.4a it is clear that the 2D and G peaks shift to lower wavenumber from single- to bilayer graphene. The direction of shift is opposite to that after transfer with 514 nm excitation on SiO_2 (compare Figs. 3.4a and 3.5a).[19,20]

To further distinguish the bilayer from the single-layer graphene film, the films were deposited on a SiO_2 substrate by using the polymethylmethacrylate (PMMA) liquid transfer method. This is particularly necessary for better comparison with the literature values of the FWHM for the Raman 2D peak and the 2D/G peak intensity ratios, which are typically taken from a graphene film on SiO_2 at 514 nm excitation.[19,20] It was observed that the Raman spectra of graphene on Cu foil does not correspond directly with that of graphene on the SiO_2 substrate, particularly in the case of bilayer graphene.

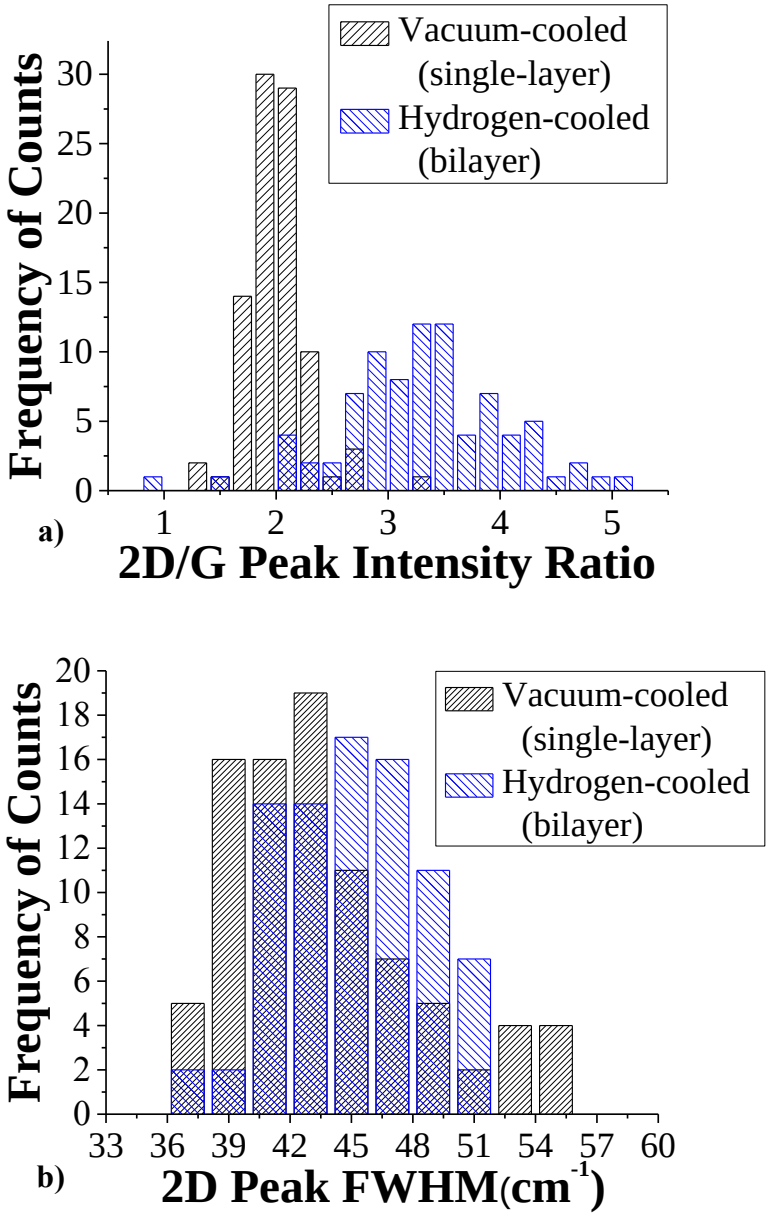


Figure 3.6. Histograms for 2D/G peak intensity ratio (a) and 2D peak FWHM (b) Raman spectroscopy maps of vacuum-cooled (single-layer) and hydrogen-cooled (bilayer) graphene on Cu with 442 nm excitation

Figures 3.7 and 3.8 show the spatial Raman mapping of the hydrogen-cooled and vacuum-cooled graphene on Cu (30 μm x 30 μm) and on SiO_2 (1 mm x 1 mm). The maps indicate that the trends observed in the Raman spectra in Figs. 3.4 and 3.5 hold true for

large area. Figure 3.9 shows the statistical results for the Raman data obtained for graphene on SiO_2 at 514 nm excitation (see Fig. 3.8 for corresponding Raman area maps). For single-layer graphene on SiO_2, the 2D peak FWHM was ~31 cm^{-1}, with a 2D/G intensity ratio of ~2.4 and an average 2D peak Raman shift of ~2689 cm^{-1}. For the bilayer graphene on SiO_2, the 2D peak FWHM varied from 32 to 45 cm^{-1}, the 2D/G peak intensity ratio was centered about ~2.4, and the average 2D peak Raman shift was ~2692 cm^{-1}. The Raman mapping combined with the statistical results in Fig. 3.9 show conclusively that the films transferred from the Cu foil are composed mostly of single-layer (for vacuum-cooled) or bilayer (for hydrogen-cooled) graphene.

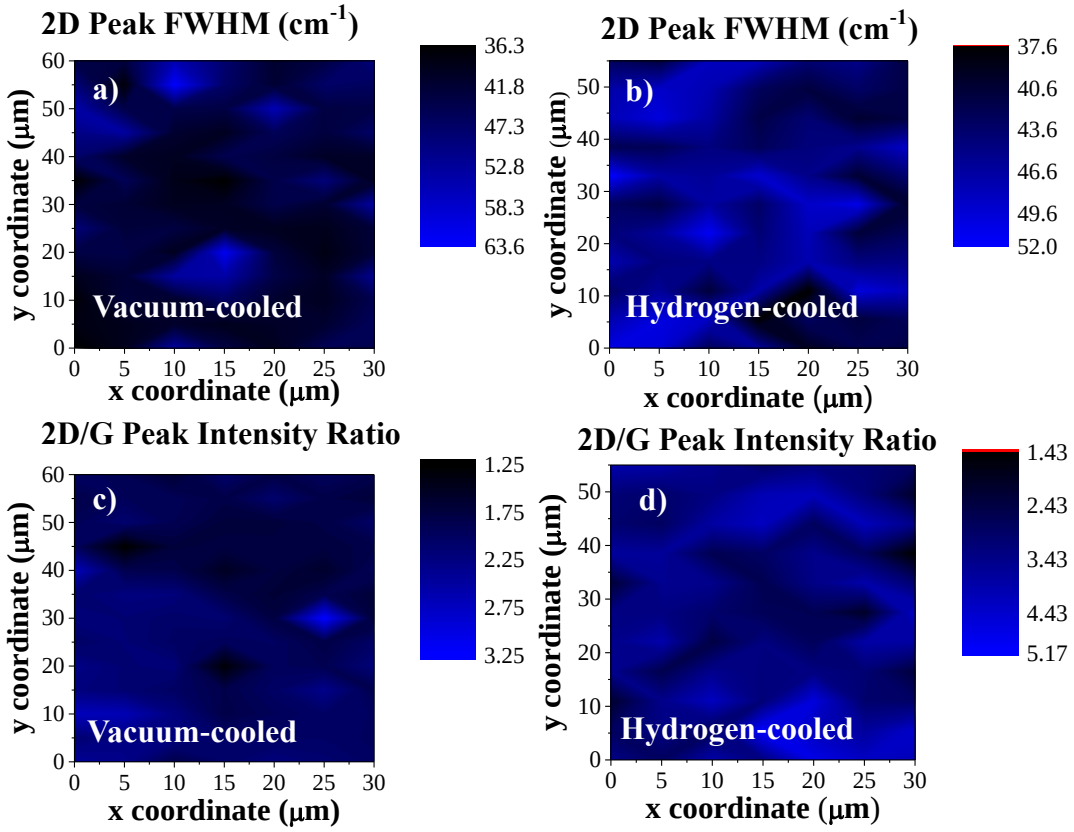


Figure 3.7. 2D peak FWHM Raman spectroscopy map of (a) vacuum-cooled single-layer and (b) hydrogen-cooled bilayer graphene on Cu; 2D/G peak intensity ratio Raman spectroscopy map of (c) vacuum-cooled single-layer and (d) hydrogen-cooled bilayer graphene (all maps 5-μm steps, 442 nm excitation).

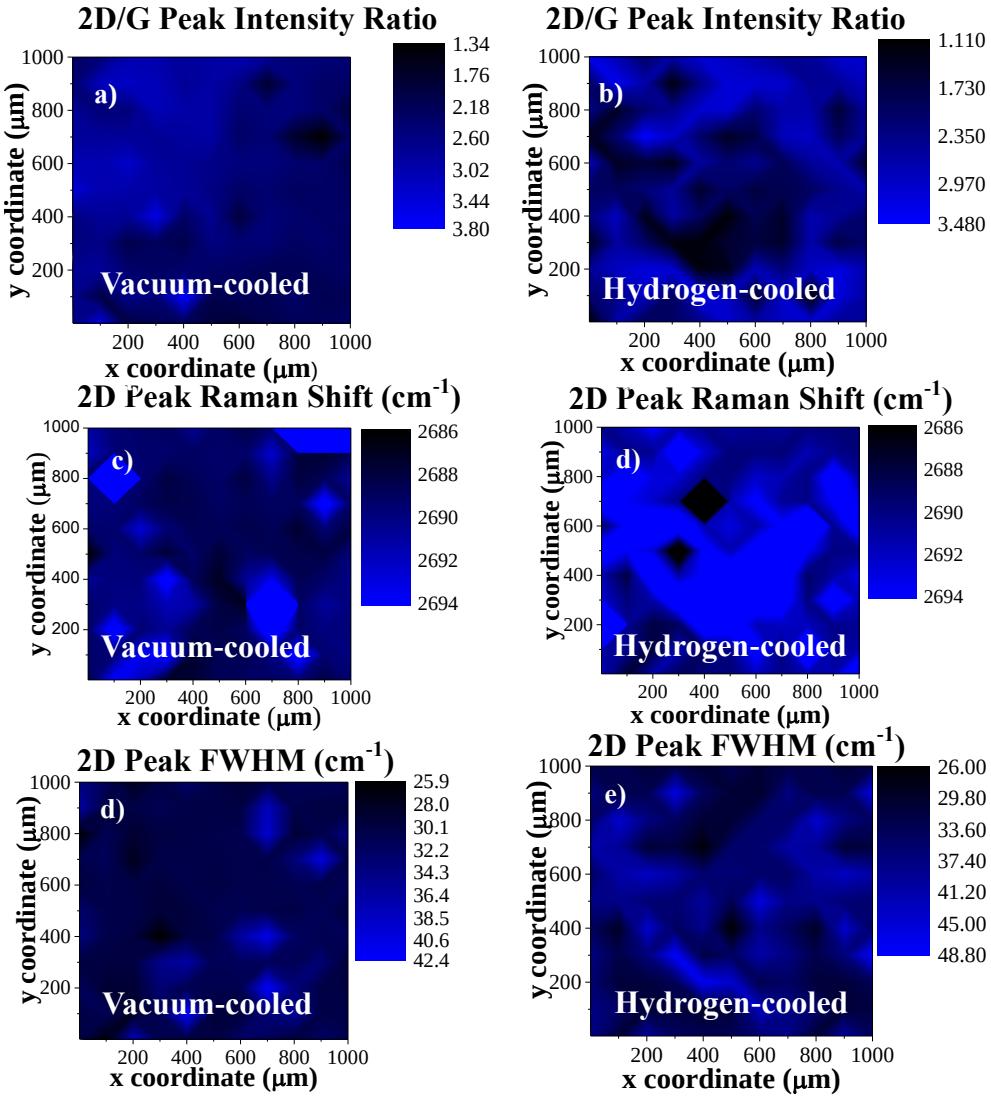


Figure 3.8. Raman spectroscopy of hydrogen-cooled bilayer and vacuum-cooled single-layer graphene transferred to SiO_2, 514 nm excitation (100 μm steps). 2D/G peak intensity ratio, 2D peak Raman shift, 2D peak FWHM Raman spectroscopy maps of hydrogen-cooled bilayer (b, d, and f, respectively) and vacuum-cooled single-layer (a, c, and e, respectively) graphene on SiO_2.

To further demonstrate that the films are predominantly single- or bilayer graphene, the electrical transport properties were evaluated by fabricating back-gated graphene field effect transistors (GFETs).

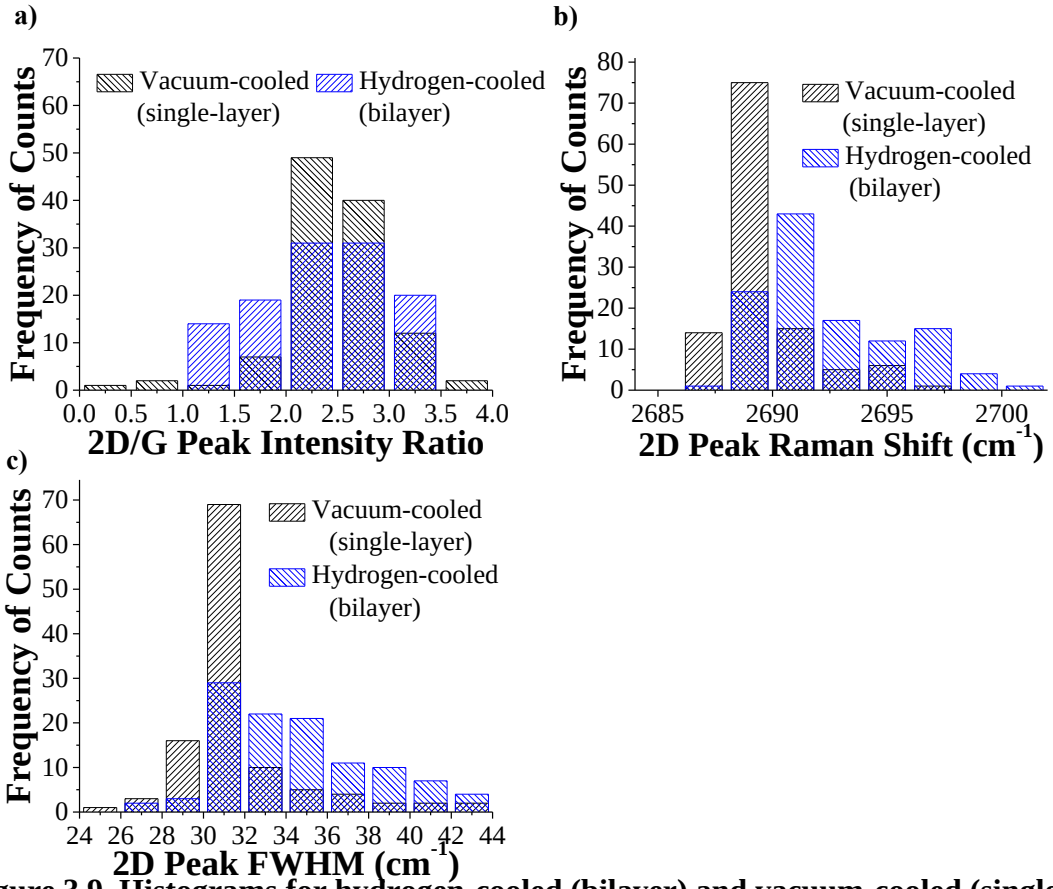


Figure 3.9. Histograms for hydrogen-cooled (bilayer) and vacuum-cooled (single-layer) graphene transferred to SiO2: (a) 2D/G peak intensity ratio, (b) 2D peak Raman shift, and (c) 2D peak FWHM. Data taken from Raman spectroscopy over 1 mm x 1 mm area using 514 nm excitation.

It is understood that single-layer graphene possesses a higher intrinsic mobility than bilayer graphene.[21] Recent studies, however, suggest that misoriented bilayer graphene may maintain the linear dispersion of single layer graphene[22] and thus have similar electron mobility as single-layer graphene, but this depends on the amount of coupling between the graphene layers, which is based on the stacking angle.[22] The ON-OFF ratio

of mechanically exfoliated GFETs was shown to decrease with increasing number of AB-stacked well coupled layers.[23] Based on Raman spectroscopy data, the hydrogen-cooled graphene is mostly misoriented bilayer with some areas of inter-layer coupling. Whereas and the vacuum-cooled graphene is essentially all monolayer, and therefore it is expected that the GFETs made from the vacuum-cooled graphene would have higher carrier mobilities and On-OFF ratios than the GFETs made with the hydrogen-cooled graphene. Figure 3.10a shows an SEM image of a prototype GFET device, and Fig. 3.10b shows the device structure schematically.

The linear trends in the output characteristics indicate ohmic contact formation at the Ni/graphene interface for both GFET types. Figure 3.10d shows the transfer characteristics for the same devices. The table in Fig. 3.10 shows extracted average carrier mobilities and current ON-OFF ratios from 20 fabricated GFETs. As shown by the table in Fig. 3.10, the current ON-OFF ratio is ~5 for GFETs made from vacuum-cooled graphene and ~2 for GFETs made from the hydrogen-cooled graphene. Both GFETs exhibit symmetric transfer characteristics, indicating that the field effect mobility for the electrons and the holes is similar. The field effect mobilities were calculated by using the conventional equation: $g_m=\mu C_{OX}(W/L)V_{DS}$ at low V_{DS} = 0.1 V, where g_m is the transconductance; μ is the field effect mobility; W and L are the channel width and the channel length, respectively; and $C_{OX} = \varepsilon_{OX}/d_{OX}$, where ε_{OX} is the dielectric constant, and d_{OX} is the thickness of the gate oxide. Assuming d_{OX} = 100 nm for SiO_2, $\varepsilon_{OX} = 3 \times 10^{-11}$, which gives $C_{OX} \sim 3 \times 10^{-4}$ F/m^2. From these data, the average effective field-effect mobility values for electrons (μ_n in table) were found to be 1652±126 and 1211±98

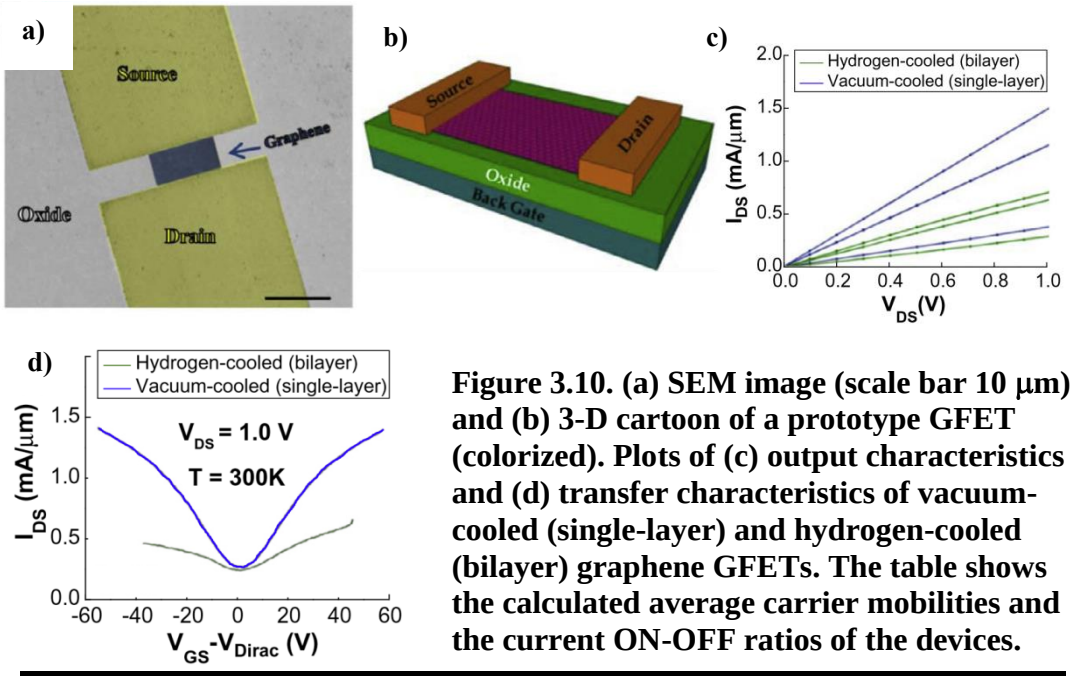


Figure 3.10. (a) SEM image (scale bar 10 μm) and (b) 3-D cartoon of a prototype GFET (colorized). Plots of (c) output characteristics and (d) transfer characteristics of vacuum-cooled (single-layer) and hydrogen-cooled (bilayer) graphene GFETs. The table shows the calculated average carrier mobilities and the current ON-OFF ratios of the devices.

CVD Graphene	Average μ_n (cm^2/V-s)	Average μ_p (cm^2/V-s)	Average I_{ON}/I_{OFF}
Vacuum cooled (single-layer)	1652±126	1743±109	~5
Hydrogen-cooled (bilayer)	1211±98	1301±45	~2

cm^2/V-s for the vacuum-cooled and hydrogen-cooled graphene, respectively. The corresponding hole mobility values (μ_p in table) are 1743±109 and 1301±45 cm^2/V-s. Our overall mobility values are slightly lower than the reported values in the literature due to the smaller graphene grain size (3-5 micron). In our devices, the GFETs made from vacuum-cooled graphene films had higher mobility than the GFETs made from

hydrogen-cooled graphene films, confirmed the presence of increased coupling in some areas of the hydrogen-cooled graphene films. The ON-OFF ratio should increase as the inter-layer coupling between layers decreases.[23] That indicates that the GFETs made from hydrogen-cooled films have electronic characteristics more similar to bilayer or few layer GFETS, whereas the GFETS made from the vacuum cooled graphene films have single-layer electronic characteristics. The Raman spectroscopy mapping was performed after the GFET channel devices were tested for electronic properties to confirm that the graphene films were not significantly altered by the device fabrication or testing process (see Fig.3.11). Suspended AB stacked bilayer graphene is 95.4% transparent to white light, whereas suspended single-layer graphene is 97.7% transparent.[24] Misoriented bilayer graphene has misorientation angle dependent optical conductivity, and will have a wavelength dependent transparency that falls somewhere between bilayer and single-layer graphene.[26,27] The hydrogen- and vacuum-cooled graphene samples were thus transferred onto quartz microscope slides for light transmission analysis. As shown in Figure 3.12, single-layer graphene has a similar light transmittance as bilayer graphene, and both films show higher transmittance than suspended single-layer or suspended AB-stacked bilayer graphene. This may be understood in the context of recent experiments with graphene optical modulators. [28,29] During light transmittance experiments, it is possible that the UV-vis radiation caused doping of the graphene films, resulting in a decrease in light absorption, even without bias.[29,30]

Because most of the bilayer graphene is misoriented, it behaves similar to single-layer graphene. Additionally UV-vis induced doping may have increased the film transparency

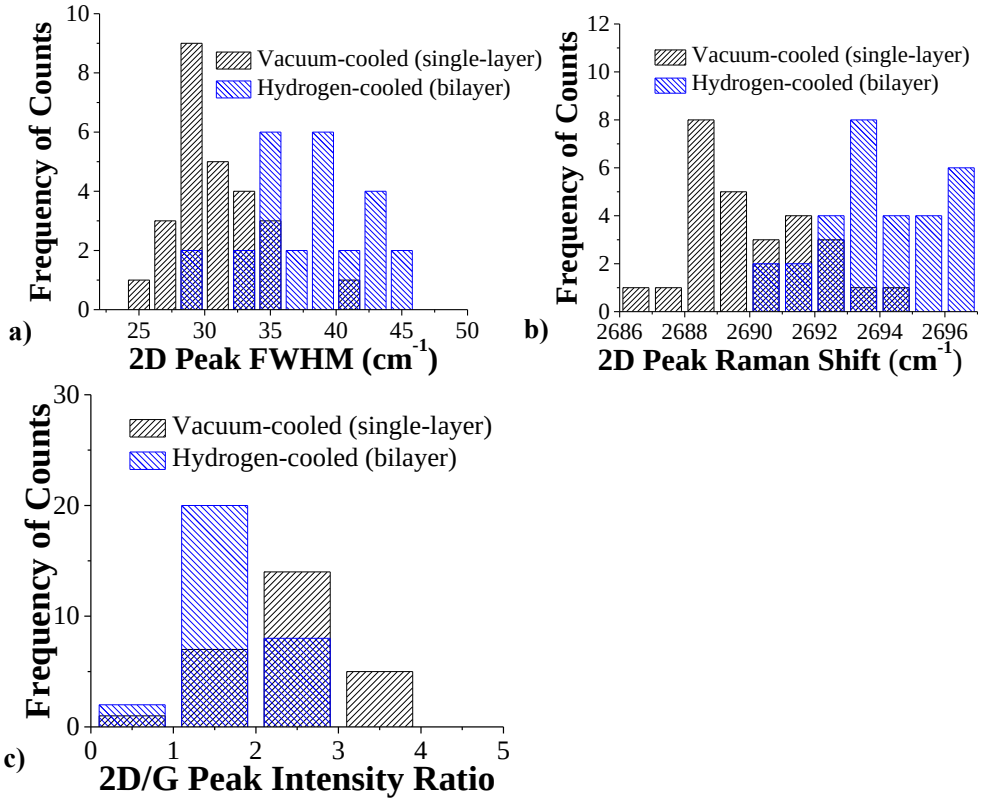


Figure 3.11. Graphene device channel Raman characteristics for single and bilayer graphene on SiO_2, 514 nm excitation: (a) 2D peak FWHM, (b) Raman shift of 2D peak, (c) 2D/G peak intensity ratio.

with the quartz slide underneath providing charge trapping sites. Raman spectroscopy analysis indicates that such doping may have occurred (see Table 3.2).The G-peak of the Raman spectrum of the graphene films on quartz before and after UV-vis exposure was analyzed. There is an indication of shift of the Raman peak (the G-peak). The shift in the G-peak position indicates that doping may have occurred.[25] The details of the shift in the G-peak and FWHM are given in Table 3.2. However, the devices fabricated using the synthesized graphene films exhibited moderate mobility $>10^3$ $cm^2/V\text{-}s$, indicating that doping, if at all present, had little negative effect on the electrical mobility of the films. This makes the films applicable as transparent conductors for variety of applications.

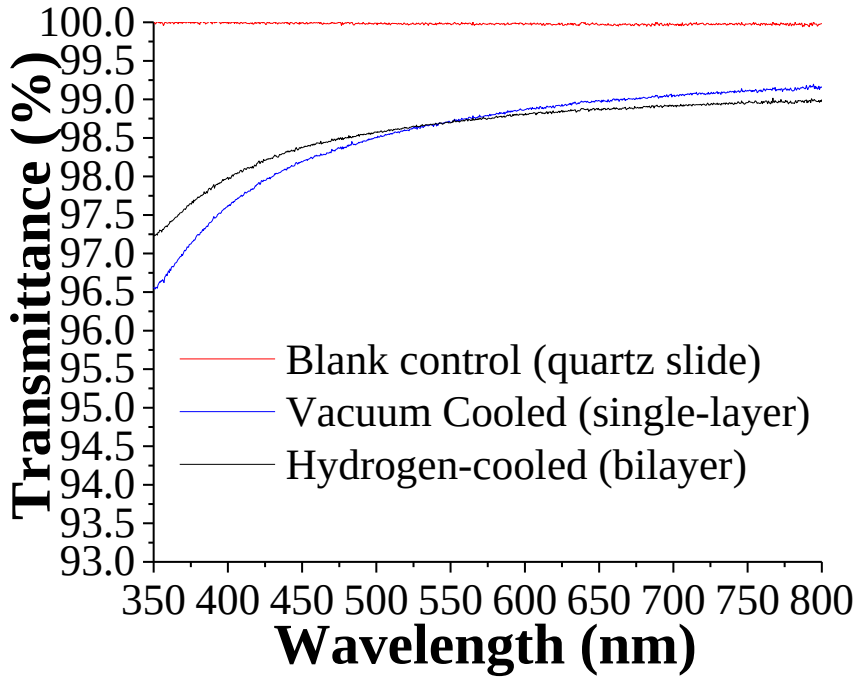


Figure 3.12. Visible light transmittance of vacuum-cooled (single-layer) and hydrogen-cooled (bilayer) graphene transferred to quartz microscope slides.

	After Transfer		
	G-Peak Raman Shift (cm^{-1})	G-Peak FWHM (cm^{-1})	Hole concentration (cm^{-2})
Single-Layer Graphene	1589	26.7	~$0.4x10^{13}$
Bi-Layer Graphene	1594	24.7	~$0.5x10^{13}$
	After UV-vis Testing		
Single-Layer Graphene	1596	21.5	~$1.6x10^{13}$
Bi-Layer Graphene	1591	20.4	~$0.7x10^{13}$

Table 3.2. Measured Raman shift and FWHM of the G-peak of single and bilayer graphene before and after UV-vis irradiation, with corresponding carrier concentrations, extracted from [25].

Because the hydrogen cooling process was so consistent in achieving bilayer graphene over 3 cm x 5 cm Cu foils, larger foil sizes (5 cm x 15 cm and 30 cm x 30 cm) were experimented with. These foils were subjected to Raman spectroscopy at 442 nm excitation. Figure 3.13 shows the Raman spectra and histograms for the 30 cm x 30 cm foil. The FWHM for the 2D peak in Fig. 3.13b is much larger than the cutoff at ~42 cm^{-1} for 442 nm excitation of single-layer graphene on Cu foil (compare Fig. 3.13b and 3.6b).

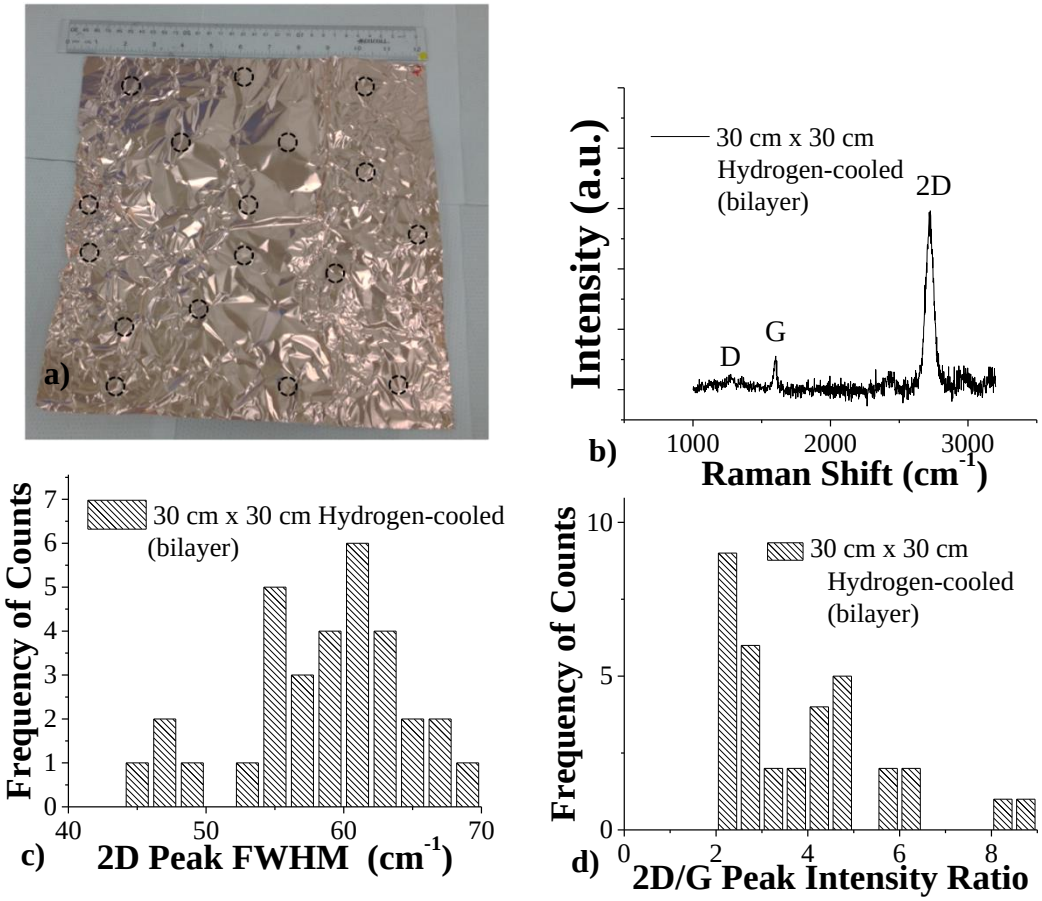


Figure 3.13. (a) Photo of 30 cm x 30 cm (~1 ft x 1 ft) Cu foil after hydrogen-cooled CVD process. (b) Typical Raman spectra from the large area samples with 442 nm excitation. Histograms of (c) 2D peak FWHM and (d) 2D peak ratio of Raman spectra (442 nm excitation) taken from 30 cm x 30 cm foils. Areas measured indicated as dashed circles in image (a).

Also, the 2D/G intensity ratios ranged from 2:1 to 8:1 for the 30 cm x 30 cm foils (Fig. 3.13d). The variation and range in 2D/G intensity ratios correspond well with those for 442 nm excitation of the 3 cm x 5 cm bilayer foils (compare Fig. 3.13d and 3.6a). Similar results were obtained with Raman spectroscopy of the 5 cm x 15 cm samples.

3.4 Discussion

At high temperature (~1000 °C) with CVD, the Cu foil catalyzes the decomposition of methane into elemental carbon and hydrogen gas and allows carbon adatoms to form islands around the defects on the foil surface. The islands then grow until they meet each other, forming misoriented grains typically a few microns in size, depending on the nucleation point density.[31] The diffusion of carbon into the Cu foil is strongly impeded due to the extremely low solubility of carbon in Cu. As a result, the grain growth is achieved mostly by deposition of carbon from the gas phase, rather than diffusion from the bulk. For that reason, it was expected that for CVD of graphene on Cu, the mixture of the flowing gases is critical. Most studies meticulously detail the gas flow during the high temperature growth, typically cooling in the same gas mixture to ambient temperature. The results of this study show the possible impact of flowing gases different from the growth mixture (in particular, hydrogen) during the cooling phase on the growth of graphene.

For the majority of the hydrogen-cooled sample area after transfer, the FWHM is above the cut-off for single-layer graphene (~30 cm^{-1}).[9,32] Misoriented bilayer graphene on SiO_2 has an FWHM of ~30-50 cm^{-1} with 514 nm excitation, as well as 2D/G ratios similar to those of single-layer graphene, from ~2:1 to 3:1.[9,10,19,20,33] The 2D peak location is known

to shift upward in frequency with an increase of graphene layer number from 1 to 2. For misoriented bilayer graphene on SiO_2, the shift is dependent on the misorientation angle.[20,33] The magnitude of the shift also depends on the excitation energy.[19,20] We observed an increase in average FWHM from single- to bilayer graphene on SiO_2 (Fig. 3.9), as well as in our GFET device channels (see Fig. 3.11). The 2D frequency distribution plot for the hydrogen-cooled sample with 514 nm excitation shows an upward shift from the single to bilayer (see Fig. 3.9). That corresponds well with previous experimentally obtained shifts for misoriented non-coupled bilayer graphene.[19,34] In the SAED for single-layer graphene, the line profile plot intensity should show the inner points are higher in intensity than the outer.[8,10] For SAED of misoriented bilayer graphene, the intensities will vary with angle of misorientation, and the misorientation angle of the points indicates the angle of orientation of the two layers.[8,10] For example, Fig. 3.5f shows the SAED for a portion of a suspended bilayer membrane with misorientation angle of ~27º. The SAED measurements of the vacuum-cooled samples show characteristics of single-layer graphene, whereas the hydrogen-cooled samples show characteristics of misoriented bilayer graphene. Further SAED showed AB-stacked graphene in some regions of the hydrogen-cooled graphene. For these reasons hydrogen-cooled graphene was concluded to be a bilayer, whereas vacuum-cooled graphene is a single layer.

Cooling experiments for larger foils (up to 30 cm x 30 cm) were also carried out (see Fig. 3.13). The FWHMs for the 2D peak from the Raman measurements of the large foils cooled with hydrogen flow are above the cutoff at 30 cm^{-1} for single-layer graphene, corresponding better with misoriented bilayer graphene. The 2D/G peak intensity ratio

from Raman spectroscopy measurements of the large foils (Fig. 3.13) matches the observed distribution of ratios for the hydrogen-cooled bilayer graphene on 3 cm x 5 cm foils (Fig. 3.6a). Based on these results, the sample size for this continuous and uniform bilayer growth process was concluded to be limited only by the size of the CVD chamber, where gas flow, pressure, and temperature can be well controlled.

The mechanism of the graphene growth can be understood from the experimental results and previous experimental and theoretical studies. In typical CVD graphene processes on Cu, methane is decomposed at the Cu surface during the growth phase (~1000 °C). Crystalline graphene islands form about nucleation points; in some cases, secondary and tertiary graphene layers form at the nucleation points.[35,36] When the graphene layers eventually meet, no Cu surface is available to catalyze the decomposition of methane, little bulk carbon diffuses from the bulk due to the low carbon solubility of Cu, and the secondary graphene layers cease to grow. It follows that the bilayer growth would be "self-limited" in this case.[31] The relative growth rate of the adlayers to the first layer is thought to be dependent on the cooling rate. Low cooling rates (~18-20 °C/min) were speculated to promote secondary adlayers to grow; however, it is not clear whether the secondary layers are formed from carbon diffusing from the bulk or depositing from the gas phase (the samples were cooled in Ar flow, but no purge of the methane is indicated).[9]

Various pretreatments have been developed to improve the quality of CVD graphene on Cu. Annealing the Cu foil in hydrogen and argon is thought to reduce the defect density

of graphene grown by CVD using methane.[37] After hydrogen and argon annealing, copper oxide nanoparticles (~1-50 nm in size) form with densities of ~1 x 10^4/mm^2.[35,36] A recent study demonstrated that only particles greater than 20 nm were participating as nucleation points for graphene growth.[36] In another study, effect of hydrogen partial pressure was studied during the growth phase. No graphene growth was observed in the absence of hydrogen, whereas, discontinuous bilayer graphene to large grain single domain graphene growth was observed at increasing partial pressures of hydrogen.[12]

The graphene film samples were prepared by first annealing the Cu foil in hydrogen at intermediate pressure (300 Torr) at high flow rate (1000 sccm) at 800 °C, followed by growing graphene with a high methane concentration (100%) and high methane flow rate (50 sccm), then cooling the sample in hydrogen from the growth temperature to room temperature. Continuous and uniform bilayer graphene growth over the entire 3 cm x 5 cm foil was observed, with all of the nucleation particles above the critical 20 nm size and with a density of ~10^7/mm^2, a factor of 1000x higher than that of the previous studies mentioned. The graphene growth achieved full coverage in about one-fifth the time due to the high nucleation density. The high methane concentration during the growth phase was shown theoretically to encourage high nucleation density in a first principles study.[38]

Cooling the samples in vacuum permits the self-limiting mechanism to occur, where carbon more readily attaches at the growing graphene grain edges. Some carbon diffuses from the bulk to the secondary or tertiary layers, but the growth ceases before these layers can achieve complete coverage. Hydrogen was observed to activate surface bound carbon

for vertical growth in atmospheric-pressure CVD of graphene from an acetylene precursor on Cu foil.[39] Hydrogen in the cooling phase may be bonding to the edges of the growing graphene layers, allowing the free carbon species to migrate and form adlayers by bulk diffusion or adsorbing on top of the first layer and migrating to the next available

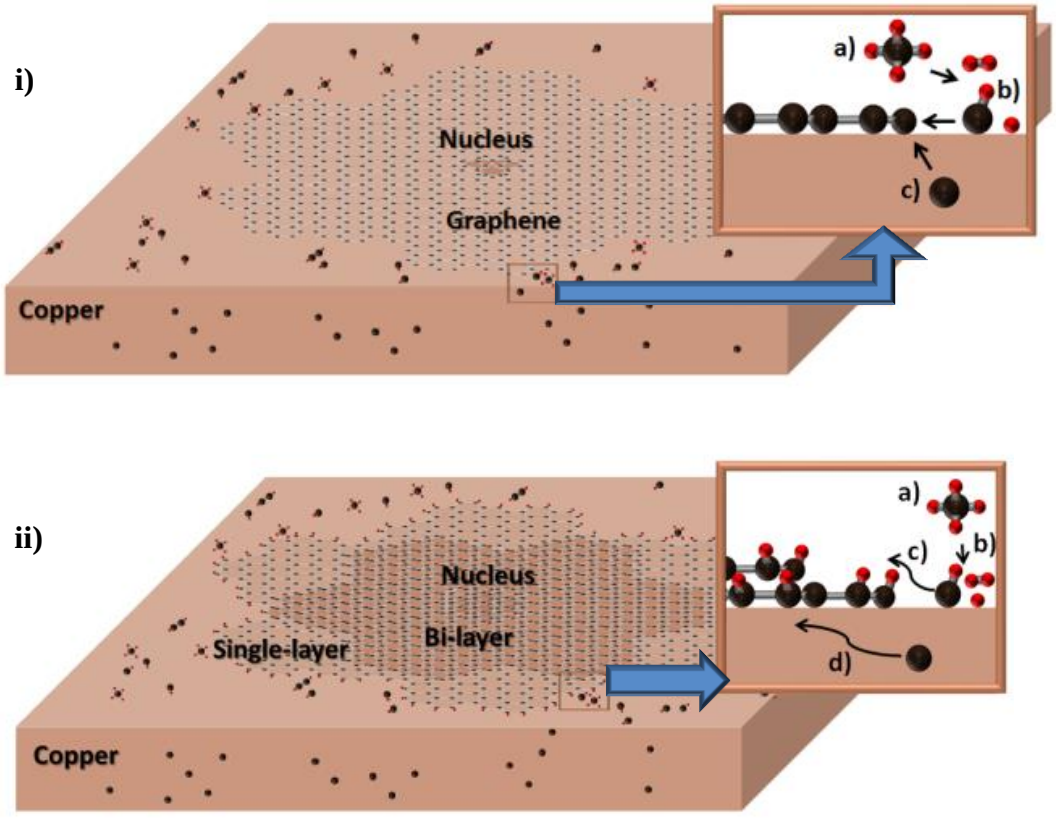


Figure 3.14. Illustration of (i) vacuum-cooled single-layer and (ii) hydrogen-cooled bilayer graphene growth mechanism. For vacuum-cooled CVD, graphene grows from the initial nucleation point, forming a bi or few-layer nucleus with surrounding single-layer grains. Methane (a) is decomposed into CH_x species at the Cu surface (b), attaching readily to the free carbon on the edges of the growing single-layer grains. Carbon from the Cu bulk may also diffuse to the surface to attach to the carbon on the grain edges (c). In the hydrogen-cooled process, free hydrogen is likely to bond to the edges of the graphene grains. Methane (a) is decomposed into CH_x species at the Cu surface (b), but will more likely encounter hydrogen-terminated graphene edges, and will either hop over (c) and contribute to the growing bilayer, or form a separate new graphene nucleus somewhere else on the Cu surface with other CH_x species. Again, carbon from the Cu bulk may also diffuse to the surface to attach to the carbon on the grain edges (d).

layer (Fig. 3.14). This may also be the cause of the observed increased nucleation density for the hydrogen-cooled graphene, as CH_x species that are unable to hop to form adlayers likely form new single-layer nuclei on the free Cu surface. These proposed mechanisms for adlayer growth are supported by recent theoretical investigations indicating the role of hydrogen in promoting bilayer growth by restricting lateral growth of graphene via edge termination.[40]

3.5 Conclusions

In this chapter, graphene was introduced as an important nanostructured carbon material for various applications, and it was shown that there need for improved synthesis methods for large area graphene with controlled layer number in a fast process. An experimental study on the effect of cooling phase gases on graphene growth mechanics was described, and it was observed that the cooling phase gases may be used to reproducibly grow continuous and uniform single- or bilayer graphene on Cu foils by the thermal CVD process. It was found that the hydrogen cooling encouraged the growth of bilayer graphene, whereas vacuum cooling resulted in predominantly single-layer graphene. These results are important for the development of graphene synthesis for various applications.

3.6 Acknowledgements

Chapter 3 was reprinted (adapted) from (Gulotty, R.; Das, S.; Liu, Y.; Sumant, A. V. Effect of Hydrogen Flow during Cooling Phase to Achieve Uniform and Repeatable Growth of Bilayer Graphene on Copper Foils over Large Area. *Carbon* **2014**, *77*, 341–350.) © (2014), with permission from Elsevier. This work was performed at the Center

for Nanoscale Materials at Argonne National Laboratory. Use of the Center for Nanoscale Materials was supported by the U.S. Department of Energy, Office of Science, Office of Basic Energy Sciences, under Contract No. DE-AC02-06CH11357.

REFERENCES AND NOTES

(1) Geim, A. K.; Novoselov, K. S. The Rise of Graphene. *Nat. Mater.* **2007**, *6*, 183–191.

(2) Bolotin, K. I.; Sikes, K. J.; Jiang, Z.; Klima, M.; Fudenberg, G.; Hone, J.; Kim, P.; Stormer, H. L. Ultrahigh Electron Mobility in Suspended Graphene. *Solid State Commun.* **2008**, *146*, 351–355.

(3) Lee, C.; Wei, X.; Kysar, J. W.; Hone, J. Measurement of the Elastic Properties and Intrinsic Strength of Monolayer Graphene. *Science* **2008**, *321*, 385–388.

(4) Wang, X.; Zhi, L.; Müllen, K. Transparent, Conductive Graphene Electrodes for Dye-Sensitized Solar Cells. *Nano Lett.* **2008**, *8*, 323–327.

(5) Balandin, A. A.; Ghosh, S.; Bao, W.; Calizo, I.; Teweldebrhan, D.; Miao, F.; Lau, C. N. Superior Thermal Conductivity of Single-Layer Graphene. *Nano Lett.* **2008**, *8*, 902–907.

(6) Zhang, Y.; Tang, T.-T.; Girit, C.; Hao, Z.; Martin, M. C.; Zettl, A.; Crommie, M. F.; Shen, Y. R.; Wang, F. Direct Observation of a Widely Tunable Bandgap in Bilayer Graphene. *Nature* **2009**, *459*, 820–823.

(7) Losurdo, M.; Giangregorio, M. M.; Capezzuto, P.; Bruno, G. Graphene CVD Growth on Copper and Nickel: Role of Hydrogen in Kinetics and Structure. *Phys. Chem. Chem. Phys.* **2011**, *13*, 20836–20843.

(8) Liu, L.; Zhou, H.; Cheng, R.; Yu, W. J.; Liu, Y.; Chen, Y.; Shaw, J.; Zhong, X.; Huang, Y.; Duan, X. High-Yield Chemical Vapor Deposition Growth of High-Quality Large-Area AB-Stacked Bilayer Graphene. *ACS Nano* **2012**, *6*, 8241–8249.

(9) Lee, S.; Lee, K.; Zhong, Z. Wafer Scale Homogeneous Bilayer Graphene Films by Chemical Vapor Deposition. *Nano Lett.* **2010**, *10*, 4702–4707.

(10) Wu, Y.; Chou, H.; Ji, H.; Wu, Q.; Chen, S.; Jiang, W.; Hao, Y.; Kang, J.; Ren, Y.; Piner, R. D.; et al. Growth Mechanism and Controlled Synthesis of AB-Stacked Bilayer Graphene on Cu-Ni Alloy Foils. *ACS Nano* **2012**, *6*, 7731–7738.

(11) Liu, W.; Li, H.; Xu, C.; Khatami, Y.; Banerjee, K. Synthesis of High-Quality Monolayer and Bilayer Graphene on Copper Using Chemical Vapor Deposition. *Carbon N. Y.* **2011**, *49*, 4122–4130.

(12) Vlassiouk, I.; Regmi, M.; Fulvio, P.; Dai, S.; Datskos, P.; Eres, G.; Smirnov, S. Role of Hydrogen in Chemical Vapor Deposition Growth of Large Single-Crystal Graphene. *ACS Nano* **2011**, *5*, 6069–6076.

(13) Qi, M.; Ren, Z.; Jiao, Y.; Zhou, Y.; Xu, X.; Li, W.; Li, J.; Zheng, X.; Bai, J. Hydrogen Kinetics on Scalable Graphene Growth by Atmospheric Pressure Chemical Vapor Deposition with Acetylene. *J. Phys. Chem. C* **2013**, *117*, 14348–14353.

(14) Zhang, X.; Ning, J.; Li, X.; Wang, B.; Hao, L.; Liang, M.; Jin, M.; Zhi, L. Hydrogen-Induced Effects on the CVD Growth of High-Quality Graphene Structures. *Nanoscale* **2013**, *5*, 8363–8366.

(15) Xiao, K.; Wu, H.; Lv, H.; Wu, X.; Qian, H. The Study of the Effects of Cooling Conditions on High Quality Graphene Growth by the APCVD Method. *Nanoscale* **2013**, *5*, 5524–5529.

(16) Li, X.; Magnuson, C. W.; Venugopal, A.; Tromp, R. M.; Hannon, J. B.; Vogel, E. M.; Colombo, L.; Ruoff, R. S. Large-Area Graphene Single Crystals Grown by Low-Pressure Chemical Vapor Deposition of Methane on Copper. *J. Am. Chem. Soc.* **2011**, *133*, 2816–2819.

(17) Lin, Y.-C.; Jin, C.; Lee, J.-C.; Jen, S.-F.; Suenaga, K.; Chiu, P.-W. Clean Transfer of Graphene for Isolation and Suspension. *ACS Nano* **2011**, *5*, 2362–2368.

(18) Kim, Y.; Lee, J.; Yeom, M. S.; Shin, J. W.; Kim, H.; Cui, Y.; Kysar, J. W.; Hone, J.; Jung, Y.; Jeon, S.; et al. Strengthening Effect of Single-Atomic-Layer Graphene in Metal-Graphene Nanolayered Composites. *Nat. Commun.* **2013**, *4*, 2114.

(19) Malard, L. M.; Pimenta, M. a.; Dresselhaus, G.; Dresselhaus, M. S. Raman Spectroscopy in Graphene. *Phys. Rep.* **2009**, *473*, 51–87.

(20) Poncharal, P.; Ayari, a.; Michel, T.; Sauvajol, J.-L. Raman Spectra of Misoriented Bilayer Graphene. *Phys. Rev. B* **2008**, *78*, 113407.

(21) Morozov, S.; Novoselov, K.; Katsnelson, M.; Schedin, F.; Elias, D.; Jaszczak, J.; Geim, a. Giant Intrinsic Carrier Mobilities in Graphene and Its Bilayer. *Phys. Rev. Lett.* **2008**, *100*, 016602.

(22) Latil, S.; Meunier, V.; Henrard, L. Massless Fermions in Multilayer Graphitic Systems with Misoriented Layers: Ab Initio Calculations and Experimental Fingerprints. *Phys. Rev. B* **2007**, *76*, 201402.

(23) Sui, Y.; Appenzeller, J. Screening and Interlayer Coupling in Multilayer Graphene Field-Effect Transistors. *Nano Lett.* **2009**, *9*, 2973–2977.

(24) Nair, R. R.; Blake, P.; Grigorenko, A. N.; Novoselov, K. S.; Booth, T. J.; Stauber, T.; Peres, N. M. R.; Geim, A. K. Fine Structure Constant Defines Visual Transparency of Graphene. *Science* **2008**, *320*, 1308.

(25) Das, A.; Pisana, S.; Chakraborty, B.; Piscanec, S.; Saha, S. K.; Waghmare, U. V; Novoselov, K. S.; Krishnamurthy, H. R.; Geim, A. K.; Ferrari, A. C.; et al. Monitoring Dopants by Raman Scattering in an Electrochemically Top-Gated Graphene Transistor. *Nat. Nanotechnol.* **2008**, *3*, 210–215.

(26) Chen, Z.; Wang, X.-Q. Stacking-Dependent Optical Spectra and Many-Electron Effects in Bilayer Graphene. *Phys. Rev. B* **2011**, *83*, 081405.

(27) Wang, Y.; Ni, Z.; Liu, L.; Liu, Y.; Cong, C.; Yu, T.; Wang, X.; Shen, D.; Shen, Z. Stacking-Dependent Optical Conductivity of Bilayer Graphene. *ACS Nano* **2010**, *4*, 4074–4080.

(28) Kim, Y. D.; Bae, M.-H.; Seo, J.-T.; Kim, Y. S.; Kim, H.; Lee, J. H.; Ahn, J. R.; Lee, S. W.; Chun, S.-H.; Park, Y. D. Focused-Laser-Enabled P-N Junctions in Graphene Field-Effect Transistors. *ACS Nano* **2013**, *7*, 5850–5857.

(29) Liu, M.; Yin, X.; Ulin-Avila, E.; Geng, B.; Zentgraf, T.; Ju, L.; Wang, F.; Zhang, X. A Graphene-Based Broadband Optical Modulator. *Nature* **2011**, *474*, 64–67.

(30) Bao, J.; Xing, S.; Wang, Y.; Wu, W.; Robles-Hernandez, F.; Pei, S. Fabrication of Large-Area Twisted Bilayer Graphene for High-Speed Ultra-Sensitive Tunable Photodetectors. *Proc. SPIE* **2013**, *8725*, 872503.

(31) Li, X.; Cai, W.; An, J.; Kim, S.; Nah, J.; Yang, D.; Piner, R.; Velamakanni, A.; Jung, I.; Tutuc, E.; et al. Large-Area Synthesis of High-Quality and Uniform Graphene Films on Copper Foils. *Science* **2009**, *324*, 1312–1314.

(32) Tao, L.; Lee, J.; Chou, H.; Holt, M.; Ruoff, R. S.; Akinwande, D. Synthesis of High Quality Monolayer Graphene at Reduced Temperature on Hydrogen-Enriched Evaporated Copper (111) Films. *ACS Nano* **2012**, *6*, 2319–2325.

(33) Kim, K.; Coh, S.; Tan, L. Z.; Regan, W.; Yuk, J. M.; Chatterjee, E.; Crommie, M. F.; Cohen, M. L.; Louie, S. G.; Zettl, a. Raman Spectroscopy Study of Rotated Double-Layer Graphene: Misorientation-Angle Dependence of Electronic Structure. *Phys. Rev. Lett.* **2012**, *108*, 246103.

(34) Ni, Z.; Wang, Y.; Yu, T.; You, Y.; Shen, Z. Reduction of Fermi Velocity in Folded Graphene Observed by Resonance Raman Spectroscopy. *Phys. Rev. B* **2008**, *77*, 235403.

(35) Yan, Z.; Lin, J.; Peng, Z.; Sun, Z.; Zhu, Y.; Li, L.; Xiang, C.; Samuel, E. L.; Kittrell, C.; Tour, J. M. Toward the Synthesis of Wafer-Scale Single-Crystal Graphene on Copper Foils. *ACS Nano* **2012**, *6*, 9110–9117.

(36) Gan, L.; Luo, Z. Turning off Hydrogen To Realize Seeded Growth of Subcentimeter Single-Crystal Graphene Grains on Copper. *ACS Nano* **2013**.

(37) Tao, L.; Holt, M.; Lee, J.; Chou, H.; McDonnell, S. J.; Ferrer, D. A.; Babenco, M.; Wallace, R. M.; Banerjee, S. K.; Ruoff, R. S.; et al. Uniform Wafer-Scale Synthesis of Graphene on Evaporated Cu (111) Film with Quality Comparable to Exfoliated Monolayer. **2012**.

(38) Zhang, W.; Wu, P.; Li, Z.; Yang, J. First-Principles Thermodynamics of Graphene Growth on Cu Surfaces. *J. Phys. Chem. C* **2011**, *115*, 17782–17787.

(39) Qi, M.; Ren, Z.; Jiao, Y.; Zhou, Y.; Xu, X.; Li, W.; Li, J.; Zheng, X.; Bai, J. Hydrogen Kinetics on Scalable Graphene Growth by Atmospheric Pressure Chemical Vapor Deposition with Acetylene. *J. Phys. Chem. C* **2013**, *117*, 14348–14353.

(40) Zhang, X.; Wang, L.; Xin, J.; Yakobson, B. I.; Ding, F. Role of Hydrogen in Graphene Chemical Vapor Deposition Growth on a Copper Surface. *J. Am. Chem. Soc.* **2014**.

Chapter 4. CVD Synthesis of Large Area Uniform R-GO-like Carbon Films with Excellent Thermal and Electrical Conductivity and Optical Transparency

4.0 Abstract

Reduced graphene oxide (R-GO) thin films have been developed for applications such as transparent conducting electrodes as well as flexible lateral heat spreaders. But high thermal and electrical conductivity have not been achieved due to the disordered nature of the flakes in conventional R-GO films. In this chapter the direct synthesis and deposition of large area (1" x 1") uniform and continuous reduced graphene oxide like carbon (R-GOC) films via thermal CVD using methane as the precursor gas, without the use of a metal catalyst film is demonstrated and characterized. The optical transmittance of the films reaches 81.2 ± 0.2 %, with sheet resistances as low as 4.0 x 10^2 ± 65 Ω/□. The thermal conductivity of the R-GOC material measured via laser flash and optothermal techniques falls in the range of 70-115 W/m-K. It was found through transmission electron microscopy that the synthesized R-GOC films are composed of nanoscale carbon clusters. Raman spectroscopy of the R-GOC shows features similar to R-GO. The electron energy loss spectroscopy (EELS) indicates the carbon in the R-GOC film is 31 to 52%. sp^3 bonded. Near edge X-ray absorption fine structure (NEXAFS) analysis indicates the carbon in the R-GOC film is 48 to 69% sp^3 bonded. In addition NEXAFS reveals the presence of carbon-oxygen bonds in the R-GOC film. X-ray photoelectron

spectroscopy (XPS) indicates the atomic % of oxygen in the films is ~14%, confirming also the presence of carbon-oxygen bonds. The experimental results of the thermal, optical, and electrical characterization suggest that the R-GOC films may have application as a transparent conducting electrode or lateral heat spreading material.

4.1 Introduction

Controllable and sustainable processes for large-scale growth of high-quality graphene have been investigated for years since the mechanical exfoliation method was introduced.[1] This is because the superior electrical, thermal, optical, and mechanical properties graphene possesses make it an attractive material for various applications.[2–5] Graphene films possess superior optical transparency and electrical conductance than commercially applied transparent conducting films such as indium tin oxide (ITO). Chemical vapor deposition (CVD) has been studied extensively and demonstrated to yield polycrystalline graphene from centimeter to near-meter area on metallic thin films and foils with layer number uniformity.[6–9] Recently uniform reduced graphene oxide (R-GO) was synthesized at reduced temperature by using slow diffusion of carbon through Cu from a solid carbon source.[10] However, direct deposition of graphene onto non-metallic substrates (such as dielectric or polymeric materials) has been a major challenge, as a metallic catalyst such as copper or nickel is required to decompose methane into sp^2 bonded carbon, and polymeric materials cannot survive the high process

temperatures of CVD. For all practical applications of CVD graphene the metallic catalyst must be etched away after the growth, and generally a polymeric handle is required for support during the etching. The polymeric handle and its accompanying residue are not easily removed, especially when a free-standing film is the final desired structure. There are no reported direct deposition methods for large area, uniform graphene films on non-metallic substrates in the absence of a metallic catalyst film.[11] Various indirect methods have been developed to achieve graphene thin films on arbitrary substrates. In the conventional Hummer's method bulk graphite is exfoliated into a liquid dispersion of nanoscale graphene oxide (GO) sheets using $KMnO_4$ and $NaNO_3$ in concentrated H_2SO_4.[12] The GO nanosheets can be reduced chemically while dispersed in a solution, or after deposition on the target substrate by thermal annealing. Deposition is carried out by spin or dip coating the dispersion of flakes onto the target substrate.

The film that results from the Hummer's method and subsequent deposition is composed of nanosheets that vary in size, shape, thickness, and degree of reduction. Flakes in these films partially overlap forming random junctions, resulting in non-uniform electrical conduction (see Figure 4.1).[13] The thermal and electrical conductivity of R-GO flakes produced by chemical or thermal reduction are substantially decreased due to the introduction of lattice defects during the chemical reduction process.[14]

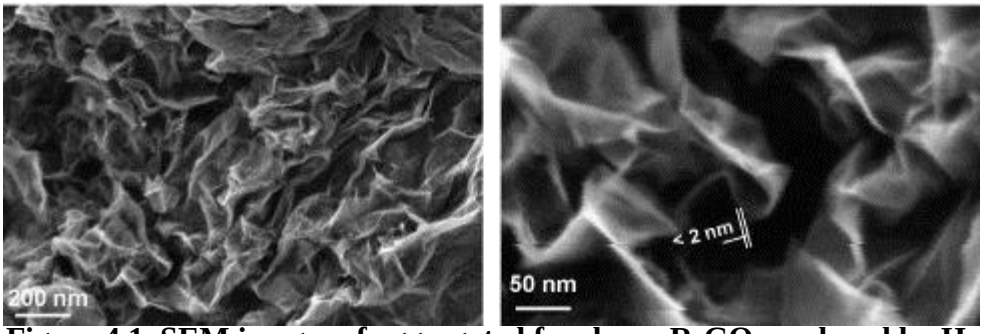


Figure 4.1. SEM images of aggregated few-layer R-GO produced by Hummers method. Flakes of variable layer number and size are observed to form random junctions. © 2007 Elsevier. Reprinted, with permission, from [Stankovich, S.; Dikin, D. A.; Piner, R. D.; Kohlhaas, K. A.; Kleinhammes, A.; Jia, Y.; Wu, Y.; Nguyen, S. T.; Ruoff, R. S. Synthesis of Graphene-Based Nanosheets via Chemical Reduction of Exfoliated Graphite Oxide. *Carbon* 2007.][15]

Some methods combine direct and indirect methods to achieve large area crystalline R-GO films. Large area R-GO films were deposited by seeded growth CVD from GO flakes on Cu.[16] A recent process neglected the copper catalyst and deposited graphitic amorphous carbon directly onto substrates, but this deposition was at relatively high temperature (1100 ºC).[17] Electrophoretic methods have been demonstrated for improving the uniformity and scalability of deposition of GO flakes from solution, but separate reduction treatment at high temperature (~1000 ºC) is still required to achieve high electrical conductivity, and the film is no longer transparent at the thicknesses (>500 nm) deposited by EPM, and the electrode of deposition, (the target substrate) must be electrically conductive (ex. Cu).[11]

In this chapter the synthesis and characterization of reduced graphene oxide like carbon (R-GOC) films via direct CVD onto quartz and silicon dioxide substrates without additional catalysts (see Figure 4.2), as well as onto Cu for ease of transfer to TEM grids

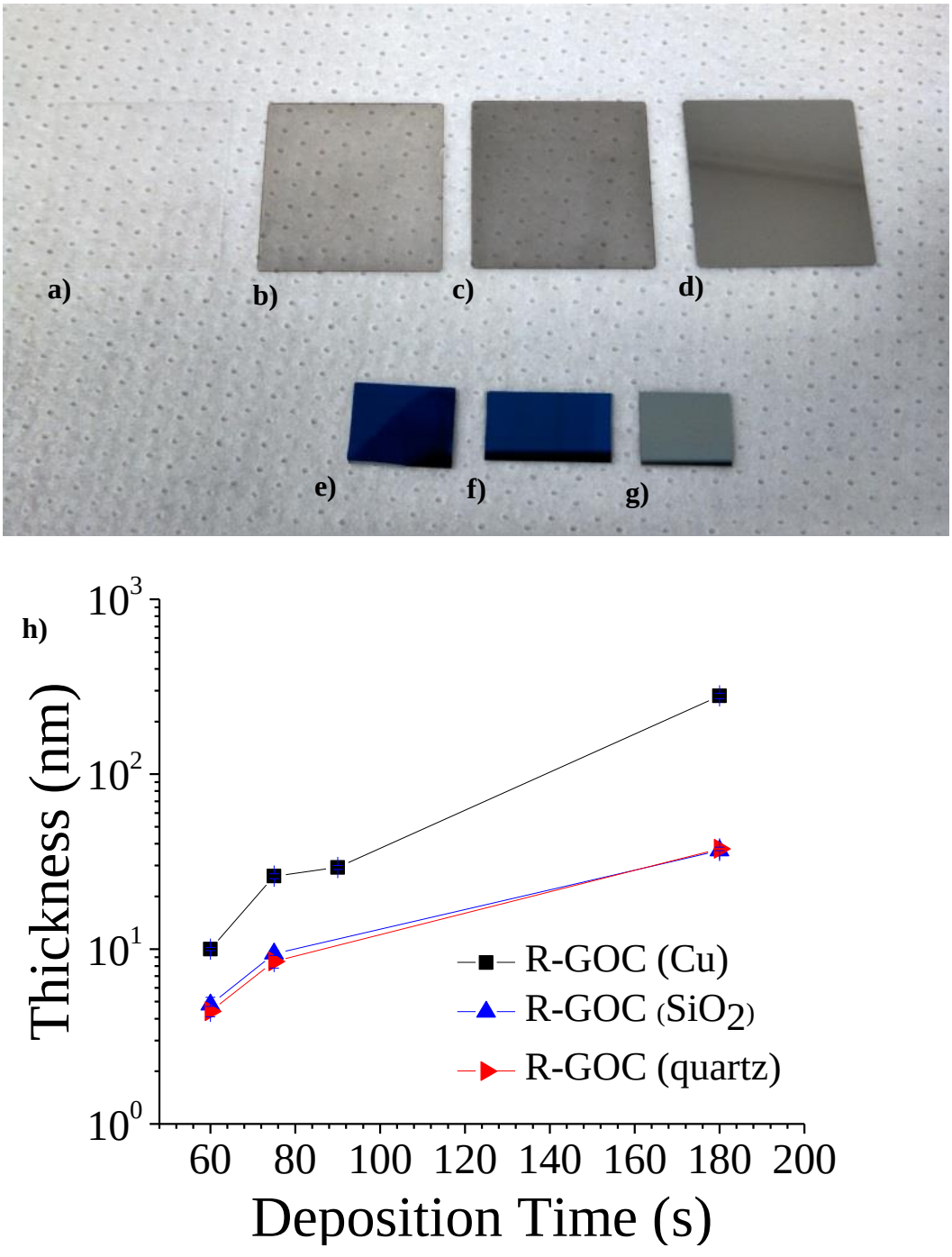


Figure 4.2. Optical image of blank quartz substrate (a), R-GOC on quartz with thickness 4.8 nm (b), 9.4 nm (c), 36.6 nm (d), R-GOC on SiO_2 substrates with thickness 4.4 nm (e), 8.5 nm (f), and 37.4 (g). Film thickness with deposition time for Cu, SiO_2, and quartz substrates (h).

is described. The reported synthesis method is area-scalable to the size of the CVD system and substrate, and the film thickness for the R-GOC deposition is tunable via controlling the precursor gas flow rate and deposition time (see Figure 4.2b). The films synthesized may offer the optimal combination of thermal and electrical conduction and optical transparency for various applications.

4.2 Experimental Methods

Cu foil (Alfa Aesar 25 mm, 99.8%) was cut into strips and placed in the CVD tube. The tube was purged to 10 mTorr in nitrogen. Then the temperature was ramped to 950 ºC in 1000 sccm H_2 and 1000 sccm Ar, until the tube pressure reaches 300 Torr, then Ar flow is ceased. At 950 ºC, the H_2 flow is ceased and the tube is purged to 1 Torr. The pressure setpoint is set to 300 Torr, and methane is introduced at 1000 sccm flow for 30 seconds, followed by 30 seconds of 100sccm flow. The pressure in the chamber reaches ~50 Torr during the deposition. Longer flow times at higher pressures result in thicker films according to Figure 4.2b. The same process was followed, with adjusted precursor gas flow durations to tune the film thickness, for the SiO_2 and quartz substrate samples. A lower temperature process was run at 850 ºC in the same substrate configuration, but with ethylene flow at 300 sccm, pressure set point at 300 Torr, for 75 s. The pressure increases steadily to 30 Torr during the deposition as the ethylene flows. For all samples the cooling from the deposition step is at 300 Torr and 1000 sccm hydrogen flow, with an additional

1000 sccm of argon flowed during the initial ramp to 300 Torr. The samples are removed in nitrogen at ≤ 100 ºC.

The R-GOC films grown on Cu were transferred from Cu to substrates for electrical and optical characterization, EELS, TEM, SAED, and AFM. The Cu foil was backside-etched using oxygen plasma reactive ion etching, (100 W, 5 minutes, 164 mTorr, 24sccm O_2); Raman spectroscopy was used to confirm the etching. Ferric chloride acid was used to etch the copper away for ~10 minutes, and a clean piece of SiO_2/Si was submerged into the acid bath to retrieve the R-GOC films and place them into water for a minute. The rinse was repeated with two fresh baths of water, a minute each. Then, the characterization substrate (SiO_2/Si, TEM grids, quartz) was submerged into the water bath to retrieve the R-GOC film. The substrates were baked at 115 ºC to remove the water for several min. The drying was confirmed with optical microscopy.

The four point probe method was used to determine the sheet resistance (in $\Omega/\square$) of the R-GOC films.

A micro-Raman spectrometer was used 514 nm excitation at variable power on the prepared TEM grid samples, as well as on SiO_2/Si and quartz slides. The laser power was optimized for signal-to-noise ratio and to prevent damage to the samples during the measurement. SEM images were taken at 5 kV and ~5 mm working distance. Light

transmittance tests were carried out using a UV/VIS spectrophotometer. EELS and SAED was completed on the TEM samples during the TEM.

To perform the measurement of the thermal conductivity with LFT, each sample was placed into a stage designed for in-plane diffusivity measurement. A circular opening in the stage allows the backside of the sample to be illuminated by the flash of a xenon lamp. A metal mask with openings a known lateral distance from the outer diameter of the exposed area is used to remove the cross-plane signal and measure the in-plane diffusivity signal. The cryogenically cooled InSb Ir detector detects the temperature rise of the top surface of the sample as a function of time, which allows the thermal diffusivity to be determined. The thermal conductivity, *k*, in W/m-K, is calculated from the equation:

$$k = \alpha \rho c_p \tag{5}$$

Where α is diffusivity (m^2/s), ρ is density (kg/m^3), and c_p is the specific heat ($J\ kg^{-1}\ K^{-1}$). The specific heat was obtained from the laser flash calorimetry.[18] The method requires a reference sample of known heat capacity and similar thermo-physical properties. In our case, the copper foil without the R-GOC film was used as reference. An assumption was made that the reference sample and the test sample absorb equal amounts of energy from equal light flashes. Further details of the laser flash measurement procedures have been reported elsewhere.[19–21]

The optothermal technique is another method to determine the thermal conductivity of a material. In our case the R-GOC film (10 nm thick) was suspended in air on copper and silicon TEM grids that had square meshes of 50 and 100 μm, respectively. The Raman laser (514 nm) was used as the heat source for the steady state measurements while the temperature of the samples was controlled using a cryogenically cooled cell and heated sample stage with nitrogen gas purging. The Raman also acts as a thermometer in the optothermal method, as the Raman G peak position is used to determine the temperature at the heat source in the steady state at variable laser power. Further details of the optothermal technique in the context of other material systems is available elsewhere.[3]

The R-GOC film was suspended on Cu TEM grid for NEXAFS characterization. More details on NEXAFS technique have been reported elsewhere.[22]

4.3 Results of the Experiments

Thermal CVD experiments were performed with methane as the precursor gas with variable deposition times on Cu, SiO_2, and quartz substrates (See Figure 4.2b). AFM was used to find the thickness of the deposited R-GOC films (see Figure 4.3 and Appendix A) The thickness is tunable via the deposition time.

The light transmission of the CVD-grown R-GOC films reached a maximum of 81.2 ± 0.2 % transparent at 514 nm for the 4.8 ± 0.5 nm thick film on quartz, with sheet resistance

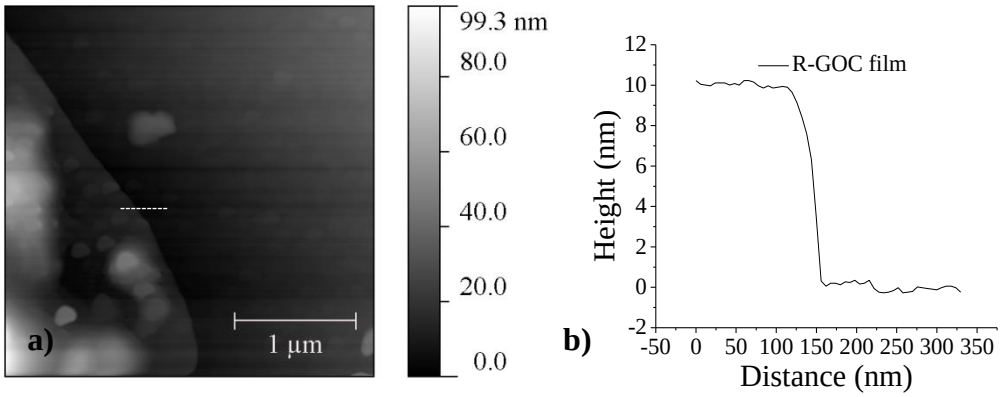


Figure 4.3. AFM map of R-GOC film deposited on Cu, then transferred to SiO_2 (a), AFM line profile (b). The film thickness is 10.0 ± 0.2 nm.

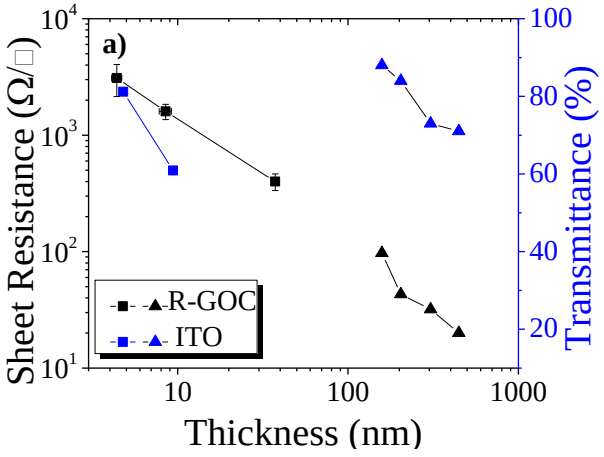


Figure 4.4. Comparison of visible transmittance (at 514 nm) and sheet resistance of CVD R-GOC films with literature values of ITO[23] for comparison.

of 7.3± 0.8 kΩ/□, and a minimum of 4.0 x 10^2 ± 65 Ω/□ sheet resistance for the 37.4 ± 0.9 nm thick R-GOC on SiO_2 (see Figure 4.4 and 4.5).

Raman characterization was carried out on the synthesized R-GOC films (see Figure 4.6). The spectra of graphitic materials is composed of the D, G, 2D, and D+D' peaks

(typically located at ~1350cm^{-1}, 1585cm^{-1}, 2700cm^{-1}, and 2800cm^{-1} respectively).[24] The R-GOC films Raman spectra (see Figure 4.6) matched the literature values for R-GO, with the D peak ~1362cm^{-1}, the G peak at ~1585cm^{-1}, and the 2D peak ~2700.[25,26] Similar spectra were observed for the R-GOC deposited on quartz and SiO_2.

In order to further determine the nanostructure of the films, transmission electron microscopy, selected area electron diffraction (SAED), and electron energy loss spectroscopy (EELS) was carried out on films transferred to TEM grids (see Figure 4.7). From the TEM we conclude that R-GOC films are composed of nanoscale clusters of carbon. All three SAED indicate amorphous carbon. This is not surprising as the spot size for SAED of one micron contains many clusters of R-GOC.

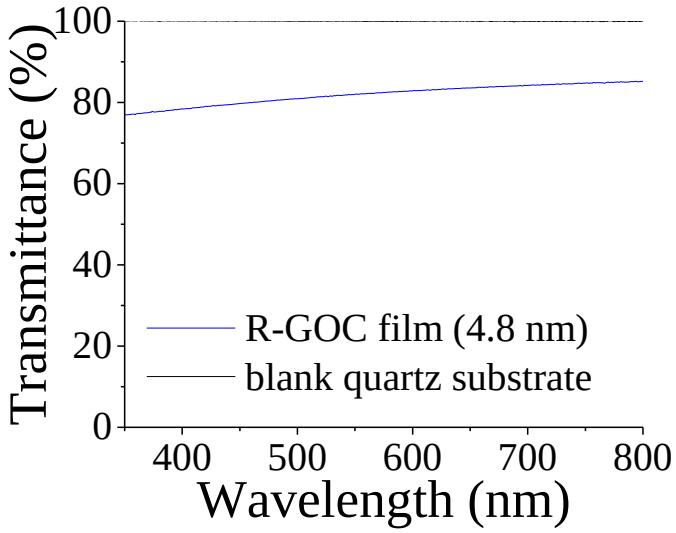


Figure 4.5. UV-visible light transmittance of R-GOC film (4.8 nm) on quartz and blank quartz substrate as control (black solid line).

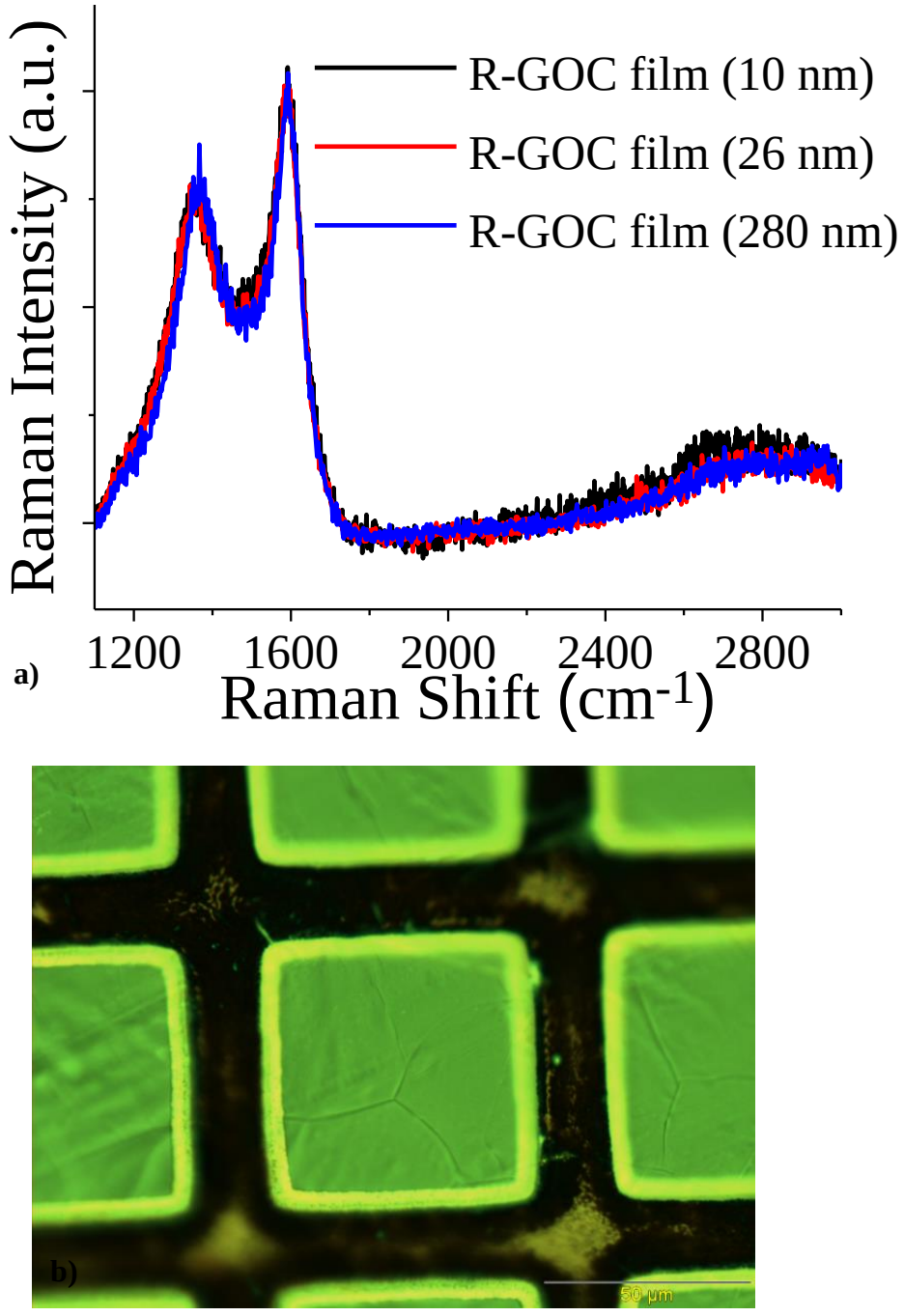


Figure 4.6. Typical Raman spectra of R-GOC films suspended in air on TEM grids (a), Optical image of R-GOC film (10 nm thick) suspended on Cu TEM grid (scale bar is 50 µm) (b) .

The EELS spectra of each film is shown in Figure 4.7g. The relative fraction of sp^2 to sp^3 bonding can be interpreted from these spectra by first defining $R_{A,}$ the ratio of the integrated area of the first 2 peaks, P_1 and P_2 to the third peak, P_3:

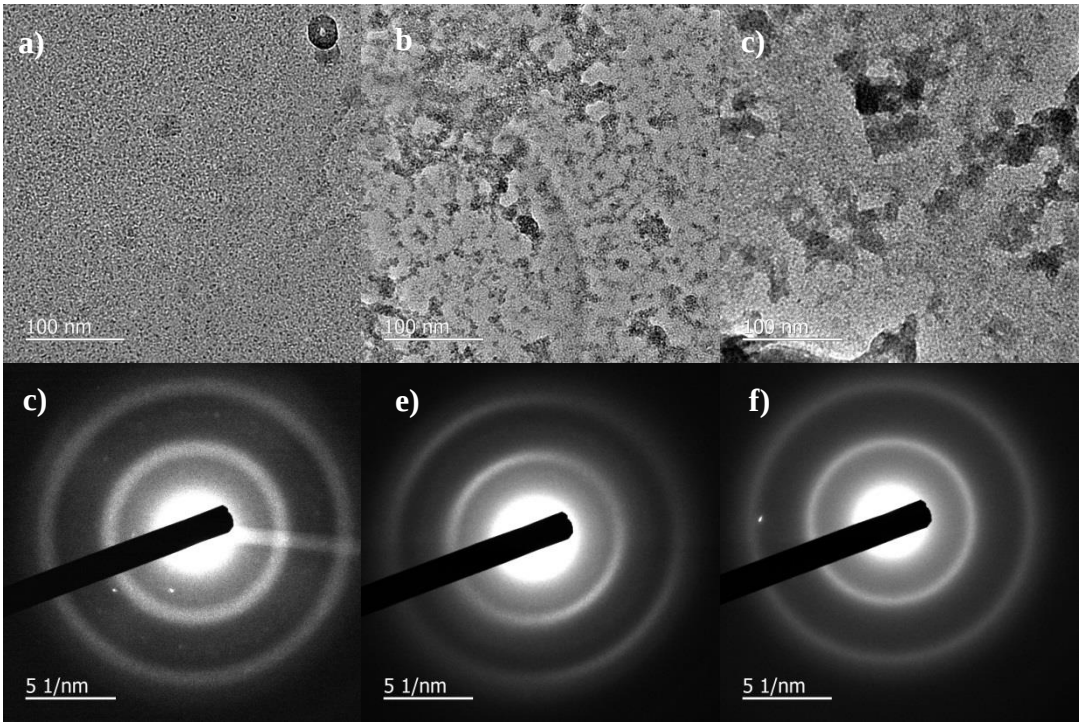
$$R_A = \frac{A(P_1+P_2)}{A(P_1+P_2+P_3)}.\ ^{27} \quad (1)$$

Then the *R* is compared to the *R* of graphite, R_{Gr} to determine *x*, the relative sp^3 fraction by the following relation:

$$R_A = R_{Gr}(1-x).\ ^{27} \quad (2)$$

From this equation, $x = 0$ (0%) for graphite and $x = 1$ (100%) for diamond. The R-GOC films have similar % sp^3 to one another based on the EELS analysis (see Table 4.1).

Two R-GOC films were transferred to Cu TEM grids for near edge X-ray absorption fine structure (NEXAFS) characterization (Figure 4.8). The relative concentration of oxygen bonds present in each film may be inferred from the relative intensity of the peaks at 288.4 and 531.4 eV.[28] The thickness of the films was determined by comparing the measured optical density of each film to the theoretical elemental X-ray absorption profile of graphitic material with density of 1.8 g/cm^3 (see Table 4.2). The same analysis used for EELS may be used to extract the percent of sp^3 bonded carbon. The results of these analyses are given in Table 4.2.



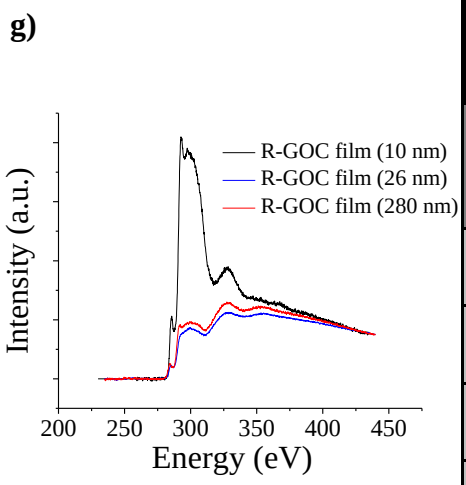


Table 4.1 – sp^3 content of R-GOC films from EELS

Film	R_A	% sp^3	Thickness (nm)
R-GOC	0.19	31	10.0 ± 0.2
R-GOC	0.14	48	26.1 ± 0.8
R-GOC	0.13	52	280.3 ±10.3
Graphite	0.28	0	--
Diamond	0	100	--

Figure 4.7. TEM, SAED, and EELS of R-GOC films 10 nm (a, d, g), 26 nm (b, e, g) and 280 nm (c, f, g) thick. Table 2 gives the fraction of sp^3 content of the R-GOC films extracted from the EELS.

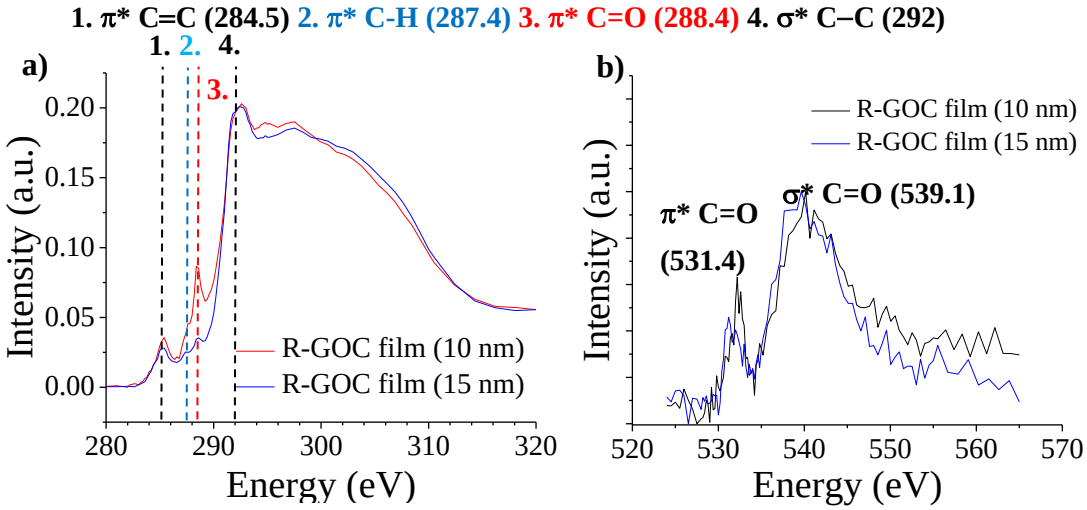


Table 4.2 –NEXAFS analysis of R-GOC film s

Film	R_A	% sp^3	Thickness (nm)	I_{π^*} C=O (288.4 eV)	I_{π^*} C=O (531.4 eV)
R-GOC	0.14	48	10	1	1
R-GOC	0.09	69	15	0.42	0.90
Graphite	0.28	0	--	--	--
Diamond	0	100	--	--	--

Figure 4.8. Normalized NEXAFS spectra of 10 and 15 nm thick R-GOC films and at C-K edge a), and O-K edge b). Table 4.2 gives the sp^3 content, thickness, and relative integrated area of π* C=O bond peaks of the R-GOC films as measured from the C-K and O-K edges, with the 10 nm thick film assigned unity.

X-ray photoemission spectroscopy (XPS) analysis was performed by a home-built X-ray photoelectron spectrometer, which includes a hemispherical electron energy analyzer of 0.9 eV energy resolution and a non-monochromated Mg K-alpha soft x-ray source at 1253 eV.

Figure 4.9 shows X-ray photon spectroscopy (XPS) analysis for the 10 nm thick R-GOC sample A transferred on the $Au/SiO_2/Si$. The survey scan (Figure 4.9a) indicates the presence of oxygen on the surface of the sample in very small amount (14.5 atomic % of oxygen in comparison to 85.5 atomic % of carbon). The high-resolution C 1s spectra indicates that most of the carbon forms C-C bonds (at 284.6 eV) while only small amount of oxygen is bonded to carbon, as indicated by C-O and C=O peaks at 286.8 eV and 289.8 eV respectively. Such a small oxygen amount can be primarily bonded to carbon at the defect sites.

Several R-GOC film thicknesses were deposited onto copper and the in-plane thermal conductivity of the entire structure was measured by combining the laser flash technique (LFT) for diffusivity and laser flash calorimetry (LFC) for heat capacity. The thermal conductivity of the R-GOC-copper composite decreases with increasing R-GOC film thickness from the neat copper value (Figure 4.10).To further illuminate the thermal properties of the R-GOC films, the optothermal technique was conducted on the R-GOC film suspended in air. The optothermal technique is a steady state method to determine the thermal conductivity of a material. A laser of known power and beam spot diameter, r_0, is used to create a point source of heat on the suspended film of diameter R and thickness t. We must account for the transmittance of the R-GOC film to light, 72.1% at 514 nm. This

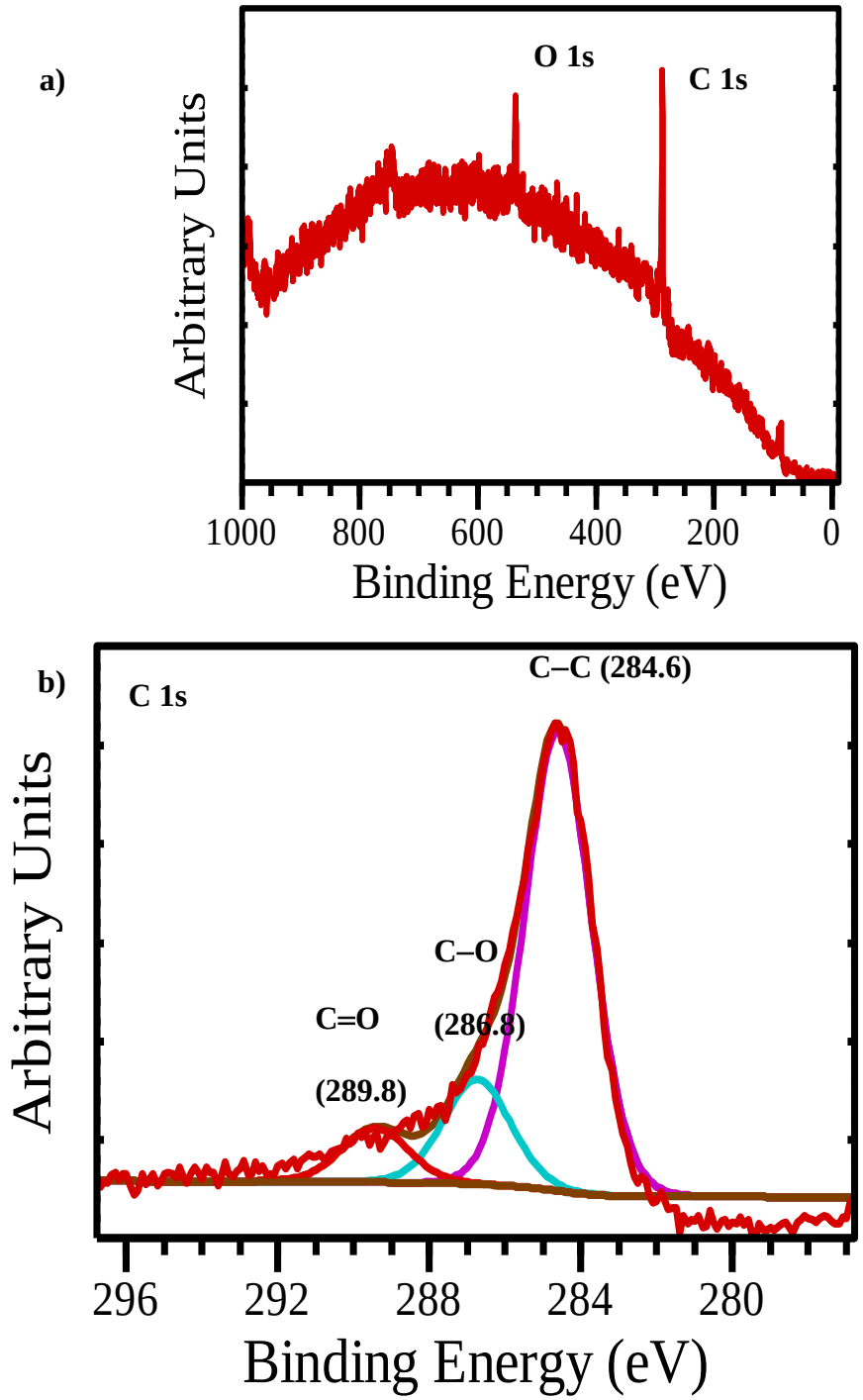


Figure 4.9. XPS survey scan of 10 nm thick R-GOC film (a) indicates the presence of oxygen on the surface of RGOC sample, with higher-resolution C 1s spectra (b) confirming that only small amount of oxygen is bonded to carbon.

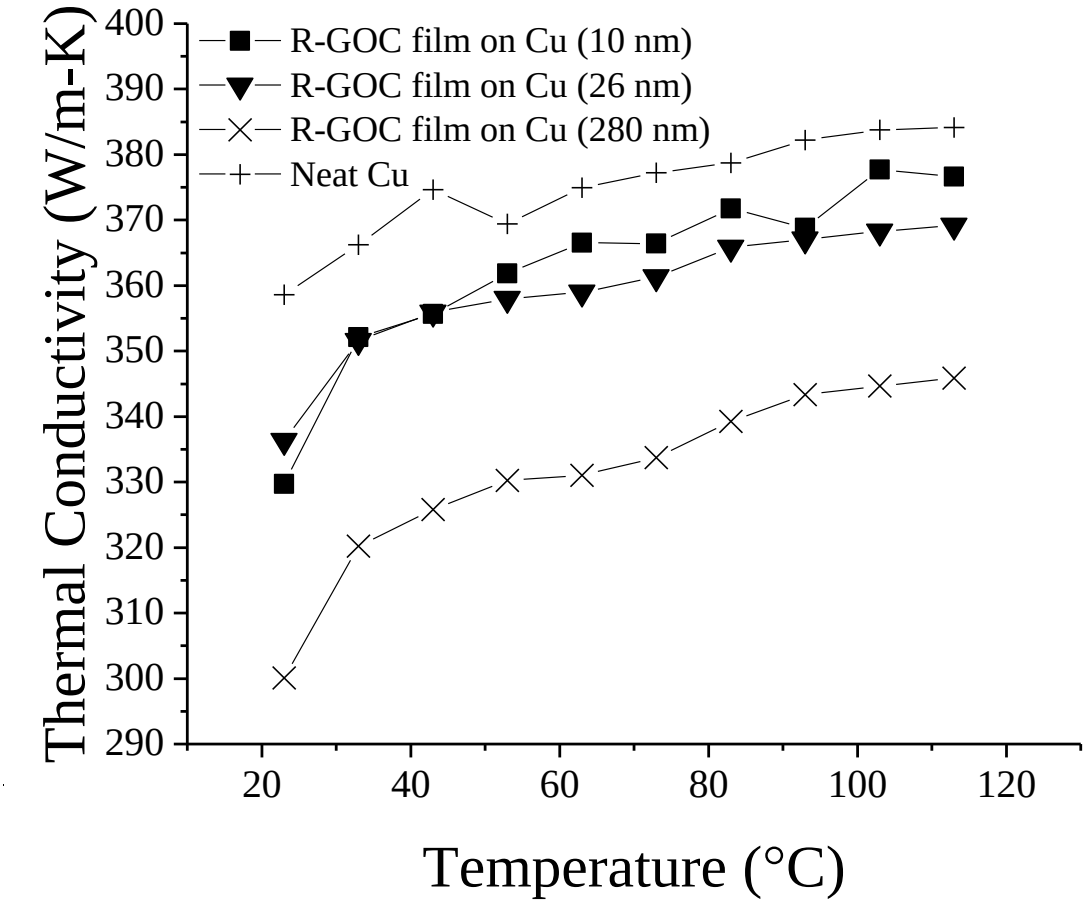


Figure 4.10. In-plane thermal conductivity of R-GOC-Cu composites of varying thickness.

means only ~ 1/5 of the laser power of the 514 nm monochromatic laser incident is absorbed. Because the film size in our case is large (50 μm x 50 μm) compared to the beam spot (0.65 μm diameter) and the film is suspended in air, it is appropriate to apply a uniform 2-dimensional radial heat equation to solve for the thermal conductivity, *K*, according to:

$$K = ln\,(R/r_0)/(2\pi t R_g) \qquad (3)$$

where R_g the thermal resistance is given by:

$$R_g \equiv \frac{T_m - T_0}{Q} \quad (4)$$

where T_m is the temperature measured at the laser spot during laser heating of power Q (after accounting for film transmittance), and T_0 is the initial temperature at ambient with no laser heating.[29] The average Raman G peak shift with temperature, χ_G, of the R-GOC film was measured to be -0.02552 $m^{-1}K^{-1}$. Then the T_m of the R-GOC film at variable Q was calculated from the measured shift in the Raman G peak. Finally, the thermal conductivity is calculated from T_m and measured dimensional parameters. The thermal conductivity was measured to be 91.4 ± 21.7 W/m-K.

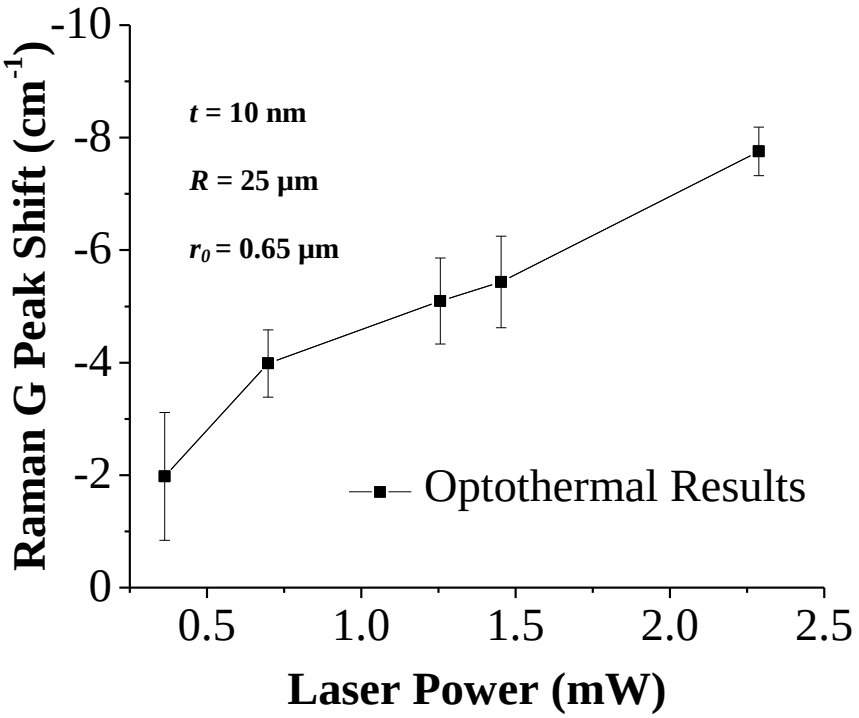


Figure 4.11. Optothermal Raman data for 10 nm thick R-GOC film suspended on Cu TEM grid. The measured G-peak shift with laser power for the R-GOC film suspended on Cu TEM grid.

4.4 Discussion

For practical applications such as transparent conducting films, one desires to maximize the transparency while minimizing the sheet resistance of the film. It was observed that the film has exceptional electrical conductivity and transparency (see Figures 4.4 and 4.5).

Another consideration of application of thermal CVD films as transparent conductors is the scalability. For the purpose of demonstrating the large area growth, the deposition of R-GOC was carried out on 100 mm fused silica wafers (see Figure 4.12). The films have similar properties as the smaller-scale films grown on 1” x 1” substrates (see Figure 4.12)

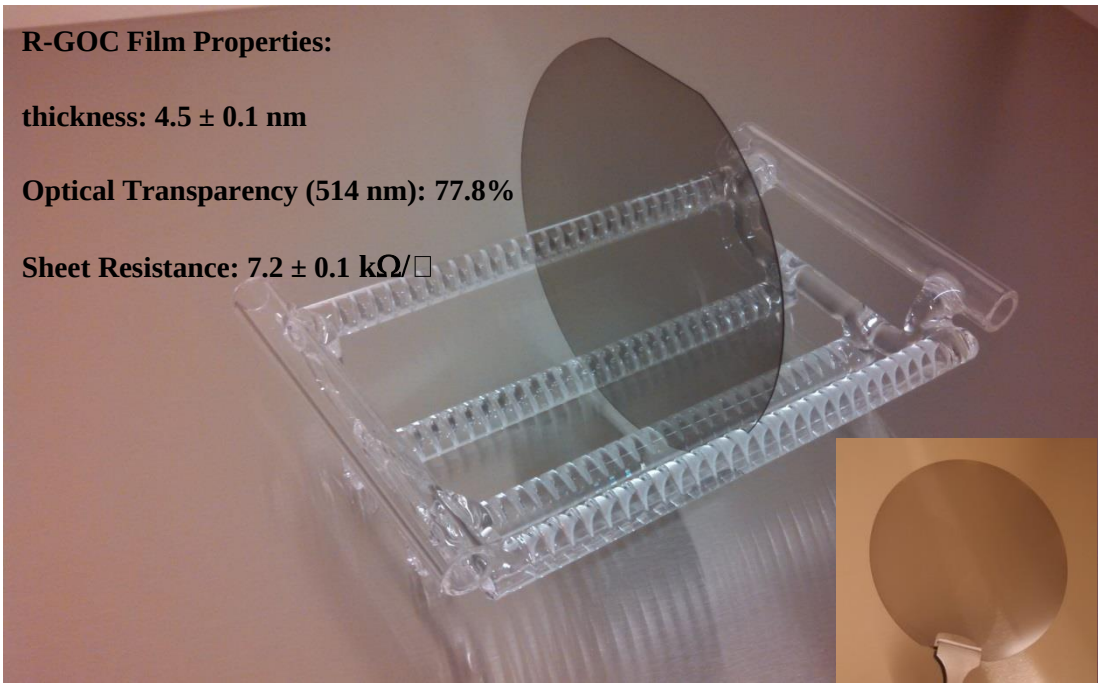


Figure 4.12. Optical images of R-GOC film on 100 mm fused silica wafer.

In consideration of applying a film as a lateral heat spreader, one seeks a film with exceptional thermal conductivity in-plane. The LFT/LFC results indicated the R-GOC films had lower thermal conductivity than copper. The optothermal results elucidate that indeed, the film has excellent thermal conductivity, 91.4 ± 21.7 W/m-K. This thermal conductivity greatly surpasses the literature value for amorphous carbon films, which range from 0.01 to 0.1 W/m-K.[30]

4.5 Conclusions

The thermal CVD process was studied to determine the quality and characteristics of R-GOC films deposited using the copper catalyst or directly onto dielectric substrates. It was observed that the R-GOC film contained 15.5% oxygen content, with sp^3 content increasing with thickness. The carbon films may be deposited on the wafer scale with uniform electrical and optical properties. The thermal characterization indicates that the R-GOC may be of interest for use as a lateral heat spreader, and the electrical and optical transparency results indicate R-GOC may be useful as a transparent conducting film material.

4.6 Acknowledgements

This work was completed at the Center for Nanoscale Materials at Argonne National Laboratory. Use of the Center for Nanoscale Materials was supported by the U.S. Department of Energy, Office of Science, Office of Basic Energy Sciences, under Contract

No. DE-AC02-06CH11357. The XPS characterization was carried out by Dr. Diana Berman at the Center for Nanoscale Materials. The TEM, SAED, and EELS characterization was carried out by Dr. Kenneth Perez at the Center for Nanoscale Materials. The NEXAFS characterization was performed by Dr. Swathi Iyer at Canadian Light Source Inc. The LFT characterization was performed at the Nano-device Laboratory at the University of California, Riverside. The gold substrates for XPS were fabricated and provided by Dr. Daniel Rosenmann from the Center for Nanoscale Materials. We would like to thank Dr. David Gosztola for his time and expertise in the optothermal Raman experimental setup.

REFERENCES AND NOTES

(1) Geim, A. K.; Novoselov, K. S. The Rise of Graphene. *Nat. Mater.* **2007**, *6*, 183–191.

(2) Bolotin, K. I.; Sikes, K. J.; Jiang, Z.; Klima, M.; Fudenberg, G.; Hone, J.; Kim, P.; Stormer, H. L. Ultrahigh Electron Mobility in Suspended Graphene. *Solid State Commun.* **2008**, *146*, 351–355.

(3) Balandin, A. A.; Ghosh, S.; Bao, W.; Calizo, I.; Teweldebrhan, D.; Miao, F.; Lau, C. N. Superior Thermal Conductivity of Single-Layer Graphene. *Nano Lett.* **2008**, *8*, 902–907.

(4) Nair, R. R.; Blake, P.; Grigorenko, A. N.; Novoselov, K. S.; Booth, T. J.; Stauber, T.; Peres, N. M. R.; Geim, A. K. Fine Structure Constant Defines Visual Transparency of Graphene. *Science* **2008**, *320*, 1308.

(5) Lee, S.; Chen, C.; Deshpande, V. V.; Lee, G.-H.; Lee, I.; Lekas, M.; Gondarenko, A.; Yu, Y.-J.; Shepard, K.; Kim, P.; et al. Electrically Integrated SU-8 Clamped Graphene Drum Resonators for Strain Engineering. *Appl. Phys. Lett.* **2013**, *102*, 153101.

(6) Bae, S.; Kim, H.; Lee, Y.; Xu, X.; Park, J.-S.; Zheng, Y.; Balakrishnan, J.; Lei, T.; Kim, H. R.; Song, Y. Il; et al. Roll-to-Roll Production of 30-Inch Graphene Films for Transparent Electrodes. *Nat. Nanotechnol.* **2010**, *5*, 574–578.

(7) Chung, T. F.; Shen, T.; Cao, H.; Jauregui, L. a.; Wu, W.; Yu, Q.; Newell, D.; Chen, Y. P. Synthetic Graphene Grown By Chemical Vapor Deposition on Copper Foils. *Int. J. Mod. Phys. B* **2013**, *27*, 1341002.

(8) Gao, L.; Ren, W.; Xu, H.; Jin, L.; Wang, Z.; Ma, T.; Ma, L.-P.; Zhang, Z.; Fu, Q.; Peng, L.-M.; et al. Repeated Growth and Bubbling Transfer of Graphene with Millimetre-Size Single-Crystal Grains Using Platinum. *Nat. Commun.* **2012**, *3*, 699.

(9) Li, X.; Magnuson, C. W.; Venugopal, A.; Tromp, R. M.; Hannon, J. B.; Vogel, E. M.; Colombo, L.; Ruoff, R. S. Large-Area Graphene Single Crystals Grown by

Low-Pressure Chemical Vapor Deposition of Methane on Copper. *J. Am. Chem. Soc.* **2011**, *133*, 2816–2819.

(10) Chu, J. H.; Kwak, J.; Kim, S.-D.; Lee, M. J.; Kim, J. J.; Park, S.-D.; Choi, J.-K.; Ryu, G. H.; Park, K.; Kim, S. Y.; et al. Monolithic Graphene Oxide Sheets with Controllable Composition. *Nat. Commun.* **2014**, *5*, 3383.

(11) Liu, Y.; Dong, X.; Chen, P. Biological and Chemical Sensors Based on Graphene Materials. *Chem. Soc. Rev.* **2012**, *41*, 2283–2307.

(12) Marcano, D. C.; Kosynkin, D. V; Berlin, J. M.; Sinitskii, A.; Sun, Z.; Slesarev, A.; Alemany, L. B.; Lu, W.; Tour, J. M. Improved Synthesis of Graphene Oxide. *ACS Nano* **2010**, *4*, 4806–4814.

(13) Lipatov, A.; Varezhnikov, A.; Wilson, P.; Sysoev, V.; Kolmakov, A.; Sinitskii, A. Highly Selective Gas Sensor Arrays Based on Thermally Reduced Graphene Oxide. *Nanoscale* **2013**, *5*, 5426–5434.

(14) Schwamb, T.; Burg, B. R.; Schirmer, N. C.; Poulikakos, D. An Electrical Method for the Measurement of the Thermal and Electrical Conductivity of Reduced Graphene Oxide Nanostructures. *Nanotechnology* **2009**, *20*, 405704.

(15) Stankovich, S.; Dikin, D. A.; Piner, R. D.; Kohlhaas, K. A.; Kleinhammes, A.; Jia, Y.; Wu, Y.; Nguyen, S. T.; Ruoff, R. S. Synthesis of Graphene-Based Nanosheets via Chemical Reduction of Exfoliated Graphite Oxide. *Carbon N. Y.* **2007**, *45*, 1558–1565.

(16) Huang, J.; Larisika, M.; Fam, W. H. D.; He, Q.; Nimmo, M. A.; Nowak, C.; Tok, I. Y. A. The Extended Growth of Graphene Oxide Flakes Using Ethanol CVD. *Nanoscale* **2013**, *5*, 2945–2951.

(17) Sagar, R. U. R.; Zhang, X.; Xiong, C.; Yu, Y. Semiconducting Amorphous Carbon Thin Films for Transparent Conducting Electrodes. *Carbon N. Y.* **2014**, *76*, 64–70.

(18) Göbel, A.; Hemberger, F.; Vidi, S.; Ebert, H. P. A New Method for the Determination of the Specific Heat Capacity Using Laser-Flash Calorimetry Down to 77K. *Int. J. Thermophys.* **2012**, *34*, 883–893.

(19) Ghosh, S.; Teweldebrhan, D.; Morales, J. R.; Garay, J. E.; Balandin, A. A. Thermal Properties of the Optically Transparent Pore-Free Nanostructured Yttria-Stabilized Zirconia. *J. Appl. Phys.* **2009**, *106*, 113507.

(20) Yan, Z.; Liu, G.; Khan, J. M.; Balandin, A. a. Graphene Quilts for Thermal Management of High-Power GaN Transistors. *Nat. Commun.* **2012**, *3*, 827.

(21) Goli, P.; Ning, H.; Li, X.; Lu, C. Y.; Novoselov, K. S.; Balandin, A. A. Thermal Properties of Graphene-Copper-Graphene Heterogeneous Films. *Nano Lett.* **2014**, *14*, 1497–1503.

(22) Watts, B.; Thomsen, L.; Dastoor, P. C. Methods in Carbon K-Edge NEXAFS: Experiment and Analysis. *J. Electron Spectros. Relat. Phenomena* **2006**, *151*, 105–120.

(23) Hao, L.; Diao, X.; Xu, H.; Gu, B.; Wang, T. Thickness Dependence of Structural, Electrical and Optical Properties of Indium Tin Oxide (ITO) Films Deposited on PET Substrates. *Appl. Surf. Sci.* **2008**, *254*, 3504–3508.

(24) Malard, L. M.; Pimenta, M. a.; Dresselhaus, G.; Dresselhaus, M. S. Raman Spectroscopy in Graphene. *Phys. Rep.* **2009**, *473*, 51–87.

(25) Wong, C. H. A.; Ambrosi, A.; Pumera, M. Thermally Reduced Graphenes Exhibiting a Close Relationship to Amorphous Carbon. *Nanoscale* **2012**, *4*, 4972–4977.

(26) Huang, J.; Larisika, M.; Fam, W. H. D.; He, Q.; Nimmo, M. a; Nowak, C.; Tok, I. Y. A. The Extended Growth of Graphene Oxide Flakes Using Ethanol CVD. *Nanoscale* **2013**, *5*, 2945–2951.

(27) Hamon, A.-L.; Verbeeck, J.; Schryvers, D.; Benedikt, J.; M. C. M. v. d. Sanden, R. ELNES Study of Carbon K-Edge Spectra of Plasma Deposited Carbon Films. *J. Mater. Chem.* **2004**, *14*, 2030.

(28) Pacilé, D.; Meyer, J. C.; Fraile Rodríguez, A.; Papagno, M.; Gómez-Navarro, C.; Sundaram, R. S.; Burghard, M.; Kern, K.; Carbone, C.; Kaiser, U. Electronic Properties and Atomic Structure of Graphene Oxide Membranes. *Carbon N. Y.* **2011**, *49*, 966–972.

(29) Cai, W.; Moore, A. L.; Zhu, Y.; Li, X.; Chen, S.; Shi, L.; Ruoff, R. S. Thermal Transport in Suspended and Supported Monolayer Graphene Grown by Chemical Vapor Deposition. *Nano Lett.* **2010**, *10*, 1645–1651.

(30) Balandin, A. A. Thermal Properties of Graphene and Nanostructured Carbon Materials. *Nat. Mater.* **2011**, *10*, 569–581.

Chapter 5. Engineering of CVD Graphene to Achieve All 2D Flexible, Transparent, and Thinnest Thin Film Transistor

5.0 Abstract

In this chapter, the fabrication of 10 atomic layer thick, high mobility, transparent thin film transistors (TFTs) is demonstrated on conventional silicon and flexible substrates. Single layer graphene was used as the electrode material, multilayer h-BN as the gate dielectric, and bilayers of WSe_2 were used as the semiconducting channel material for the TFTs. The field effect carrier mobility was 45 $cm^2/(V\text{-}s)$, which exceeds the mobility values of state of the art amorphous silicon based TFTs by a factor of two. The transparency of the device film stack of WSe_2—h-BN—graphene was found to be more than 88% transparent over the entire visible light spectrum. The device characteristics were stable and unaltered for in-plane mechanical strain of up to 2% and over a wide temperature range (77-400K). The fabricated TFTs were observed to have subthreshold slope of 90 mV/decade, current ON-OFF ratio of 10^7 with ambipolar conduction. These electrical characteristics are highly sought after though rarely reported in organic and inorganic TFT studies.

5.1 Introduction

Nanostructured carbon thin films, such as graphene, possess superior electrical,[1] thermal,[2] optical,[3] and mechanical properties.[4] High carrier velocity, exceptional mechanical stability, and near complete transparency of graphene has resulted in its commercialization as stretchable and transparent electrodes and interconnects.[5–8] Graphene has been investigated as an alternative to silicon for post CMOS nanoelectronics, but because it has no sizeable bandgap, graphene cannot be used in logic circuits the way silicon can. However, transition metal dichalgenides (TMDs) such as MoS_2, and WSe_2 are semiconducting 2D materials with effective bandgaps and electron mobility for high performance field effect transistors (FETs).[9–14] In terms of insulating materials, hexagonal boron nitride (h-BN) provides a compatible interface to both TMDs and graphene while being a large bandgap insulator. These three elements, the high-mobility transparent conducting graphene, the high-mobility semiconducting TMDs, and the insulating h-BN, are 2D materials that may potentially be stacked to form thin film transistors (TFTs). Thus far, the TFT industry has been focused on amorphous silicon (a-Si) due to limited materials choices. The key features in developing a superior TFT include high electron and hole mobility, high On-OFF current ratio (which corresponds to a low subthreshold slope (in mV/decade)), low contact resistance, ambipolar conduction, high optical transparency, temperature

stability, and mechanical flexibility.[15] In addition to meeting these requirements, 2D materials also operate at lower power, improving scalability. In this chapter the fabrication of the thinnest all-2D, flexible, transparent TFT is described, including characterization of the electrical properties and light transmittance of the devices.

5.2 Experimental Methods

Copper foil (Alfa Aesar 25 μm, 99.8%) is cut into rectangular pieces about the same area as the 3 cm x 5 cm quartz block used as a sample chuck in the chemical vapor deposition (CVD) tube. The CVD process includes annealing in hydrogen to remove any oxide film that may have formed on the Cu foil, followed by deposition of carbon at high temperature using methane as the precursor gas, and then cooling to ambient temperature in vacuum to form polycrystalline graphene. This process is based on the success of the methods developed by Li et al for Cu foils.[16] The copper foil is annealed in 1000 sccm hydrogen at 800 °C for 30 min and 300 Torr chamber pressure prior to the growth. The temperature is increased to 1000 °C, the chamber is purged to 0.1 Torr pressure, and methane is flowed at 50 sccm and 1 Torr chamber pressure for 3 min. The chamber is set to cool to ambient in vacuum pressure (0.01 Torr). Once the temperature reaches ≤100 °C, the samples are removed from the chamber using nitrogen as a purging gas. The graphene coats both sides of the Cu foil. Reactive ion etching (RIE) in oxygen plasma is used to remove the backside graphene from the Cu foil. For bilayer graphene, the chamber is cooled to ambient in a 1:1

mixture of hydrogen and argon at 1000 sccm each, until the chamber pressure reaches 300 Torr, then the argon flow is ceased.

WSe_2 flakes are mechanically exfoliated onto 20 nm SiO_2/Si substrate and on flexible polyethylene terephthalate substrate using scotch tape. The CVD-grown graphene films are transferred over the entire substrates using polymethyl methacrylate (PMMA) as a transfer handle and ferric chloride acid as the Cu etchant. Care must be taken to rinse the PMMA film several times in fresh deionized water to remove all of the ferric chloride etchant residues. The PMMA is removed using dichloroethane and acetone. Source and drain Al electrode pads are patterned using e-beam lithography and liftoff. Oxygen plasma RIE etches the graphene that lies over the channel region of the WSe_2 flake, the Al masks the contact and electrode graphene. Further e-beam lithography is used with sodium hydroxide solution to selectively etch the Al from the graphene contacts. Multilayer h-BN was acquired from graphene-supermarket.com on Cu foil, and using PMMA as the transfer handle and ferric chloride acid, the h-BN films are transferred over the entire substrates. Topgate Al electrode pads and contacts are patterned using e-beam lithography and liftoff. Oxygen plasma RIE is used to etch the graphene. Again, the Al masks the topgate electrode contact graphene. Further e-beam lithography is used with sodium hydroxide solution to selectively etch the Al from the graphene contact to the topgate h-BN.

Visible spectroscopy was used to measure the visible transparency of the WSe_2 flakes exfoliated onto PET, as well as the fabricated WSe_2—h-BN—graphene active device layer on PET with blank PET as the reference.

5.3 Results of the Experiments

Figure 5.1a shows the false color SEM images of the back-gated all 2D TFT on SiO_2. Figure 5.1b,c show the three dimensional diagram and cross-section view of the 2D TFT device. Figure 5.2 shows the back-gated transfer characteristics of an all 2D TFT with bilayer WSe_2 flake as the semiconducting channel material and the graphene as the source/drain contact electrodes. Figure 5.3 shows the transfer characteristics of a graphene field effect transistor (GFET) with underlying WSe_2 as the screening layer. The Fermi level of the of the graphene responds to the back gate bias in spite of the charge screening by the WSe_2 channel underneath the contacts. This suggests in the back-gating configuration the WSe_2 acts just as an additional dielectric layer. The observed ambipolar conduction of the fabricated TFT suggests that the Dirac point of graphene aligns close to the middle of the bandgap of the semiconducting WSe_2 layer (Fig. 5.4a). Because the bandgap of bilayer WSe_2 is ~1.3eV, this would indicate the presence of a large Schottky barrier height (Φ) at the graphene WSe_2 contacts for both electron injection (Φ_{N0}) into the conduction band and hole injection (Φ_{P0}) into the valence band, shown in the band diagram in Fig. 5.4. However, when a negative gate

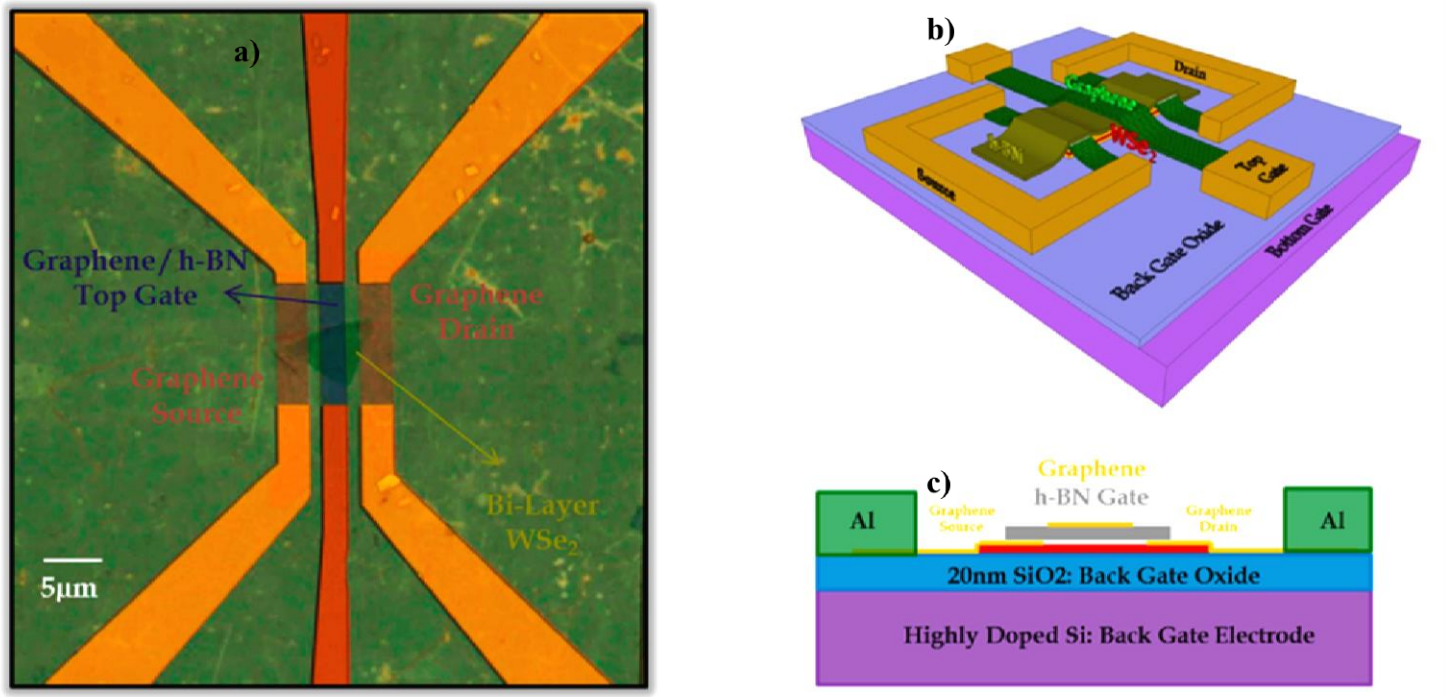


Figure 5.1. (a) False color SEM image (b) 3D cartoon, and (c) cross sectional view of an all 2D TFT with graphene as metal electrode, h-BN as gate dielectric and WSe2 as the semiconducting channel material.

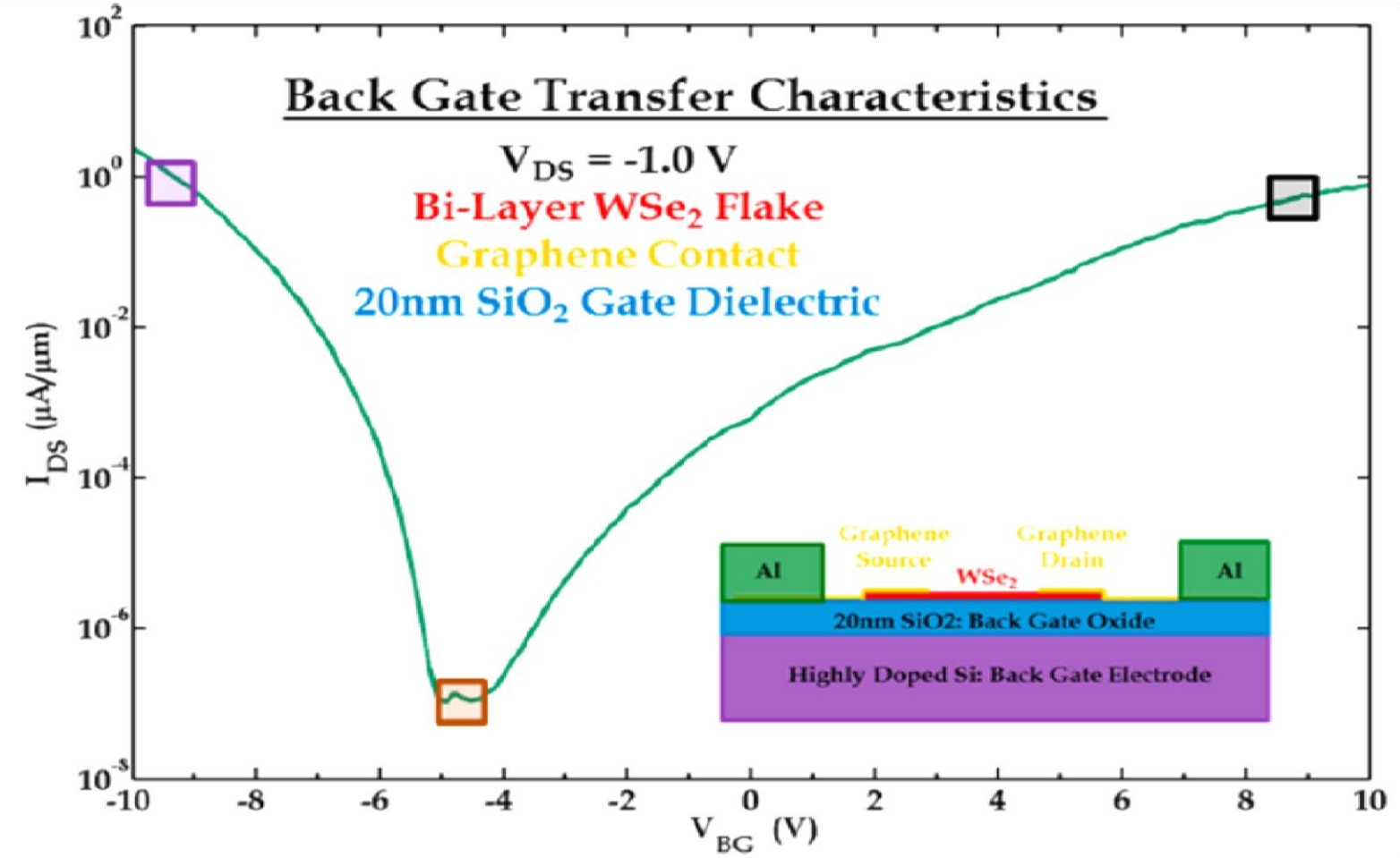


Figure 5.2. Back gate transfer characteristics of a WSe_2 TFT with graphene contact electrodes at the source and drain. Inset is the cross section diagram of the device.

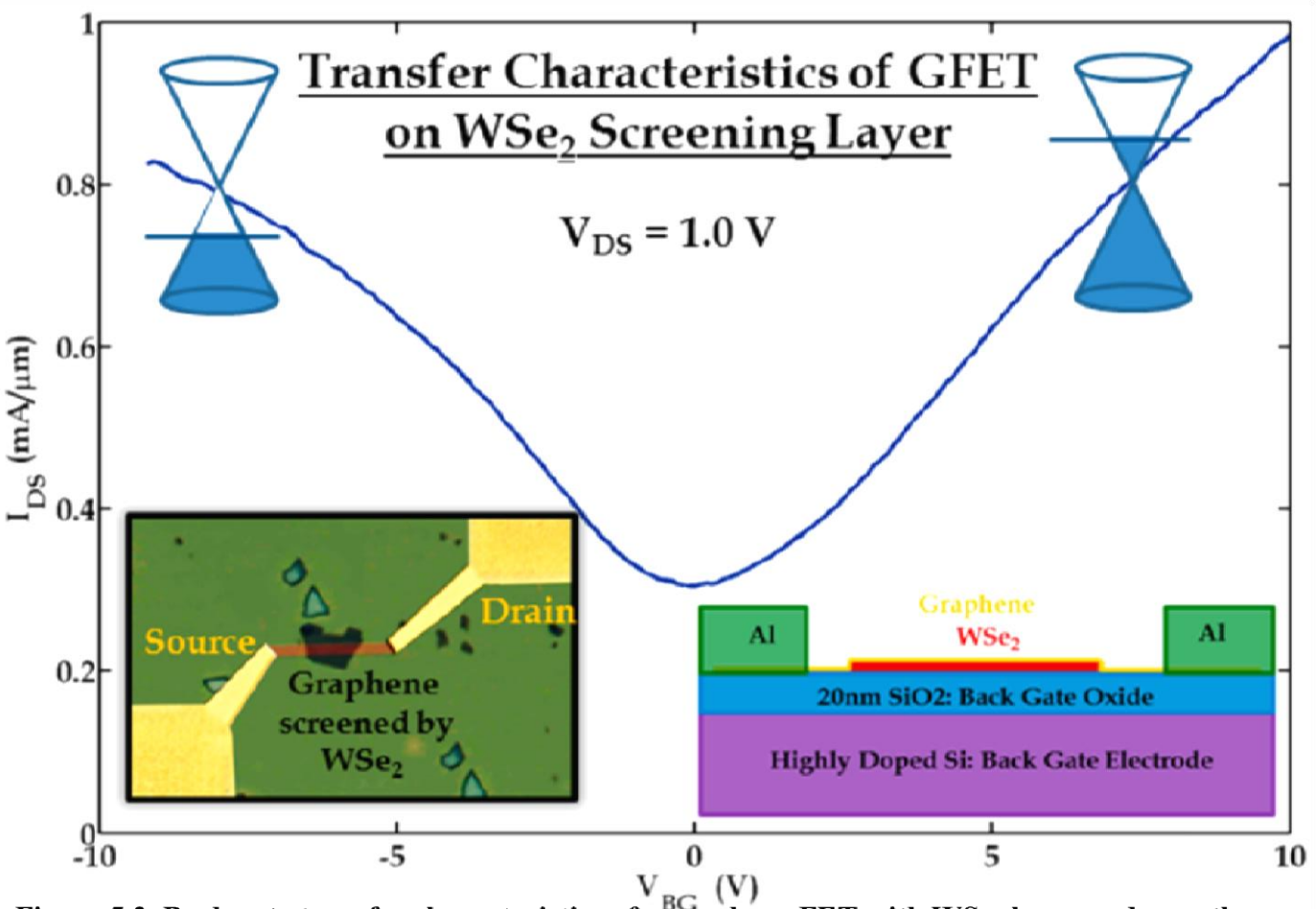


Figure 5.3. Back gate transfer characteristics of a graphene FET with WSe_2 layer underneath. Inset shows colorized SEM image of the device and cross section diagram of the device.

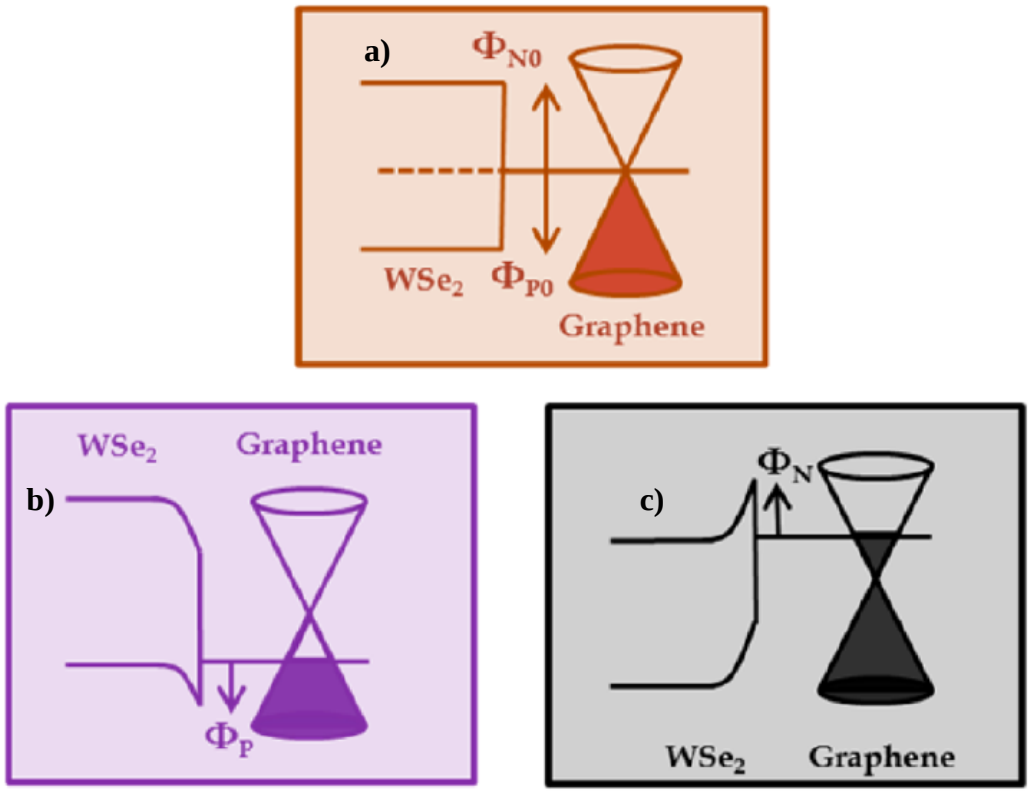


Figure 5.4. Band alignment at graphene to WSe_2 contact interface with no back gate (a), negative back gate bias (b), and positive back gate bias (c).

bias is applied, the energy bands in WSe_2 bend to facilitate hole injection into the valence band while simultaneously the Fermi level in graphene moves closer to the valence band, reducing the Schottky barrier height for hole injection from Φ_{P0} to Φ_P (Fig. 5.4b). A similar effect occurs for positive bias, reducing the Schottky barrier height for electron injection to the conduction band from Φ_{N0} to Φ_N (See Fig. 5.4c). The reduced Schottky barrier height corresponds with a lower contact resistance than would otherwise be the case with non-graphene contacts. Figure 43a,b shows the partially top-gated transfer characteristics of the same TFT with h-BN as the gate dielectric and

graphene as the gate electrode corresponding to positive (V_{BG} =10 V) and negative (V_{BG} = -10V) back gate biases. The negative bias causes p-doping and the device exhibits p-FET characteristics, whereas the positive bias causes n-doping and n-FET characteristics.

The subthreshold slope was found to be 90mV/decade in the p-FET configuration

and 130mV/decade for n-FET configuration (see Fig. 5.5).

The mobility of the devices were extracted at low V_{DS} = 0.1 V, using the transconductance equation:

$$g_m=\mu C_{OX}(W/L)V_{DS} \qquad (5.1)$$

which relates the transconductance, g_m, to the field effect mobility, μ, where W and L are the channel width and the channel length, respectively; and $C_{OX} = \varepsilon_{OX}/d_{OX}$, where ε_{OX} is the dielectric constant, and d_{OX} is the thickness of the gate oxide. Assuming d_{OX} = 3 nm for h-BN, ε_{OX} = 6 x 10-11, C_{OX} is 3.1 x 10^{-2} F/m^2. From the transfer characteristics and eq 5.1, the average effective field-effect mobility values for electrons and holes were found to be 24 and 45 $cm^{2/}$V-s respectively.

The results of the transfer and output characteristics of the TFT devices fabricated on flexible poly ethylene terephthalate (PET) substrates (see optical image in Fig. 5.6) are given in Fig. 5.7 and 5.8 respectively, and the transfer characteristics with applied strain

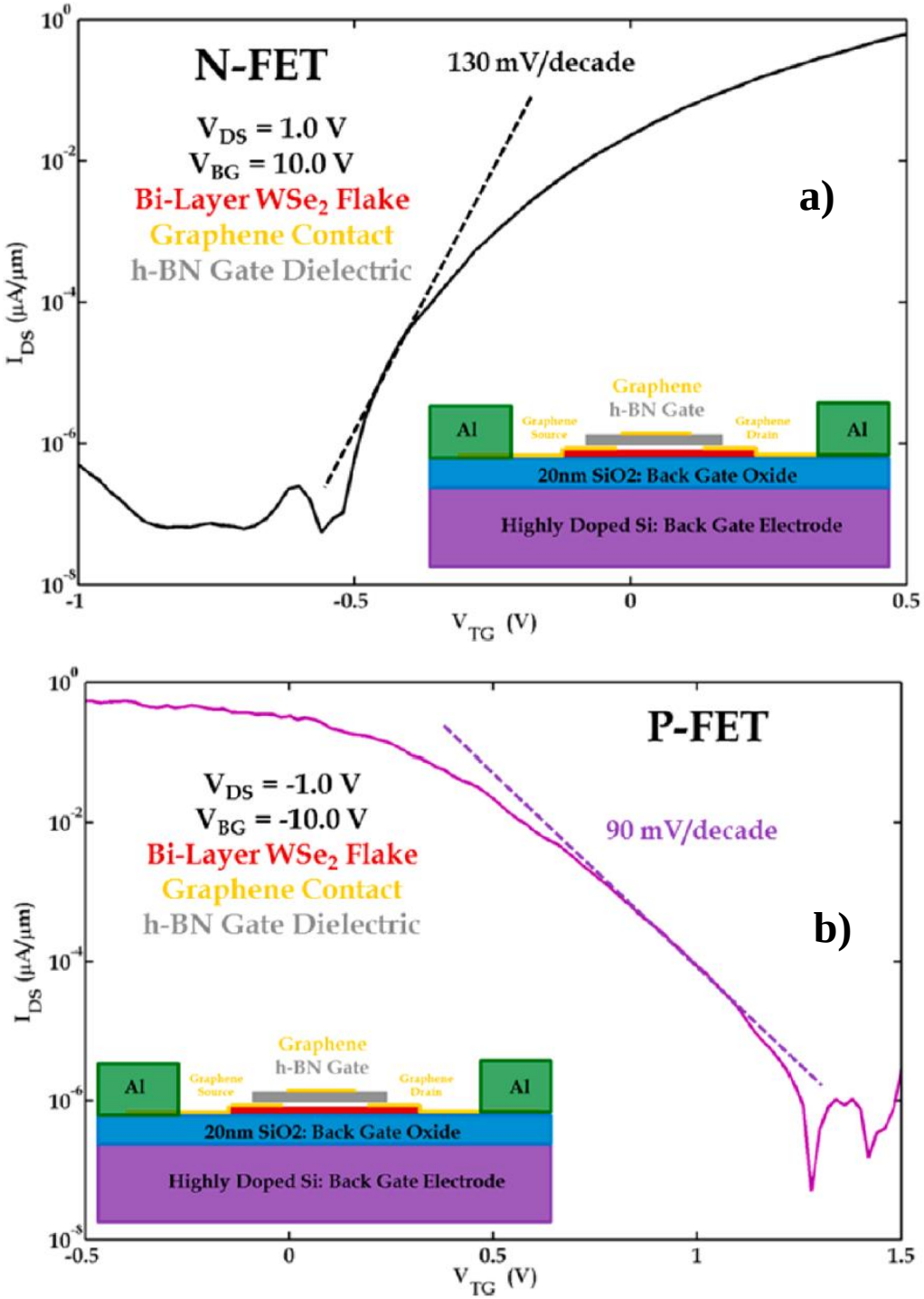
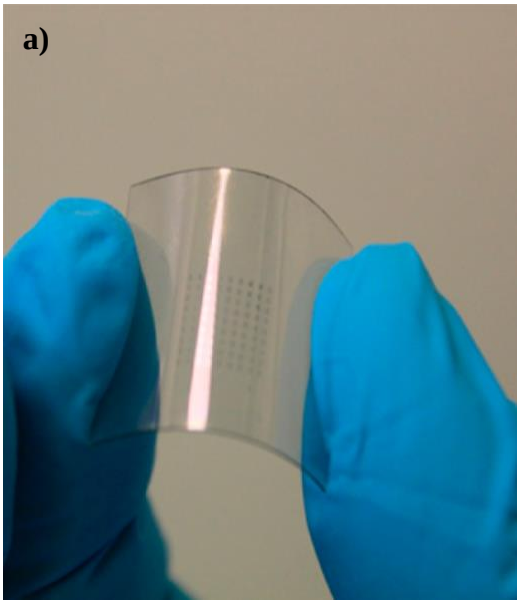


Figure 5.5. Top gate transfer characteristics of all 2D TFT corresponding to V_{BG} = 10 V (a), and -10 V (b).



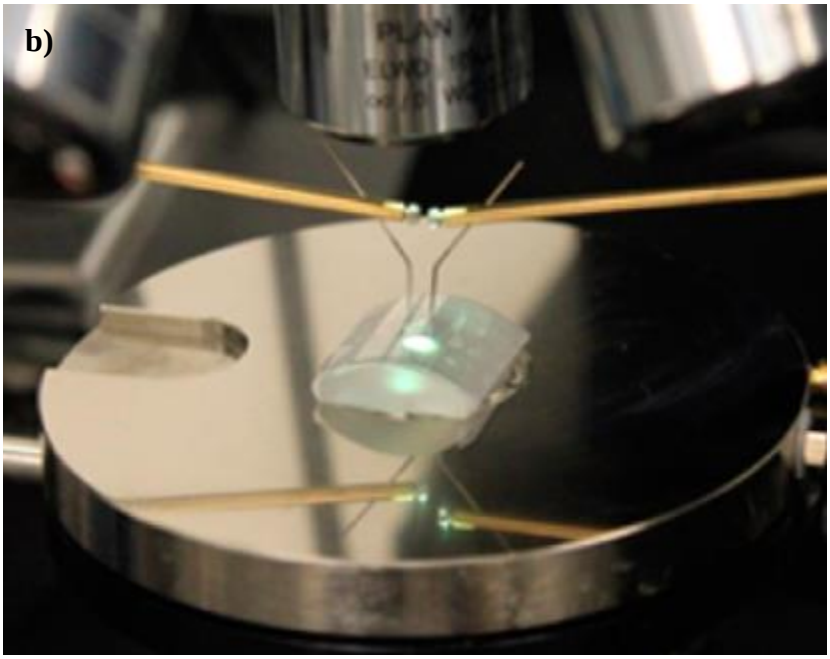


Figure 5.6. Optical images of thinnest FET on flexible PET substrate (a) and experimental setup to measure strain effect (b).

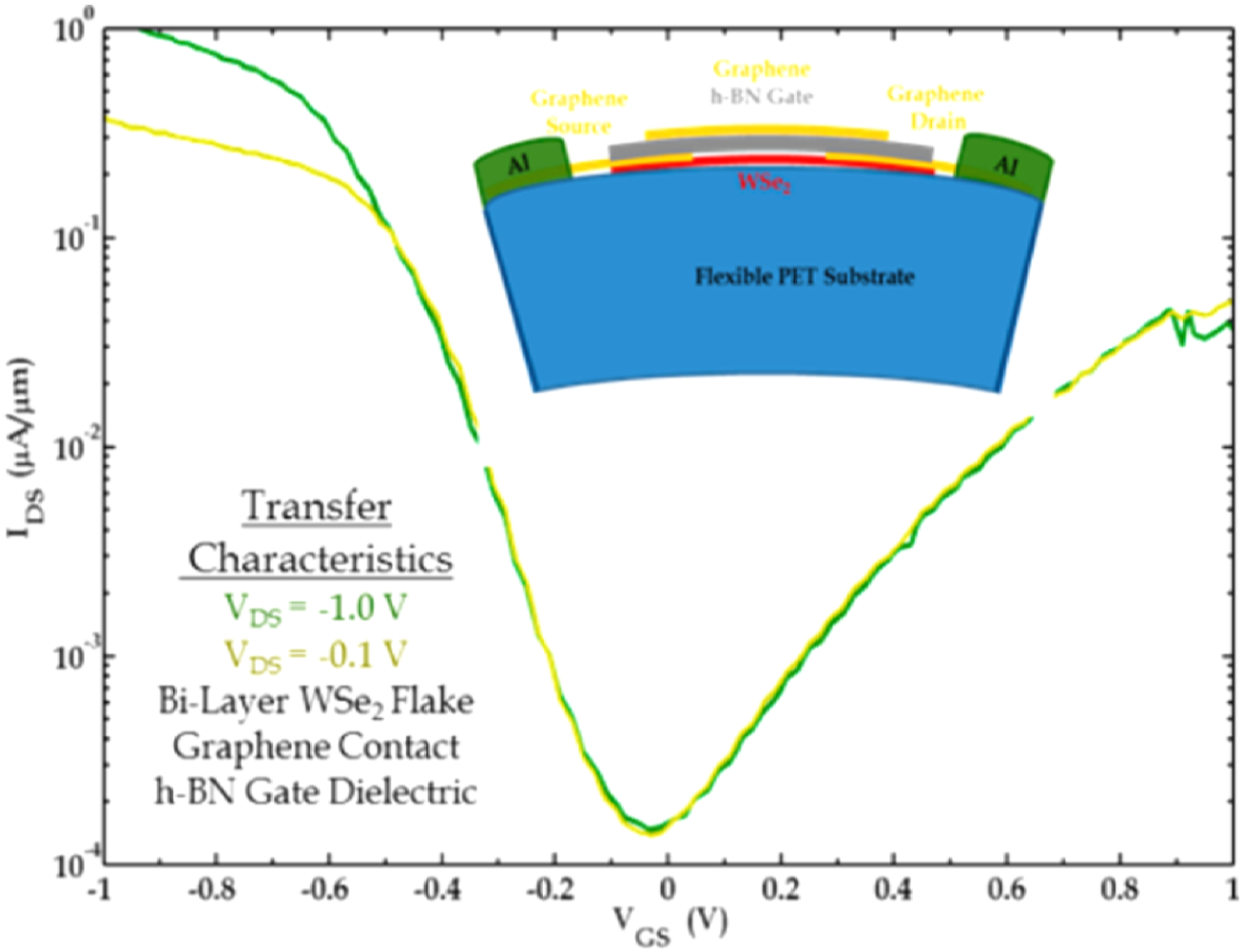


Figure 5.7. Transfer characteristics of the thinnest FET on flexible PET substrate.

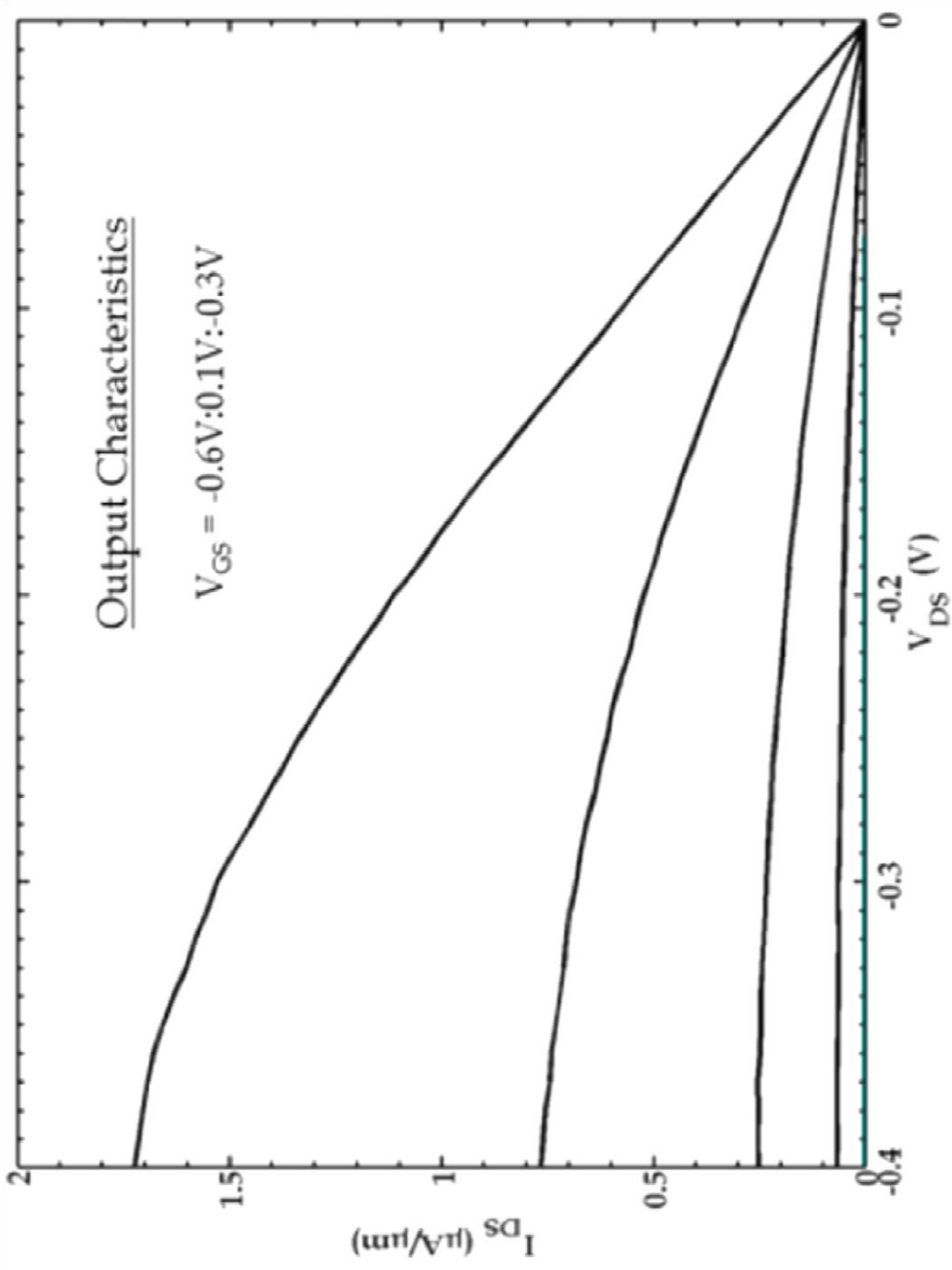


Figure 5.8.Output characteristics of the thinnest FET on flexible PET substrate.

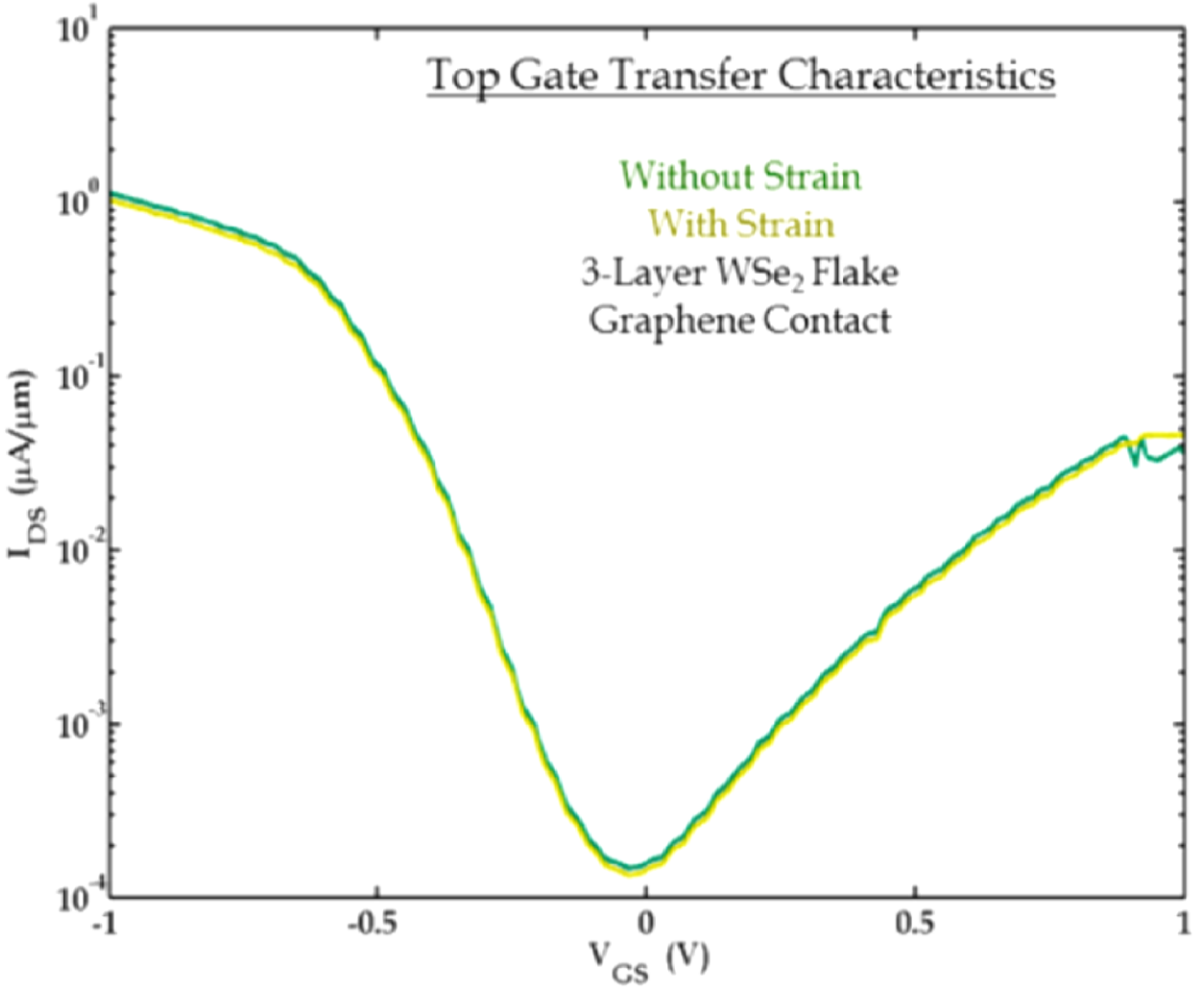


Figure 5.9. Transfer characteristics of the thinnest FET on flexible PET substrate with and without strain.

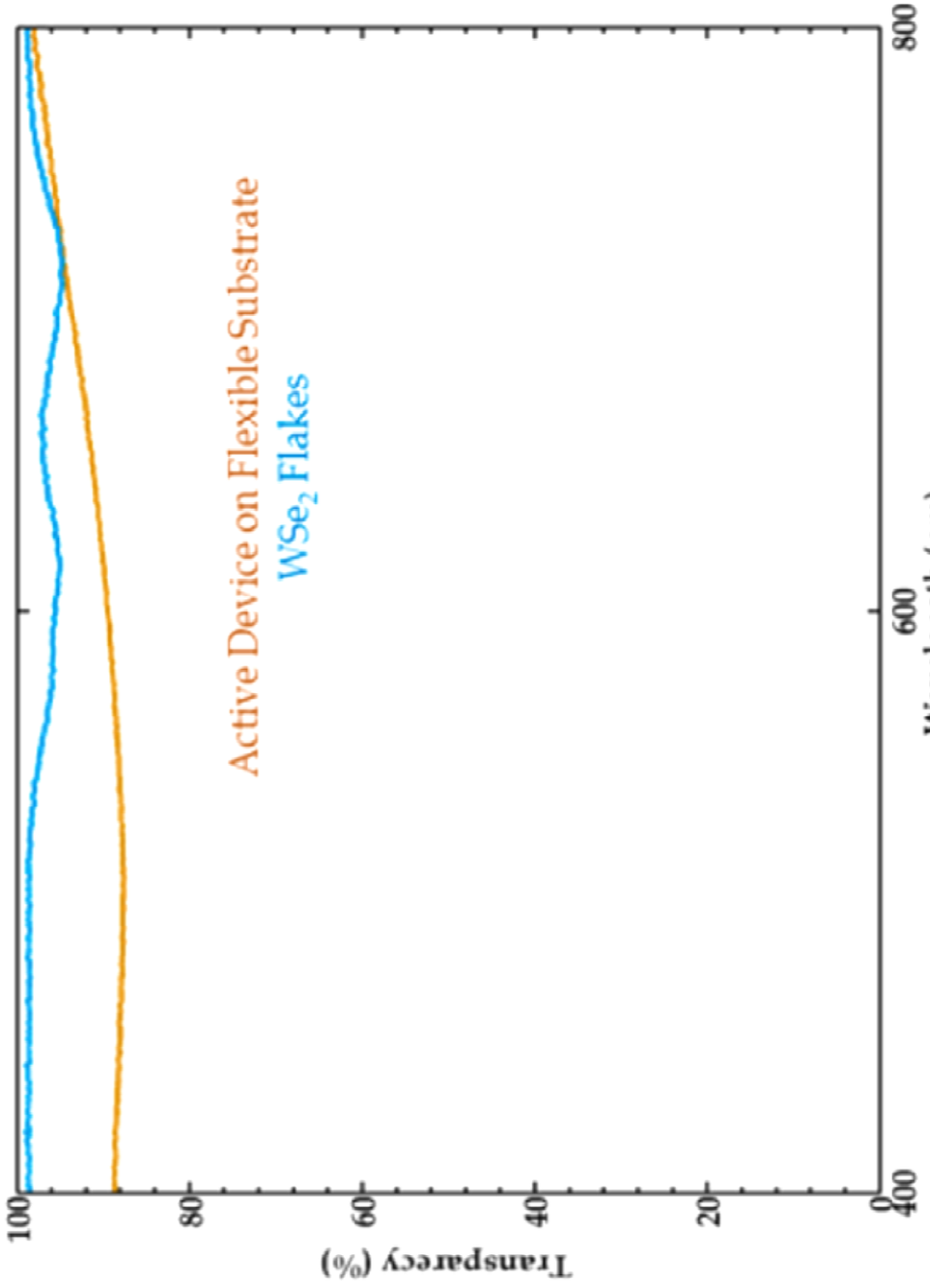


Figure 5.10. Transparency of WSe_2 flakes, and thinnest FET on flexible PET substrate in the visible light range.

are given in Fig. 5.9. The optical transmittance of the device stack and exfoliated WSe_2 flakes is given in Fig. 5.10.

The subthreshold slope of the TFT on flexible PET substrate was found to be ~180 mV/ decade for hole p-FET configuration and ~340 mV/decade for the n-FET configuration. The devices were measured with and without strain, and as seen in Fig. 5.9, the device characteristics were unaltered even with 2% in-plane mechanical strain. Due to the possibility that the 2D materials have weak adhesion to the substrates, it is difficult to confirm the invariability of the electronic properties with applied strain.

The transmittance of visible light for the all 2D TFT was found to be ~88%, the absorbance of the WSe_2 flakes was less than 5% (See Fig. 48).

5.4 Discussion

The mobility of most organic semiconductors is < 1 $cm^{2/}V$-s.[15,17] The mobility value of the fabricated TFT device outperforms state of the art TFT technology by ~100 times. Alternative active transparent semiconducting materials such as metal oxides like indium tin oxide , ZnO, and alloys of zinc and tin oxides have demonstrated high mobility values (1-100 $cm^{2/}V$-s), but they suffer severe threshold voltage shift and electrical instability due to oxygen vacancy doping.[15,18,19] The all 2-D TFTs described here show no threshold voltage shift when exposed to vacuum or ambient air conditions, even after extended time. Carbon Nanotube and nanowire based TFTs have

demonstrated mobility values in the range of 10-100 $cm^{2/}V$-s, however wire placement remains a challenge in the realization of reliable and consistent properties in these devices. [20,21] The CVD graphene growth process eliminates the placement problem, while potentially lowering the contact resistance by band bending and effectively reducing the Schottky barrier to hole injection into the valence band or electron injection into the conduction band.

For the development of thin film display technology (light emitting diode (LED) or liquid crystal (LCD) displays), the available drive current (I_D) of the TFT is an important parameter. The required drive current depends on the material and brightness desired. For example, a single pixel of organic LED requires several μA of current. This drive current is readily achieved in the 2D TFTs described here at drive voltages as low as $V_{DS} = V_{GS} = 1V$. The number of pixels/area possible with the described TFT design could be aggressively scaled down, and a single TFT could drive multiple LEDs.

The drive current is important for LCDs as well as shown in eq 5.2. The charging time, τ, is inversely proportional to the drive current.

$$\tau = V_D C_P / I_D \qquad (5.2)$$

where V_D is the drive voltage, and C_P is the pixel capacitance. For a standard C_p = 0.1-1pF, the all 2D TFTs described here will have a charging time of 0.1-1μs. The

resolution of an LCD, as given by eq 5.3:

$$\beta = V_D C_{PS}/C_P \quad (5.3)$$

where C_{PS} is the parasitic capacitance, can also be significantly improved by using the all 2D TFT described here. For a standard C_{PS} = 50 fF, resolution of 5-50 mV may be achieved. A figure of merit, ζ as high as 10^8-10^{10} may be achieved in the 2D TFTs, as given by eq 5.4:

$$\zeta = \tau^{-1}\beta^{-1} \quad (5.4)$$

The figure of merit obtained is 2-4 orders of magnitude higher than the state of the art a-Si TFTs.

5.5 Conclusions

In this chapter, the fabrication of the thinnest, flexible, transparent, high performance TFT was demonstrated using all two-dimensional layered materials. The fabricated all 2D TFT outperforms the state of the art a-Si TFT in mobility, drive current capability, and charging time. The presence of ambipolar conduction is another unique feature for the fabricated all 2D TFTs. This chapter highlights the potential of CVD graphene as an important part of achieving the future of TFT technology.

5.6 Acknowledgments

Reprinted (adapted) with permission from (Das S, Gulotty R, Sumant A V, Roelofs A. All

two-dimensional, flexible, transparent, and thinnest thin film transistor. Nano Lett **2014**;14:2861–6.). Copyright (2014) American Chemical Society." This work was performed at the Center for Nanoscale Materials at Argonne National Laboratory. Use of the Center for Nanoscale Materials was supported by the U.S. Department of Energy, Office of Science, Office of Basic Energy Sciences, under Contract No. DE-AC02-06CH11357.

REFERENCES AND NOTES

(1) Bolotin, K. I.; Sikes, K. J.; Jiang, Z.; Klima, M.; Fudenberg, G.; Hone, J.; Kim, P.; Stormer, H. L. Ultrahigh Electron Mobility in Suspended Graphene. *Solid State Commun.* **2008**, *146*, 351–355.

(2) Balandin, A. A.; Ghosh, S.; Bao, W.; Calizo, I.; Teweldebrhan, D.; Miao, F.; Lau, C. N. Superior Thermal Conductivity of Single-Layer Graphene. *Nano Lett.* **2008**, *8*, 902–907.

(3) Nair, R. R.; Blake, P.; Grigorenko, A. N.; Novoselov, K. S.; Booth, T. J.; Stauber, T.; Peres, N. M. R.; Geim, A. K. Fine Structure Constant Defines Visual Transparency of Graphene. *Science* **2008**, *320*, 1308.

(4) Lee, S.; Chen, C.; Deshpande, V. V.; Lee, G.-H.; Lee, I.; Lekas, M.; Gondarenko, A.; Yu, Y.-J.; Shepard, K.; Kim, P.; et al. Electrically Integrated SU-8 Clamped Graphene Drum Resonators for Strain Engineering. *Appl. Phys. Lett.* **2013**, *102*, 153101.

(5) Palacios, T. Graphene Electronics: Thinking Outside the Silicon Box. *Nat. Nanotechnol.* **2011**, *6*, 464–465.

(6) Geim, A. K.; Novoselov, K. S. The Rise of Graphene. *Nat. Mater.* **2007**, *6*, 183–191.

(7) Bae, S.; Kim, H.; Lee, Y.; Xu, X.; Park, J.-S.; Zheng, Y.; Balakrishnan, J.; Lei, T.; Kim, H. R.; Song, Y. Il; et al. Roll-to-Roll Production of 30-Inch Graphene Films for Transparent Electrodes. *Nat. Nanotechnol.* **2010**, *5*, 574–578.

(8) Chen, X.; Akinwande, D.; Lee, K.-J.; Close, G. F.; Yasuda, S.; Paul, B. C.; Fujita, S.; Kong, J.; Wong, H.-S. P. Fully Integrated Graphene and Carbon Nanotube Interconnects for Gigahertz High-Speed CMOS Electronics. *IEEE Trans. Electron Devices* **2010**, *57*, 3137–3143.

(9) Radisavljevic, B.; Radenovic, A.; Brivio, J.; Giacometti, V.; Kis, A. Single-Layer MoS2 Transistors. *Nat. Nanotechnol.* **2011**, *6*, 147–150.

(10) Das, S.; Chen, H.-Y.; Penumatcha, A. V.; Appenzeller, J. High Performance Multilayer MoS2 Transistors with Scandium Contacts. *Nano Lett.* **2013**, *13*, 100–105.

(11) Wang, H.; Yu, L.; Lee, Y.-H.; Shi, Y.; Hsu, A.; Chin, M. L.; Li, L.-J.; Dubey, M.; Kong, J.; Palacios, T. Integrated Circuits Based on Bilayer MoS_2 Transistors. *Nano Lett.* **2012**, *12*, 4674–4680.

(12) Podzorov, V.; Gershenson, M. E.; Kloc, C.; Zeis, R.; Bucher, E. High-Mobility Field-Effect Transistors Based on Transition Metal Dichalcogenides. *Appl. Phys. Lett.* **2004**, *84*, 3301.

(13) Das, S.; Appenzeller, J. WSe2 Field Effect Transistors with Enhanced Ambipolar Characteristics. *Appl. Phys. Lett.* **2013**, *103*, 103501.

(14) Larentis, S.; Fallahazad, B.; Tutuc, E. Field-Effect Transistors and Intrinsic Mobility in Ultra-Thin MoSe2 Layers. *Appl. Phys. Lett.* **2012**, *101*, 223104.

(15) Street, R. A. Thin-Film Transistors. *Adv. Mater.* **2009**, *21*, 2007–2022.

(16) Li, X.; Magnuson, C. W.; Venugopal, A.; Tromp, R. M.; Hannon, J. B.; Vogel, E. M.; Colombo, L.; Ruoff, R. S. Large-Area Graphene Single Crystals Grown by Low-Pressure Chemical Vapor Deposition of Methane on Copper. *J. Am. Chem. Soc.* **2011**, *133*, 2816–2819.

(17) Klauk, H. Organic Thin-Film Transistors. *Chem. Soc. Rev.* **2010**, *39*, 2643–2666.

(18) Kamiya, T.; Nomura, K.; Hosono, H. Present Status of Amorphous In–Ga–Zn–O Thin-Film Transistors. *Sci. Technol. Adv. Mater.* **2010**, *11*, 044305.

(19) Nomura, K.; Ohta, H.; Takagi, A.; Kamiya, T.; Hirano, M.; Hosono, H. Room-Temperature Fabrication of Transparent Flexible Thin-Film Transistors Using Amorphous Oxide Semiconductors. *Nature* **2004**, *432*, 488–492.

(20) Duan, X.; Niu, C.; Sahi, V.; Chen, J.; Parce, J. W.; Empedocles, S.; Goldman, J. L. High-Performance Thin-Film Transistors Using Semiconductor Nanowires and Nanoribbons. *Nature* **2003**, *425*, 274–278.

(21) Engel, M.; Small, J. P.; Steiner, M.; Freitag, M.; Green, A. A.; Hersam, M. C.; Avouris, P. Thin Film Nanotube Transistors Based on Self-Assembled, Aligned, Semiconducting Carbon Nanotube Arrays. *ACS Nano* **2008**, *2*, 2445–2452.

Chapter 6. Engineering of CVD Graphene and R-GOC Films to Achieve Large Area Atomically Thin Free Standing Membranes for RF-Injector Windows

6.0 Abstract

Due to its crystalline and atomically thin structure, graphene possesses high electron transmittance and exceptional mechanical strength and stiffness. In this chapter the mechanical properties and diffusivity of large area (0.5 mm and 1 mm diameter) graphene (free-standing, reduced graphene oxide like carbon (R-GOC) supported, and poly(methyl methacrylate) (PMMA) supported) is studied. Combining the measured differential pressure at break from experiments with computational modelling of the system, the Young's modulus and strength at fracture of the films is extracted. Helium diffusivity experiments were carried out on R-GOC and PMMA supported graphene membranes to find the leak rate across the membranes, and computational models were used to extract the diffusivity. Fabrication of large area half millimeter diameter free standing and R-GOC supported graphene membranes and half millimeter to millimeter scale PMMA supported graphene membranes is demonstrated. Raman spectroscopy analysis confirmed that the majority of the PMMA support may be cleaned away using conventional solvents such as acetone, but this process generally results in fracture of the graphene membrane. It is demonstrated that the R-GOC film may be converted to graphene using laser irradiation on a 10 μm x 10 μm area. The obtained results described

in this chapter suggest that graphene is a promising material for RF photoinjector windows and laser irradiation of R-GOC may be the optimal route of fabrication for mm-scale graphene membranes.

6.1 Introduction

Graphene, first introduced into the science and engineering community by Novoselov and Geim,[1] has demonstrated remarkable electrical,[2] mechanical,[3] optical, [4] and thermal properties.[5] Single crystalline graphene from mechanical exfoliation has been demonstrated to be impermeable to helium.[6] As a result of its exotic properties, engineers have attempted to integrate graphene into applications in electronic, optical, and mechanical devices.

Advanced light sources produce x-ray light used for materials science, biology, chemistry, physics, and environmental science research.[7] Future light source applications require new cathode materials and designs with higher quantum efficiencies.[8] Metal cathodes are reliable and robust against contamination and may be transferred and installed at atmospheric pressures, but have low quantum efficiency.[8] Semiconductor cathodes offer improved quantum efficiency, but less reliability and robustness against contamination. For the purpose of improving the cathode through design, one can improve the robustness of the cathode to contamination, or improve the vacuum of the system. Graphene offers a potential method of improving the vacuum of the system.

Graphene is electron transparent[9] but gas impermeable[6] window material. Graphene would permit the emission of electrons from the semiconducting cathode while protecting the vacuum surrounding it from vacuum contamination. Because of the desire to maintain electron coherency, and prevent contamination of the cathode, it is best if the graphene is pristine, single crystalline and clean of any residues. Polymeric residues contain oxygen and carbon, which are specifically known to affect the performance of semiconducting cathodes.[10]

Polycrystalline graphene synthesis on Cu foils via chemical vapor deposition, followed by etching of the Cu and transfer of the graphene using PMMA as a handle and support is a conventional method of achieving graphene over large area on arbitrary substrates. Most of the PMMA can be removed after transfer using acetone or anisole and isopropyl alcohol (IPA).[11,12] This process is not ideal for producing suspended graphene membranes due to the inevitable PMMA residues left behind and the graphene breaking during the solvent cleaning.[11] For example, C. Lee et al. found about one graphene membrane (0.5 mm diameter) of nine survives when all nine are suspended on the same perforated substrate during cleaning. The broken membranes may help the last membrane to survive by allowing the solvent vapors a path to escape. But for the RF injector window engineering application, a single substrate with a single intact residue free window is required.

Free-standing multilayer graphene (30nm thick) synthesized on nickel was recently demonstrated to achieve graphene loudspeakers on the few mm scale, though there was no claim that the graphene was continuous or impermeable to gases.[13]

Another process of creating suspended graphene films is to first deposit R-GO flakes to form a film, then transfer the film to a perforated substrate.[14] A second option is to deposit GO flakes to form a film, then transfer the film to a perforated substrate, finally laser reducing the films to form turbostratic graphite.[15] These films, while not atomically thin or uniform, are able to be suspended on micron scale holes (~20 μm) without PMMA handles.[14,15]

Studies thus far on the mechanical properties of graphene have focused on membranes on the nanometer to micron scale,[3,6,16–18] though there are recent reports of larger scale graphene membrane fracture characteristics.[19] In the smaller scale case the mechanical properties are extracted by measuring the bulge of the graphene membrane suspended over a pit in silicon for a given pressure differential from ambient using AFM,[6] or by indenting the membrane with an AFM tip.[3] Larger scale experiments (~90 μm diameter membranes) mainly focus on fracture mechanics, finding that ambient water causes stress corrosion fracturing of the graphene film.[19]

This chapter will describe the fabrication and characterization of half millimeter scale graphene membranes with and without R-GOC or PMMA support as well as millimeter scale graphene membranes with PMMA support. This will include both direct experimental results and extracted materials properties from computational modelling. This chapter also includes laser irradiation experiments of the R-GOC films to achieve free standing graphene.

6.2 Experimental Methods

Single and bilayer graphene and 10 nm thick R-GOC films were synthesized on copper foil via chemical vapor deposition (see chapters 3 and 4 for more details). The graphene was transferred to stainless steel apertures via the conventional PMMA transfer method. The R-GOC films were transferred without any handle.

A micro-Raman spectrometer was used with variable wavelength excitation and laser power to characterize the membranes. Laser ablation of the R-GOC was performed with the micro-Raman spectrometer at variable wavelength excitation and laser power.

The prepared stainless steel apertures with graphene membranes were placed in a vacuum chamber with pressure controlled on each side. Differential pressure was applied by holding one side at atmosphere and pumping the other to low vacuum. The membrane was observed to break by the change in transmission intensity of a laser.

The prepared stainless steel apertures PMMA supported or R-GO supported graphene were placed in the same setup as the mechanical robustness testing. Both sides were pumped down to low vacuum ($1x10^{-6}$ Torr), and allowed to outgas for 20 minutes. The pressure in on each side reaches $0.8\text{-}1.1x10^{-5}$ Torr during outgassing. Pump down again ~1 h to recover vacuum, isolate both sides and pump down to $7\text{-}8x10^{-6}$ Torr. Then a controlled helium supply is introduced to one side. The leak rate of helium across the membrane is monitored by helium gauges on the pump that is isolated on the other side of the membrane.

COMSOL computational software was used to model the strength of the membranes at break, as well as the helium diffusivity of the membranes.

6.3 Results of the Experiments

Figure 6.1 shows optical images of typical graphene membranes transferred to stainless steel before and after acetone IPA cleaning. Raman spectra of the graphene film before and after acetone cleaning are shown in Fig. 6.2.

There are several important features visible in these Raman spectra, including the 2D peak (centered about 2700 cm^{-1}), the G peak (centered about 1580 cm^{-1}), and the D peak (centered about 1350 cm^{-1}), the second order D' peak (~1620 cm^{-1}) and the disorder induced combination mode D+G (~2950cm^{-1}).[20] It is clear from the 2D peak to G peak ratio (>1.5) that these are spectrums of graphene films with less than 3 layers. In addition to

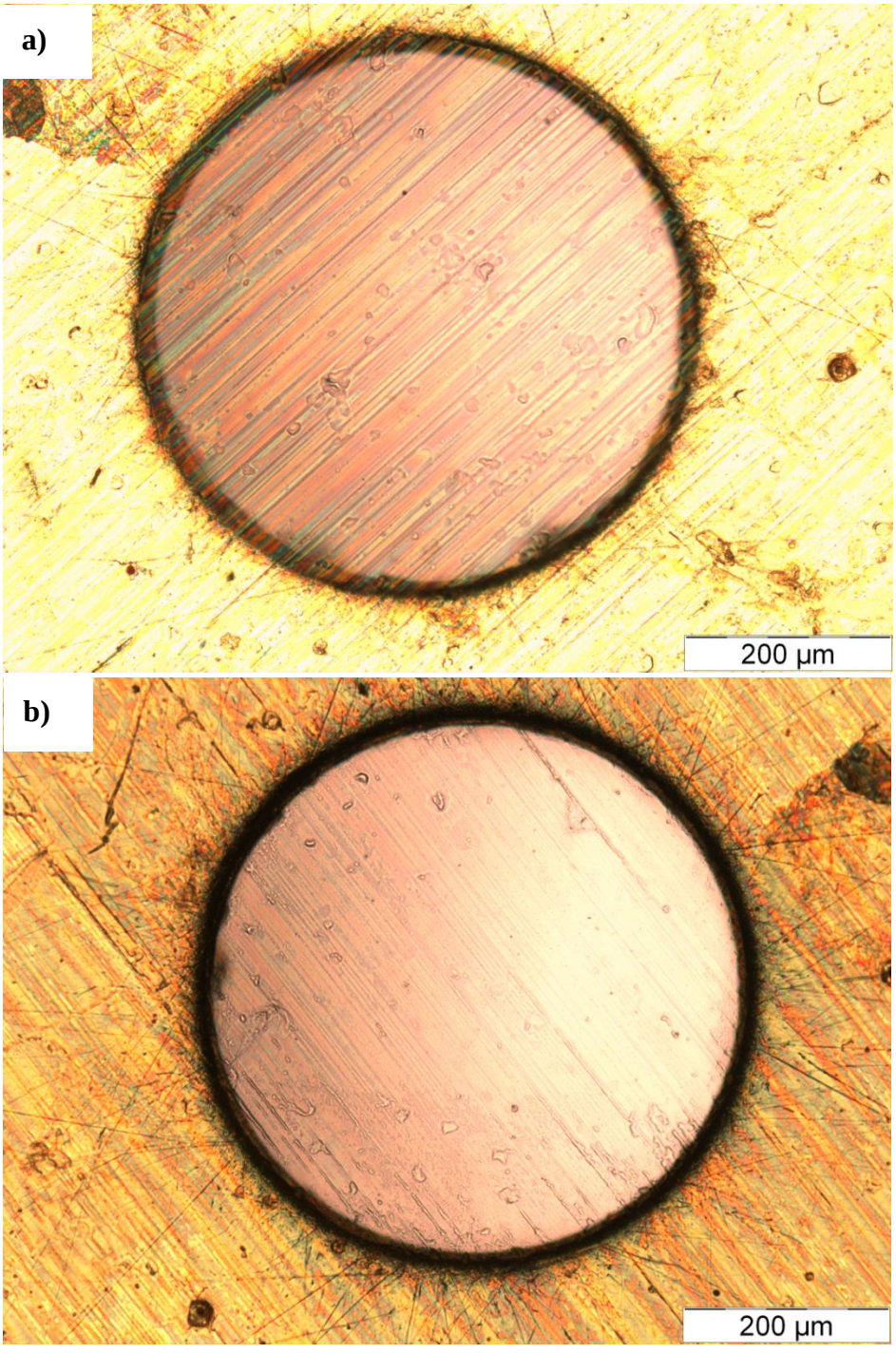


Figure 6.1. Optical images of graphene membranes transferred to stainless steel without treatment (a) and after solvent cleaning (b).

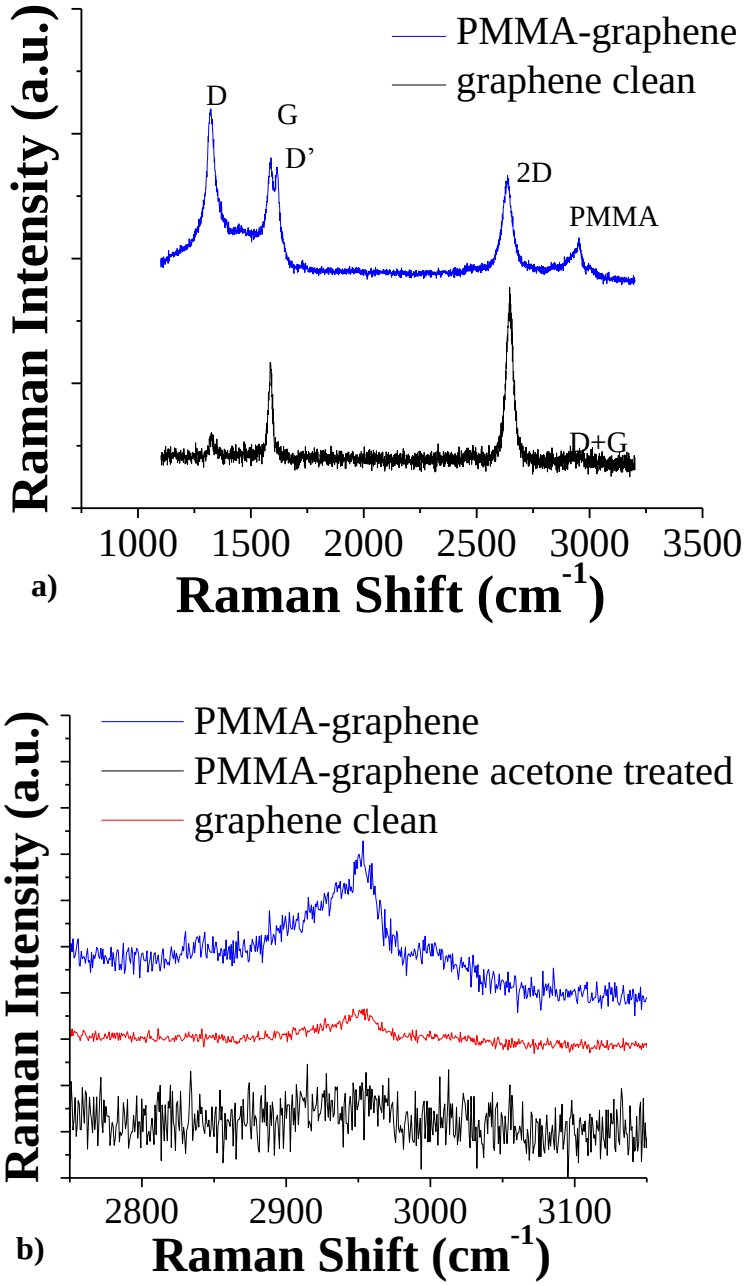


Figure 6.2. Raman spectra of membrane before (blue) and after cleaning (black) (a), PMMA bands from Raman spectra of graphene membranes without treatment (blue), after one treatment with acetone (red), after repeated application of acetone, followed by IPA (black) (b), 633nm excitation.

the peaks of graphene, there is a set of peaks around ~2950 cm^{-1} that are characteristic of PMMA.[21] After repeated acetone treatments, with IPA treatment to finish the cleaning, the PMMA signature is found to reduce to the background D+G peak intensity.

Figure 6.3 shows a plot from one of the differential pressure testing experiments. A laser, which transmits through the window, is used to determine the pressure differential when the graphene ruptures. It was observed that the clean graphene membrane (in this case half millimeter) can withstand a differential pressure of ~79.5±.7 Torr. The PMMA supported graphene can withstand greater pressure differential ~700 Torr. Several PMMA supported graphene membranes were tested for helium diffusivity, as described in the methods section. The helium leak rate across the tested PMMA-single layer graphene membrane was found to be 6×10^{-10} mbar-L/s. Table 6.1 provides a summary of the differential pressure and helium testing for all the membranes. The transmitted light intensity of the laser changes significantly between different membrane types. Judging by the increase in differential pressure potential (about a factor of 2 increase), the PMMA handle seems to provide significant mechanical support and strength to the graphene. The membranes appear to fail due to brittle fracture (see Fig. 6.4). The fracture is initiated at the defects that result from the copper foil having bulges and valleys. The PMMA transfer process transfers the topology of the copper foil to the resulting membrane. Thus, bulges in the copper translate to bulges in the membrane (see Fig. 6.5).

Sample Type	Size (mm)	ΔP (Torr)	ΔI_0 (%)	He leak rate Outlet Side (mbar*L/s)
bilayer graphene	0.5	79.5 ± 0.5	8.2 ± 4.4	--
PMMA + bilayer graphene	0.5	208.2 ± 50.7	11.0 ± 0.8	
PMMA + bilayer graphene	1	45	3.1	
PMMA + monolayer graphene	0.5	~0	3	1.4×10^{-9}
PMMA +monolayer graphene	1	111	21.6	1.2×10^{-9}
R-GOC 10 nm + monolayer graphene	0.5	--	9.1	1.2×10^{-11}
PMMA	0.5	0	3.7	1.0×10^{-10}
PMMA	1	80	5.2	5.0×10^{-10}

Table 6.1. Summary of differential pressure testing and helium leak rate testing of graphene membranes, including the absorbed light intensity of the membrane.

In an effort to remove the defects from the membrane, different CVD processes for graphene growth were investigated. It was found that the surface of the copper can be made bulge or valley free by reducing the hydrogen anneal time of the copper foil (see Fig 6.6). However, with shorter anneal times, the folds present from the rolling process of the copper foil may also initiate fracture.

The bulges can be problematic not just as points for brittle fracture initiation, but also from the stand point of improving the yield and survivability of the membranes through the

cleaning process. A membrane that has pits and valleys is more likely to develop pinhole defects during the acetone cleaning.

Optical images transferred R-GOC films are given in Fig. 6.7. The 0.5 mm diameter membrane in Fig. 6.7a has folds that occur during the transfer process as the film floats freely in water, while the smaller membranes (Fig. 6.7c) have smaller creases from the

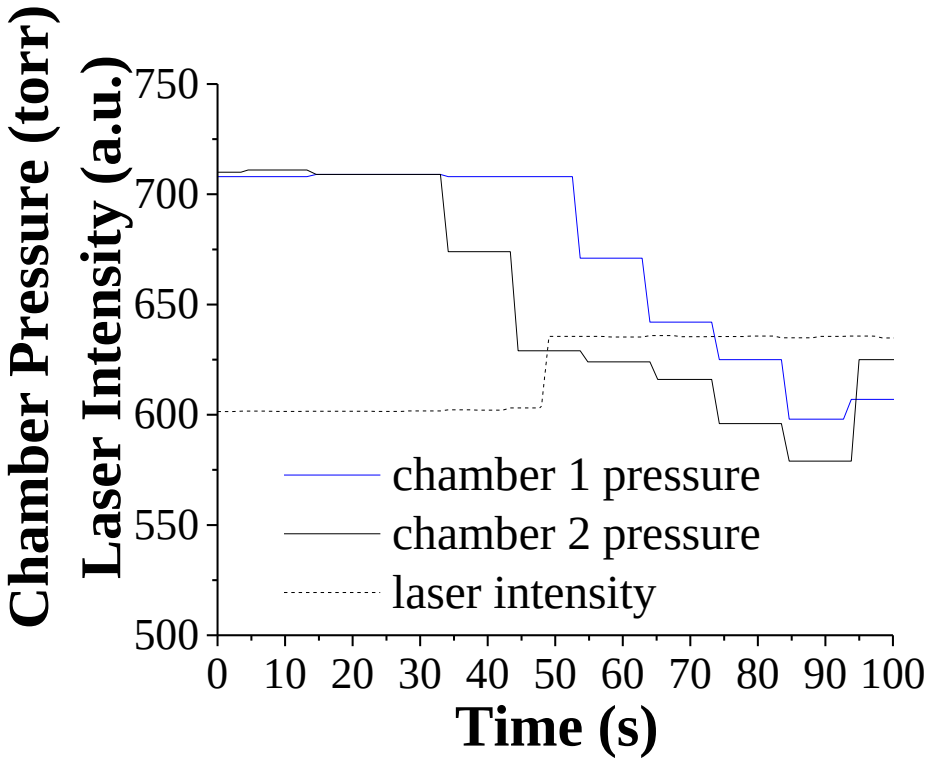


Figure 6.3. Plot of pressure gauge readings of each chamber with transmission intensity of the laser during a differential pressure test of clean bilayer graphene membrane. The Differential pressure is the difference between the pressure in chamber 1 and chamber 2. The window breaks when the laser intensity abruptly increases. At that point chamber 1 pressure starts to decrease from atmospheric pressure. This plot indicates the membrane withstood 80 Torr of pressure differential before breaking.

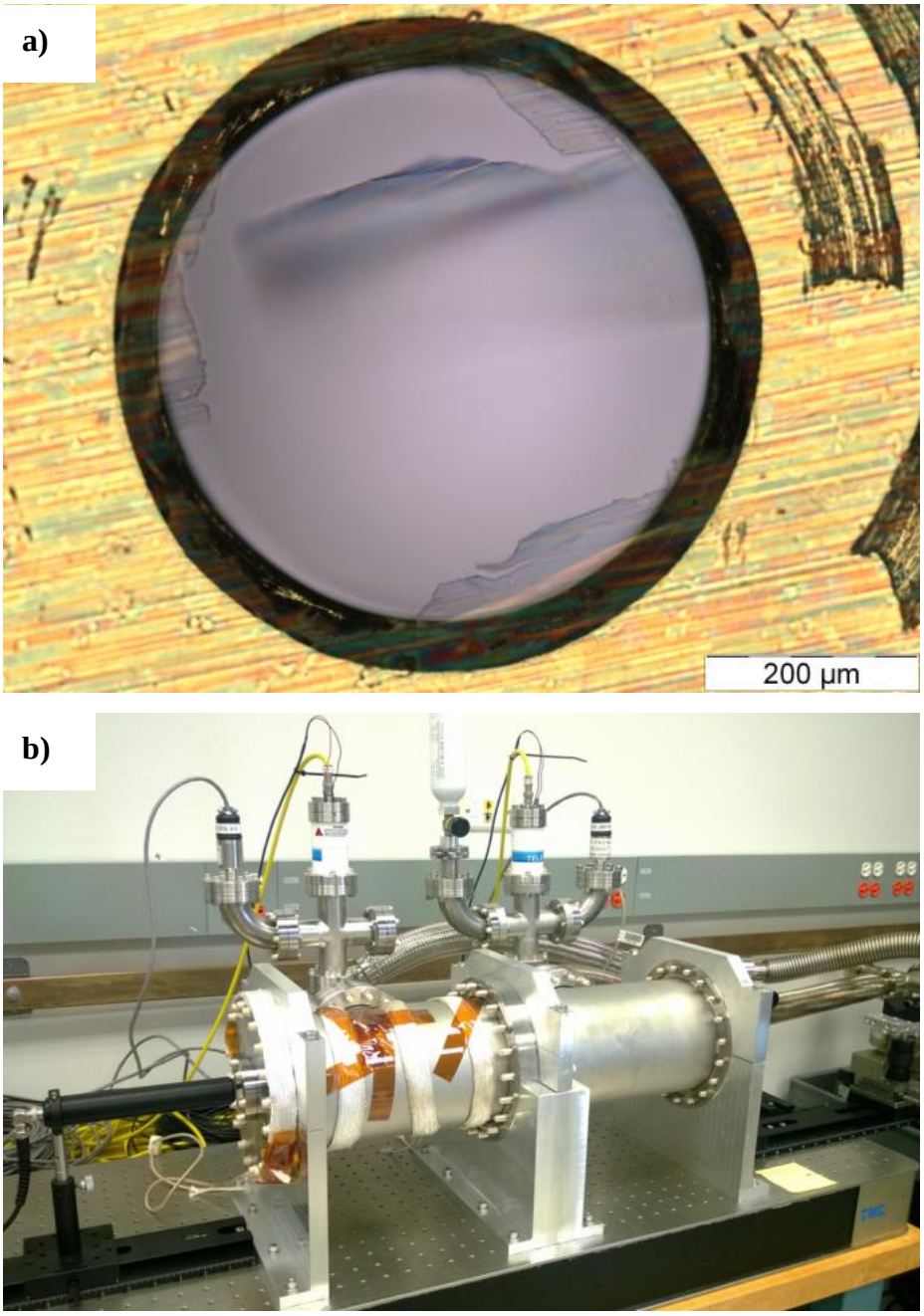


Figure 6.4. Optical images of half-millimeter diameter graphene membrane on stainless steel aperture after differential pressure testing was completed (a), Differential pressure and helium leak rate testing setup (b).

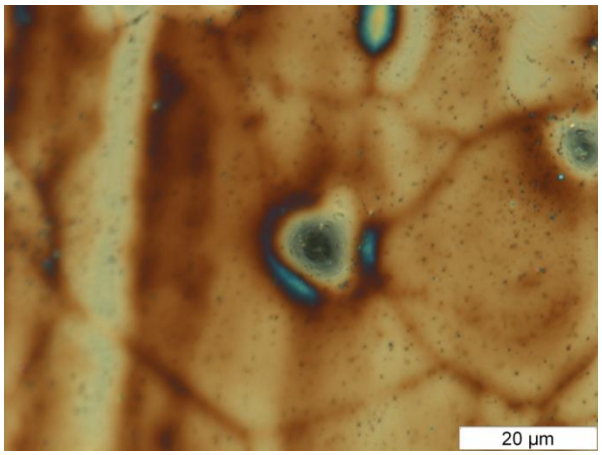


Figure 6.5. Optical image of bilayer graphene membrane supported by PMMA. Dark pit is graphene with thin PMMA coating.

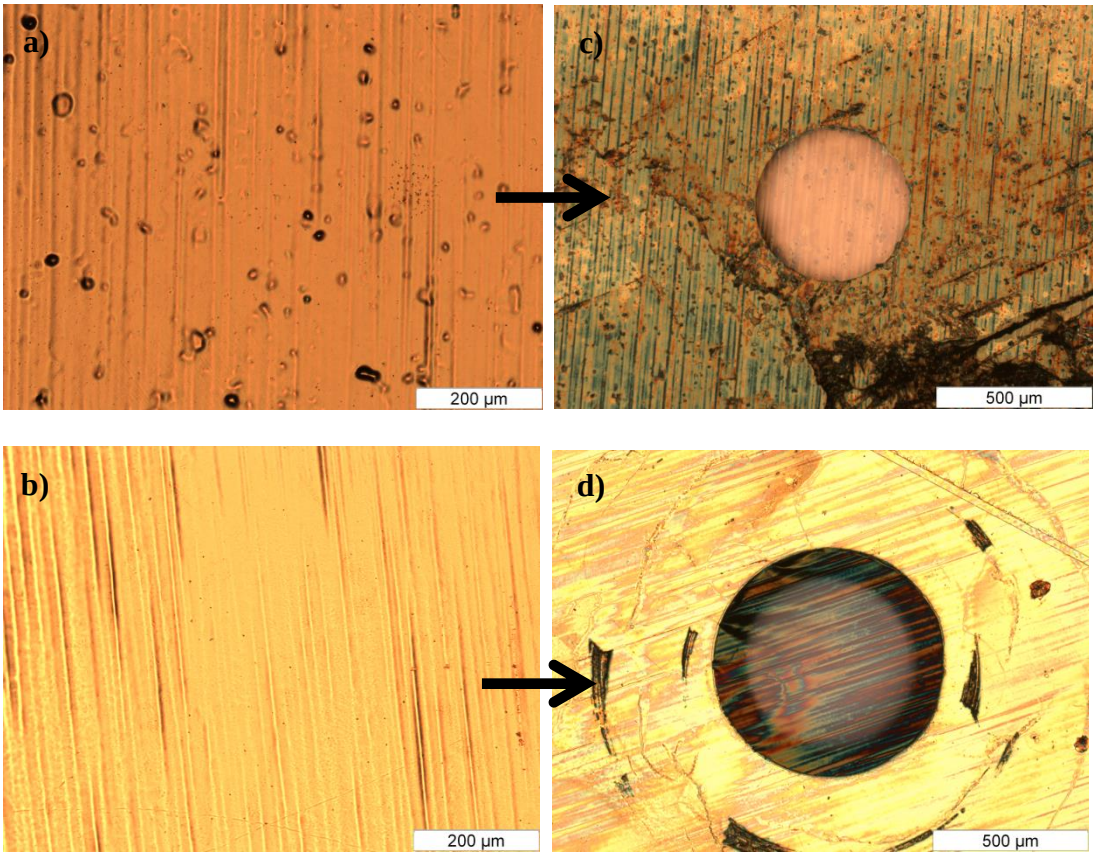


Figure 6.6. Optical images of Cu foils with extended 30 minute hydrogen anneal at 800 °C with ramp to deposition temperature in hydrogen (a), without the annealing (b), and corresponding graphene membranes fabricated from the films on Si aperture (c) and stainless steel aperture (d).

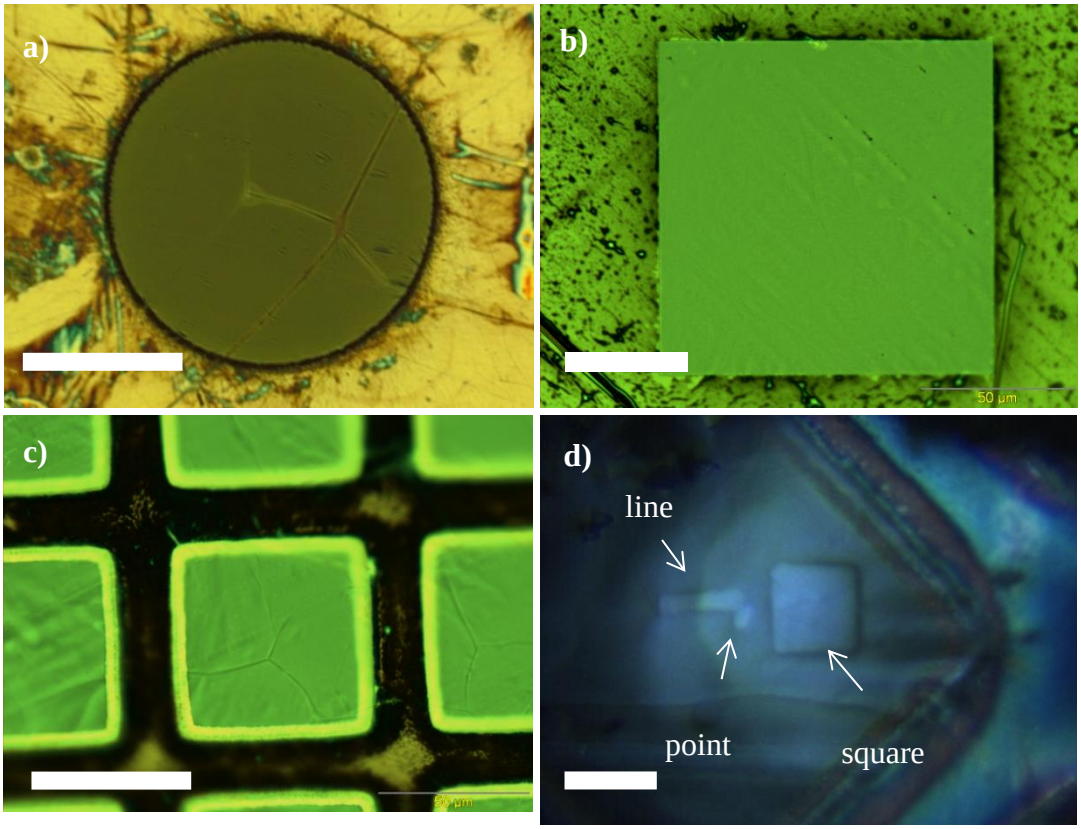


Figure 6.7. Optical images of R-GOC membranes transferred to 0.5 mm stainless steel aperture (a), 0.1 mm square silicon TEM grid (b), and 50 µm square Cu TEM grids (c), (d). The R-GOC film in (d) was selectively exposed to 325 nm laser light (5.5 mW) at a point, a line, and a 10 µm *x* 10 µm square using Scale bars are 50 µm, 200 µm and 50 µm, and 10 µm.

grains in the copper foil. Figure 6.7d is an optical image of the R-GOC film after exposure to 325nm laser light at 5.5mW in a point, line, and 10 µm *x* 10 µm square (see Fig. 6.7d). Raman spectroscopy of the R-GOC film after the 325nm laser exposure indicate that the film is single layer graphene with (2.2 ± 1.0):1 2D peak to G peak ratio, (1.2 ± 0.6):1 D to G peak ratio and FWHM 38.2 ± 5.1 cm^{-1} (see Fig. 6.8).

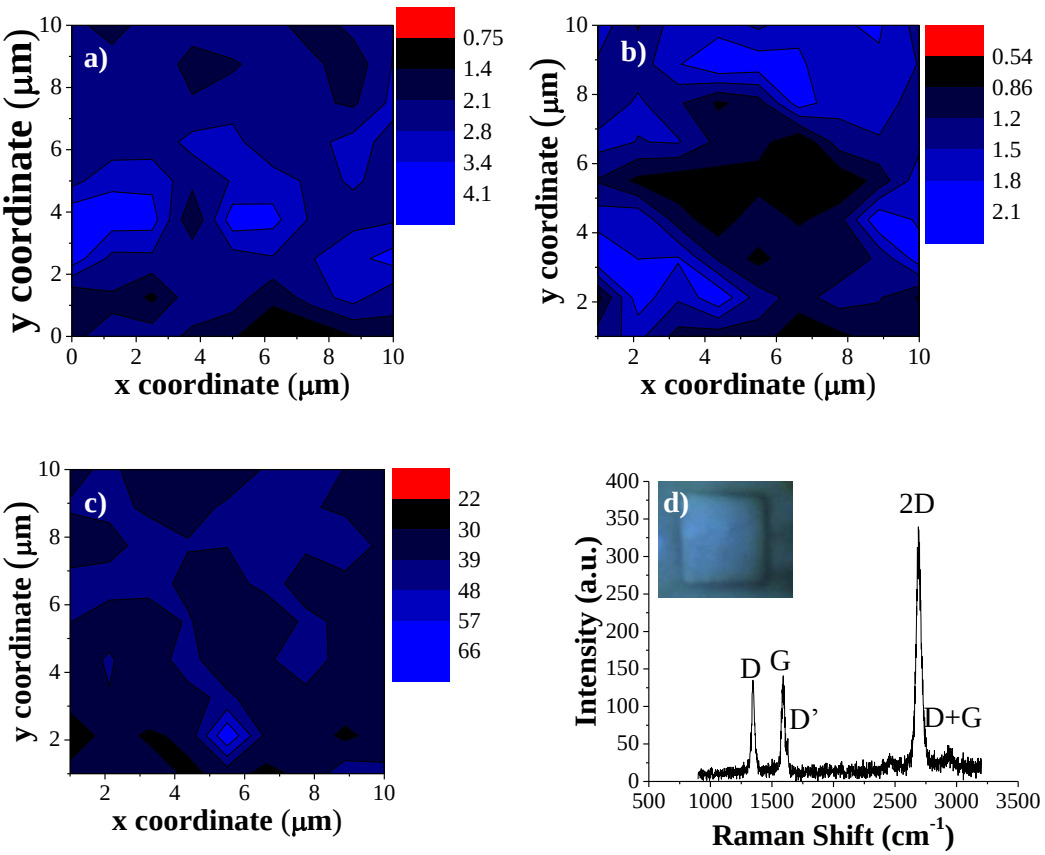


Figure 6.8. Spatial Raman maps of 325nm ablated R-GOC film: 2D/G peak intensity ratio (a), D/G peak intensity ratio (b), 2D peak FWHM (c), and typical Raman spectra (d) (inset optical image of ablated film).

6.4 Discussion

The ultimate goal that the research in this chapter is pursuing is to achieve a facile process for fabricating a free-standing continuous single layer graphene membrane on the millimeter scale. While the PMMA transfer is readily achievable, difficulties were encountered in cleaning PMMA handle away. PMMA-free processes were pursued. One method found was to utilize reduced graphene oxide like carbon films (R-GOC) as the transfer handle. It is possible that a graphene layer forms beneath the as fabricated 10 nm

thick R-GOC film on Cu during the R-GOC film synthesis. The fact that laser ablation may be used to remove the R-GOC, leaving behind a film with graphene Raman signatures suggests that the R-GOC film grown on copper possesses a graphene layer. Regardless, the laser ablation technique provides a new pathway for achieving freestanding graphene using large area R-GOC film.

While the leak rates and pressure difference at rupture are indications of diffusivity and strength, respectively, finding the intrinsic properties of the film requires further interpretation. The results of COMSOL diffusivity and mechanical simulations are given in Figure 6.9 and 6.10-12, respectively. The helium was introduced at a rate of 5.2×10^{-8} mbar-L/s for 1 s. Accounting for chamber geometry, pressures, and using the ideal gas law, this corresponds to introducing a concentration of ~$2 - 3 \times 10^{-10}$ mol/m^3. Using the same analysis and the measured helium leak rates on the outlet side from Table 6.1, the concentration of helium on the outlet side was calculated. The simulations were carried out such that the membrane's diffusivity causes the experimentally measured concentration on the outlet side after 1 s. In practice, the helium leak rate detector saturates to the max concentration within 1 s of introducing the concentration to the inlet side during the helium leak rate experiment. The diffusivity of the PMMA supported graphene films are similar to the neat PMMA film. Whereas the diffusivity of the R-GOC film is two orders of magnitude less than PMMA supported graphene films (see Table 6.2).

The helium leak rate experiment can be interpreted as the diffusion of a finite source in non-steady state. For a non-steady state finite source, the concentration profile *C(x, t)* is given by

$$C(x,t) = \frac{Q}{\sqrt{\pi D t}} e^{-\frac{-x^2}{4Dt}} \quad , \qquad (6.1)^{22}$$

where *Q* is the initial concentration, *D* is the diffusivity, *t* is time, and *x* is the diffusion distance (thickness of the film). Using Wolfram Alpha's computational knowledge engine (available free online), we find that the diffusivity can be solved from eq 6.1 as:

$$D = -\frac{x^2}{2tW\left[-\frac{C(x,t)^2 \pi x^2}{2Q^2}\right]} \quad , \qquad (6.2)$$

where *W[z]* is the Lambert-W or product log function. From eq 6.2 we calculate the diffusivity of the membranes (see table 6.2).

The mechanical simulations were carried to determine the Young's modulus, *E*, and breaking stress σ_{MAX} of the supported graphene membranes. The optical microscopy images of the membranes after rupture show little deformation occurs before the film breaks. This indicates that the graphene membranes fail by brittle fracture, with strains of less than 2-5%. COMSOL simulations were carried out to fit the Young's modulus of the graphene membranes such that 2% strain maximum occurs in the membrane at the measured pressure differentials. Although the pressure differentials were measured in real time (see figure 6.3), the measurements are more qualitative and comparative than

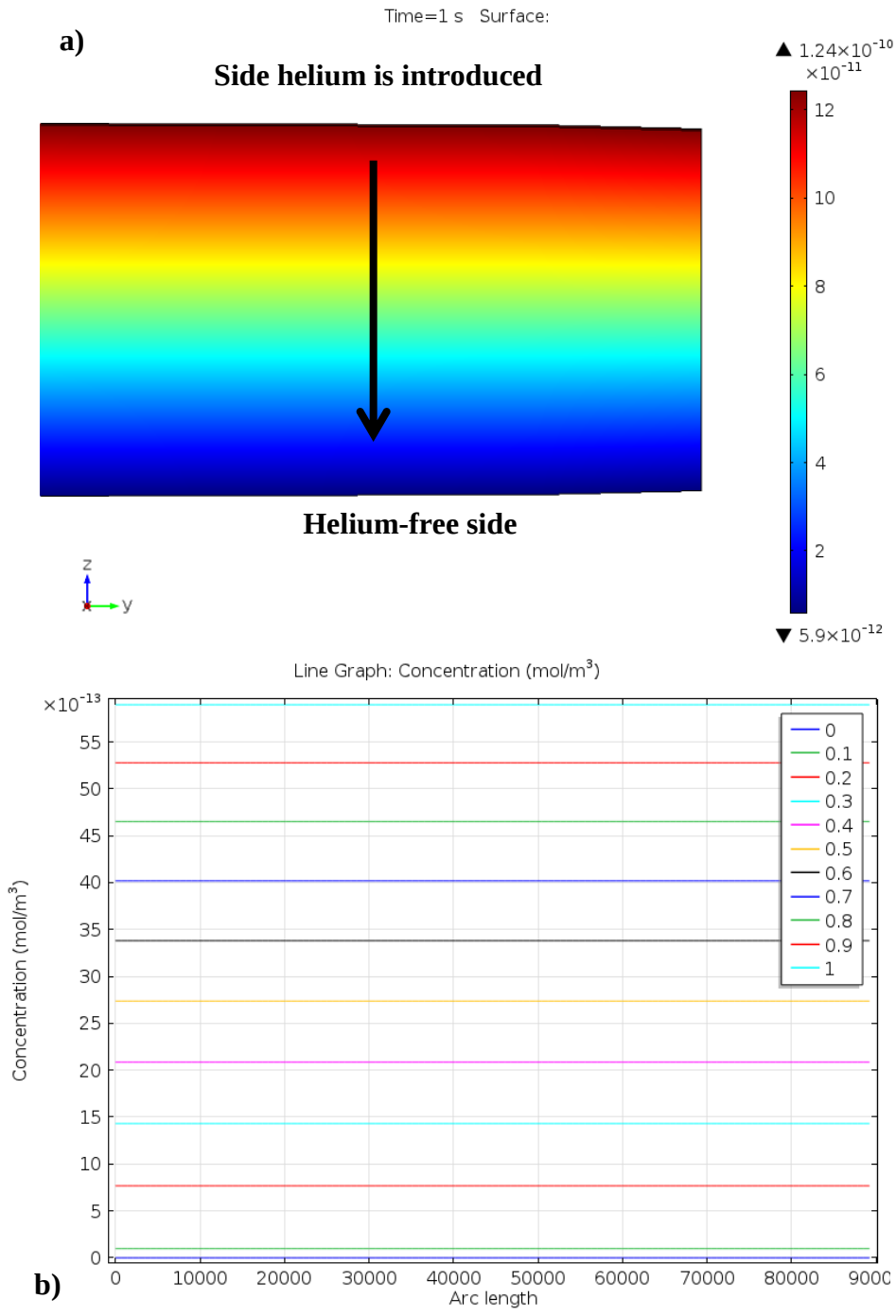


Figure 6.9. Helium leak rate simulation 2D surface map of PMMA + graphene membrane cross section 1 s after He is introduced (a), surface concentration line plot of "Helium-free side" for 0.5 mm diameter PMMA + graphene membrane 1 s after He is introduced (b).

Sample Type	Size (mm)	Measured Leak rate (mbar-L/s)	Calculated Diffusion Coefficient (m^2/s)	Simulated Diffusion Coefficient (m^2/s)
PMMA (220 nm) + monolayer graphene	0.5	1.2×10^{-9}	5.83×10^{-16}	4.20×10^{-16}
R-GOC (10 nm)	0.5	2.0×10^{-11}	8.99×10^{-19}	3.23×10^{-19}
PMMA (220 nm)	0.5	1.0×10^{-10}	5.73×10^{-16}	3.00×10^{-16}
PMMA (220 nm)	1	5.0×10^{-10}	5.68×10^{-16}	2.50×10^{-16}

Table 6.2. Summary of diffusivity simulation results for PMMA and R-GOC membranes including the neat PMMA film for comparison.

absolute, as the pressure experienced at the membrane may be different from the pressure measured at the gauges. For the purpose of calibration neat PMMA membranes were tested. It was found that the mechanical simulation returns *E* significantly larger (57 GPa) than the literature value for PMMA (3 GPa) [23] at the measured differential pressures, if the membranes are assumed to break in brittle fracture at 2% strain. The pressure differentials were proportionally fit so that the simulation returns E = 3GPa at 2% strain for the neat PMMA membrane. The simulation summary is given in Figures 6.10-12, and the results in Table 6.3. The PMMA supported monolayer graphene had the highest simulated elastic modulus $E = 4 \pm 0.3$ GPa, with $\sigma_{MAX} = 161 \pm 4.00$ MPa (see Table 6.3).

For a square membrane of width *W*, deflection *z*, Young's modulus *E*, thickness *t*, and Poisson's ratio *v*, the relation between the Young's modulus and the applied differential pressure Δp, may be described by:

$$\Delta p = \frac{4z}{W^2}\left(c_1 S_o + \frac{4c_2 E t z^2}{W^2(1-v)}\right), \qquad (6.3)\ [6]$$

where S_0 is the initial tension per unit length along the boundary, *z* is the deflection, c_1 = 3.393 and $c_2 = (.8 + 0.062v)^{-3}$. The deflection may be related to *W* by

$$z = W \sin\theta \tan\theta, \qquad (6.4)$$

where θ is the angle the membrane makes with respect to the normal from the surface.

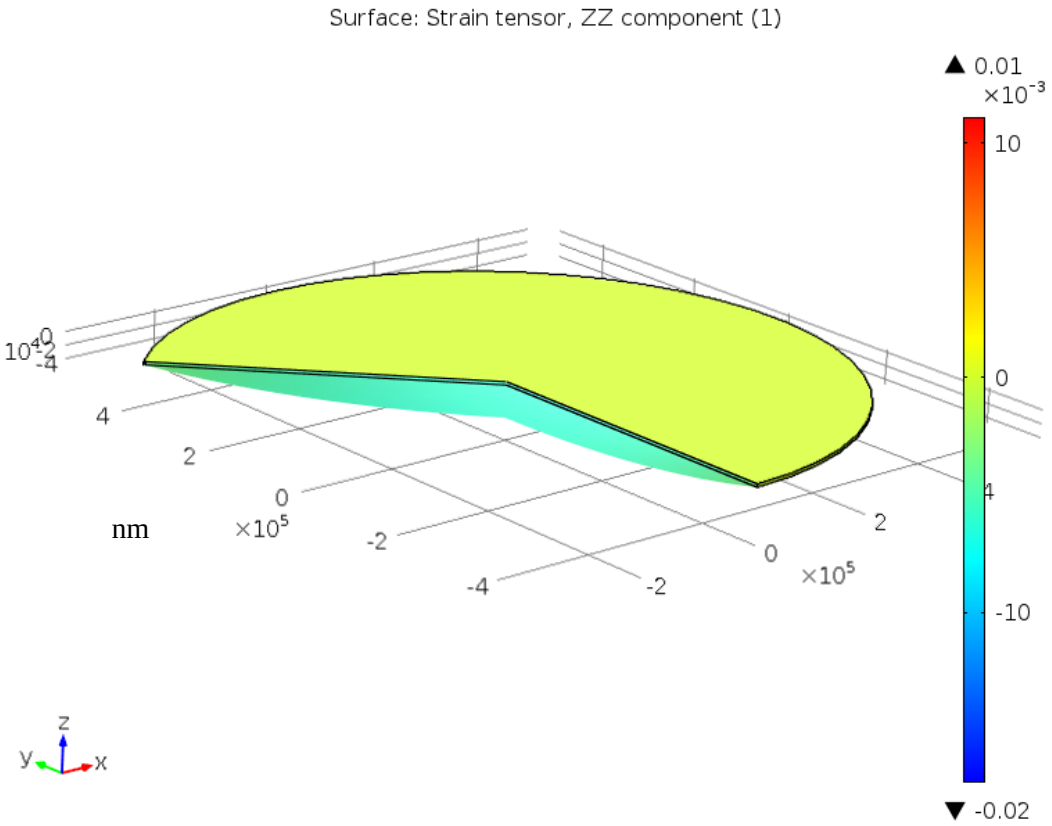


Figure 6.10. Mechanical simulation of strain distribution in PMMA-supported bilayer graphene during differential pressure test (1 mm diameter, 220 nm thickness).

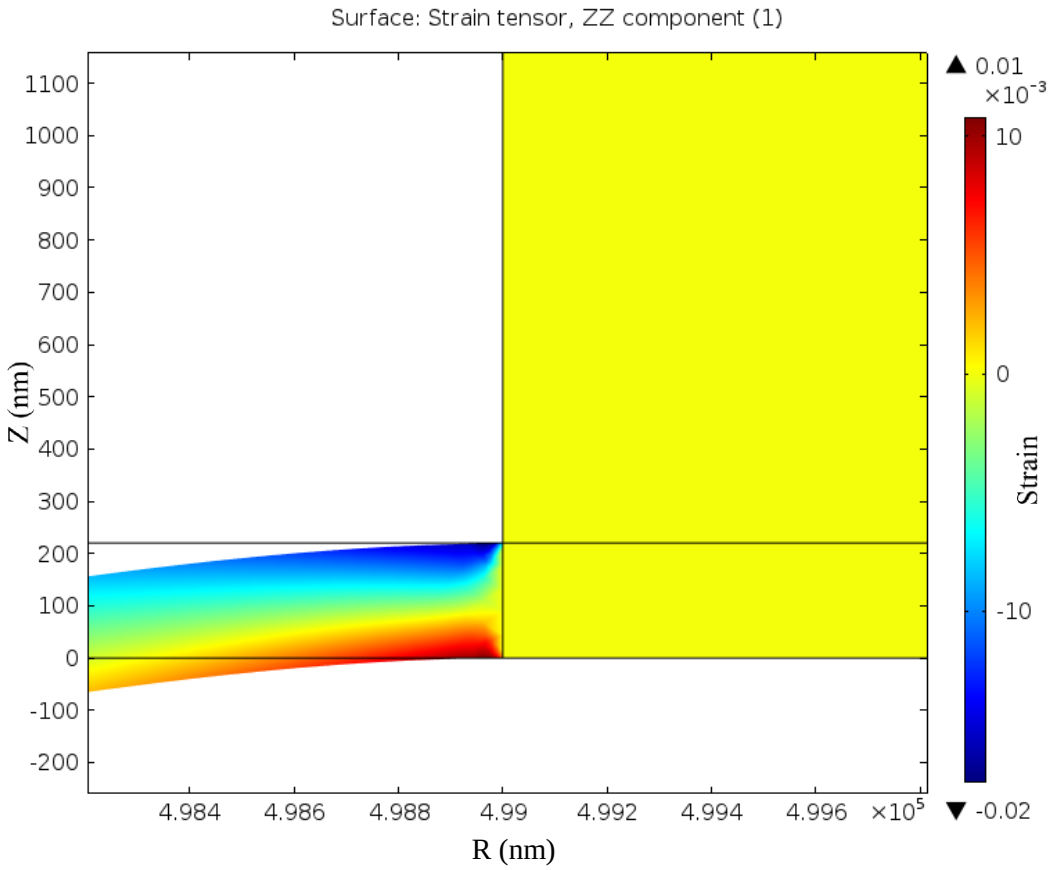


Figure 6.11. Mechanical simulation of strain distribution in the connecting edge of the PMMA-supported bilayer graphene during differential pressure test (1 mm diameter, 220 nm thickness).

Because the films are exceptionally thin compared to *W*, we may use the Young-Laplace equation to describe the relation between the pressure and the membrane tension, *S*:

$$\Delta p = \frac{2S\cos\theta}{W/2}. \qquad (6.5)$$

Finally, the strain, ε, may be related to the tension by

$$\varepsilon = \frac{S(1-\nu)}{Et} \qquad (6.6)^{6}$$

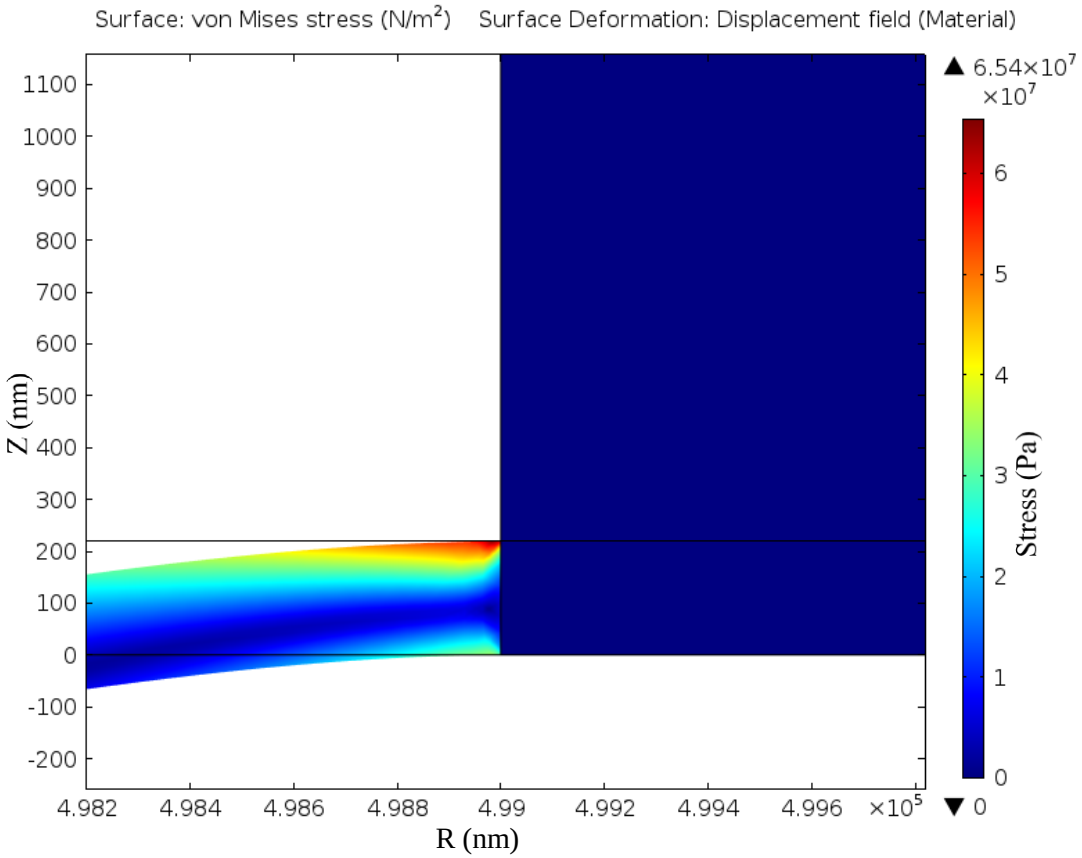


Figure 6.12. Mechanical simulation of stress at maximum strain (2%) in the connecting edge of the PMMA-supported bilayer graphene during differential pressure test (1 mm diameter, 220 nm thickness).

Assuming no initial tension and the Young's modulus of the PMMA is equal to the literature value (3GPa)[23], we use eqs 6.3-6and find that the strain and angle at the rupturepressure are calculated to be ~0.3% and 15.2°. The Young's moduli of the remaining membranes are varied until the differential pressure calculated is equal to the measured differential pressure at $\varepsilon = 0.3\%$ and $\theta = 15.2°$. The strain at rupture calculated is an order of magnitude smaller then observed in the COMSOL simulations for the same elastic moduli, though the relative differences in the Young's Moduli of the membranes are

Sample Type	Size (mm)	E (GPa)	σ_{MAX} (MPa)
PMMA (220 nm) + monolayer graphene	1	4.3± 0.3	161 ± 4.00
PMMA (220 nm) + bilayer graphene	0.5	3.3± 0.9	144 ± 11.5
PMMA (220 nm) + bilayer graphene	1	1.7 ± 0.2	65.3 ± 1.70
PMMA (220 nm)	1	3.0 ± 0.3	117 ± 3.50

Table 6.3. Summary of mechanical simulation results for PMMA supported membranes including the neat PMMA film for comparison.

Sample Type	Size (mm)	E (GPa)
PMMA (220 nm) + monolayer graphene	1	4.1
PMMA (220 nm) + bilayer graphene	1	1.8
PMMA (220nm) + bilayer graphene	0.5	4.1
bilayer graphene (1 nm)	0.5	340
PMMA (220 nm)	1	3.0

Table 6.4. Summary of calculated Young's moduli for graphene membranes. Neat PMMA film is included for comparison.

similar for the calculations and the simulations (compare table 6.3 and 6.4). For the graphene membrane, the assumed strain of 0.3% is in line with the maximum strain observed in a mechanical characterization study of mechanically exfoliated graphene.[6] The calculated Young's modulus for the bilayer graphene samples is 0.3TPa, while the observed value for single layer graphene is ~1-1.3 TPa.[6]

6.5 Conclusions

In this chapter, the fabrication methods for freestanding graphene membranes were demonstrated using PMMA supported transfer and solvent cleaning, as well as R-GOC film transfer and laser irradiation. The fabricated windows were found to have low helium diffusivity based on computational models and experimental he leak rate data, and significant mechanical robustness based on experimentally measured differential pressures at break and computational models. This chapter highlights the potential of CVD R-GOC films as an important part of achieving the future of RF injector window technology.

6.6 Acknowledgements

This work was performed at the Center for Nanoscale Materials and the Advanced Photon Source at Argonne National Laboratory. Use of the Center for Nanoscale Materials was supported by the U.S. Department of Energy, Office of Science, Office of Basic Energy Sciences, under Contract No. DE-AC02-06CH11357. This work was supported by the LDRD Director's Competitive Grants of ANL (Proposal Number #2013-096-N0).

REFERENCES AND NOTES

(1) Geim, A. K.; Novoselov, K. S. The Rise of Graphene. *Nat. Mater.* **2007**, *6*, 183–191.

(2) Bolotin, K. I.; Sikes, K. J.; Jiang, Z.; Klima, M.; Fudenberg, G.; Hone, J.; Kim, P.; Stormer, H. L. Ultrahigh Electron Mobility in Suspended Graphene. *Solid State Commun.* **2008**, *146*, 351–355.

(3) Lee, C.; Wei, X.; Kysar, J. W.; Hone, J. Measurement of the Elastic Properties and Intrinsic Strength of Monolayer Graphene. *Science* **2008**, *321*, 385–388.

(4) Wang, X.; Zhi, L.; Müllen, K. Transparent, Conductive Graphene Electrodes for Dye-Sensitized Solar Cells. *Nano Lett.* **2008**, *8*, 323–327.

(5) Balandin, A. A.; Ghosh, S.; Bao, W.; Calizo, I.; Teweldebrhan, D.; Miao, F.; Lau, C. N. Superior Thermal Conductivity of Single-Layer Graphene. *Nano Lett.* **2008**, *8*, 902–907.

(6) Bunch, J. S.; Verbridge, S. S.; Alden, J. S.; van der Zande, A. M.; Parpia, J. M.; Craighead, H. G.; McEuen, P. L. Impermeable Atomic Membranes from Graphene Sheets. *Nano Lett.* **2008**, *8*, 2458–2462.

(7) Advanced Light Source: Quick Facts http://www-als.lbl.gov/index.php/about-the-als/quick-facts.html.

(8) Dowell, D. H.; Bazarov, I.; Dunham, B.; Harkay, K. Cathode R & D for Future Light Sources Written for the BES Workshop on Accelerator R & D for Future Light Sources. *NIM* **2010**, 685.

(9) Stoll, J. D.; Kolmakov, A. Electron Transparent Graphene Windows for Environmental Scanning Electron Microscopy in Liquids and Dense Gases. *Nanotechnology* **2012**, *23*, 505704.

(10) Chanlek, N. Quantum Efficiency Lifetime Studies Using the Photocathode Preparation Experimental Facility Developed for the ALICE Accelerator, 2011, pp. 94–135.

(11) Lee, C.-K.; Hwangbo, Y.; Kim, S.-M.; Lee, S.-K.; Lee, S.-M.; Kim, S.-S.; Kim, K.-S.; Lee, H.-J.; Choi, B.-I.; Song, C.-K.; et al. Monoatomic Chemical-Vapor-Deposited Graphene Membranes Bridge a Half Millimeter-Scale Gap. *ACS Nano* **2014**, *8*, 2336–2344.

(12) Lin, Y.-C.; Jin, C.; Lee, J.-C.; Jen, S.-F.; Suenaga, K.; Chiu, P.-W. Clean Transfer of Graphene for Isolation and Suspension. *ACS Nano* **2011**, *5*, 2362–2368.

(13) Zhou, Q.; Zettl, A. Electrostatic Graphene Loudspeaker. *Appl. Phys. Lett.* **2013**, *102*, 223109.

(14) Robinson, J. T.; Zalalutdinov, M.; Baldwin, J. W.; Snow, E. S.; Wei, Z.; Sheehan, P.; Houston, B. H. Wafer-Scale Reduced Graphene Oxide Films for Nanomechanical Devices. *Nano Lett.* **2008**, *8*, 3441–3445.

(15) Zalalutdinov, M. K.; Robinson, J. T.; Junkermeier, C. E.; Culbertson, J. C.; Reinecke, T. L.; Stine, R.; Sheehan, P. E.; Houston, B. H.; Snow, E. S. Engineering Graphene Mechanical Systems. *Nano Lett.* **2012**, *12*, 4212–4218.

(16) Lee, S.; Chen, C.; Deshpande, V. V.; Lee, G.-H.; Lee, I.; Lekas, M.; Gondarenko, A.; Yu, Y.-J.; Shepard, K.; Kim, P.; et al. Electrically Integrated SU-8 Clamped Graphene Drum Resonators for Strain Engineering. *Appl. Phys. Lett.* **2013**, *102*, 153101.

(17) Ruiz-Vargas, C. S.; Zhuang, H. L.; Huang, P. Y.; van der Zande, A. M.; Garg, S.; McEuen, P. L.; Muller, D. A.; Hennig, R. G.; Park, J. Softened Elastic Response and Unzipping in Chemical Vapor Deposition Graphene Membranes. *Nano Lett.* **2011**, *11*, 2259–2263.

(18) Suk, J. W.; Piner, R. D.; An, J.; Ruoff, R. S. Mechanical Properties of Monolayer Graphene Oxide. *ACS Nano* **2010**, *4*, 6557–6564.

(19) Hwangbo, Y.; Lee, C.-K.; Kim, S.-M.; Kim, J.-H.; Kim, K.-S.; Jang, B.; Lee, H.-J.; Lee, S.-K.; Kim, S.-S.; Ahn, J.-H.; et al. Fracture Characteristics of Monolayer CVD-Graphene. *Sci. Rep.* **2014**, *4*, 4439.

(20) Campos-Delgado, J.; Romo-Herrera, J. M.; Jia, X.; Cullen, D. a; Muramatsu, H.; Kim, Y. A.; Hayashi, T.; Ren, Z.; Smith, D. J.; Okuno, Y.; et al. Bulk Production of a New Form of sp(2) Carbon: Crystalline Graphene Nanoribbons. *Nano Lett.* **2008**, *8*, 2773–2778.

(21) Yoshimura, S.; Tsukazaki, Y.; Kiuchi, M.; Sugimoto, S.; Hamaguchi, S. Sputtering Yields and Surface Modification of Poly(methyl Methacrylate) (PMMA) by Low-Energy Ar + Ion Bombardment with Vacuum Ultraviolet (VUV) Photon Irradiation. *J. Phys. D. Appl. Phys.* **2012**, *45*, 505201.

(22) Ballufi, R. W.; Allen, S.; Carter, C. *Kinetics of Materials*; 2005.

(23) Nunes, R. W.; Martin, J. R.; Johnson, J. F. Influence of Molecular Weight and Molecular Weight Distribution on Mechanical Properties of Polymers. *Polym. Eng. Sci.* **1982**, *22*, 205–228.

Conclusion

The chapters of this dissertation have reported research addressing the major problems facing the application of nanostructured carbon materials, including integration into already existing material systems and controlled synthesis. Novel methods were investigated for coupling carbon nanotubes to polymer matrices,[1] as well as new approaches for controlling the synthesis of graphene[2] and reduced graphene oxide like carbon on copper foils *via* chemical vapor deposition. It was found that carboxylic functionalization of carbon nanotubes was effective in improving the coupling of CNTs to polymer matrices, affecting the thermal transport of the resulting CNT-polymer nanocomposites. From the CVD studies it was established that the cooling phase gases flowed after deposition influence the growth mechanics of graphene on copper foil. Further CVD studies showed that methane may be decomposed directly onto quartz to form reduced graphene oxide like carbon thin films. The obtained thermal characterization results in the CNT thermal study are important for development of CNTs as a filler for composite pastes with high thermal conductivity, and the results of the CVD studies are important for developing further understanding of growth mechanics of bilayer graphene, reduced graphene oxide like carbon and other nanostructured carbon. In addition to the fundamental study of CVD synthesis of graphene and reduced graphene oxide like carbon, this dissertation highlighted engineering of graphene to various applications, including the development of the thinnest flexible transistor with active materials made from all-2D materials,[3] as well as large-scale electron transparent windows, and transparent conducting thin films.

REFERENCES AND NOTES

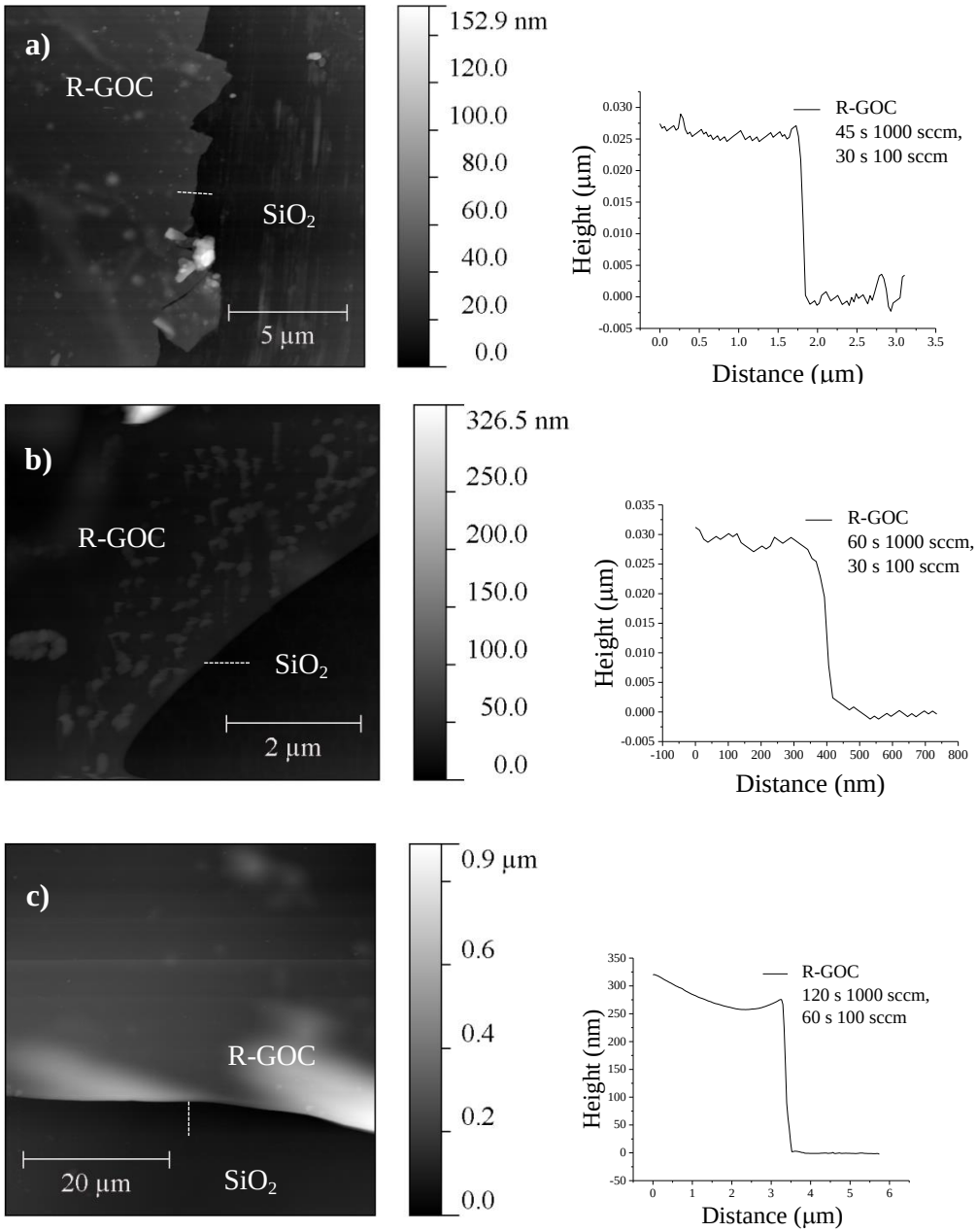
(1) Gulotty, R.; Castellino, M.; Jagdale, P.; Tagliaferro, A.; Balandin, A. A. Effects of Functionalization on Thermal Properties of Single-Wall and Multi-Wall Carbon Nanotube-Polymer Nanocomposites. *ACS Nano* **2013**, *7*, 5114–5121.

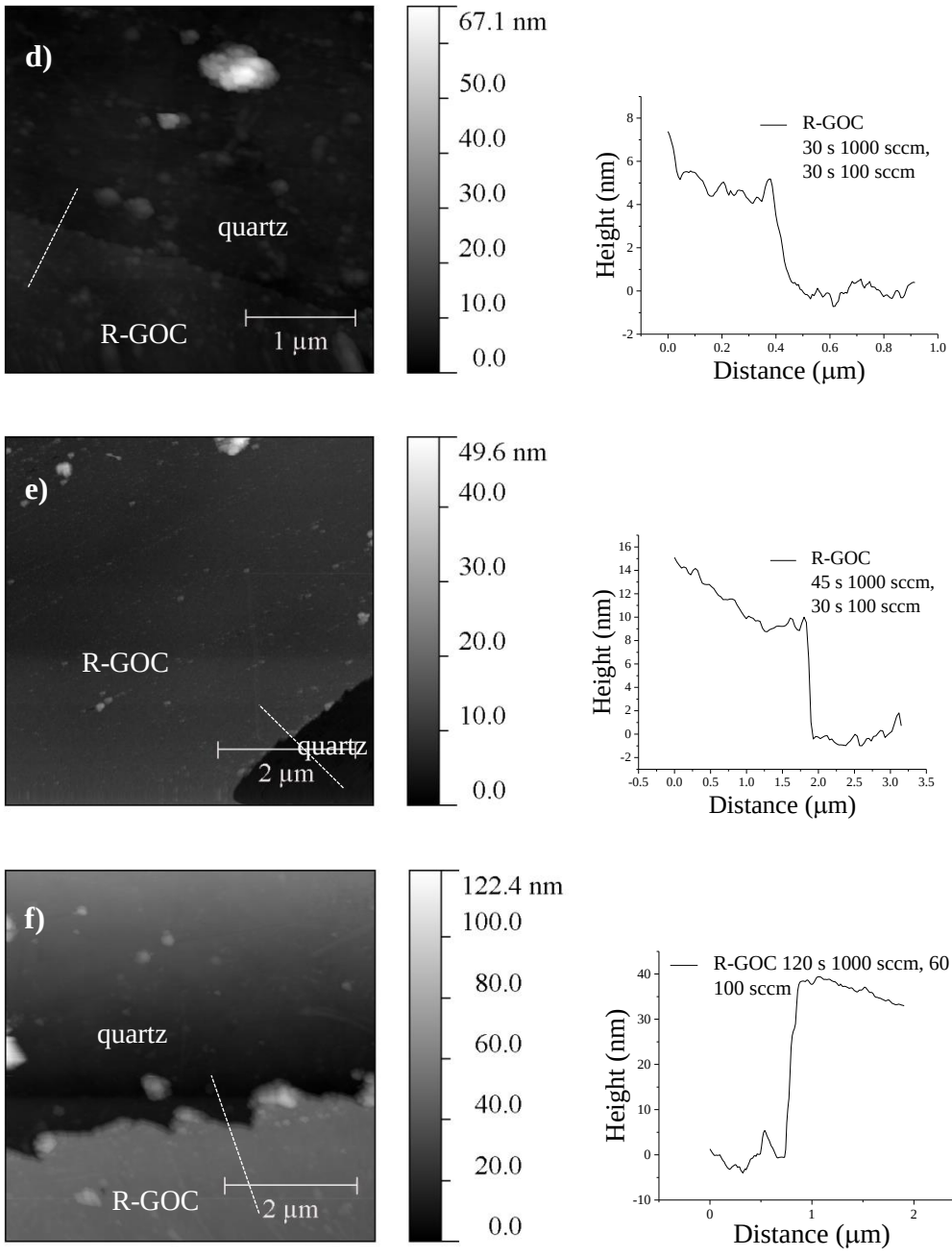
(2) Gulotty, R.; Das, S.; Liu, Y.; Sumant, A. V. Effect of Hydrogen Flow during Cooling Phase to Achieve Uniform and Repeatable Growth of Bilayer Graphene on Copper Foils over Large Area. *Carbon N. Y.* **2014**, *77*, 341–350.

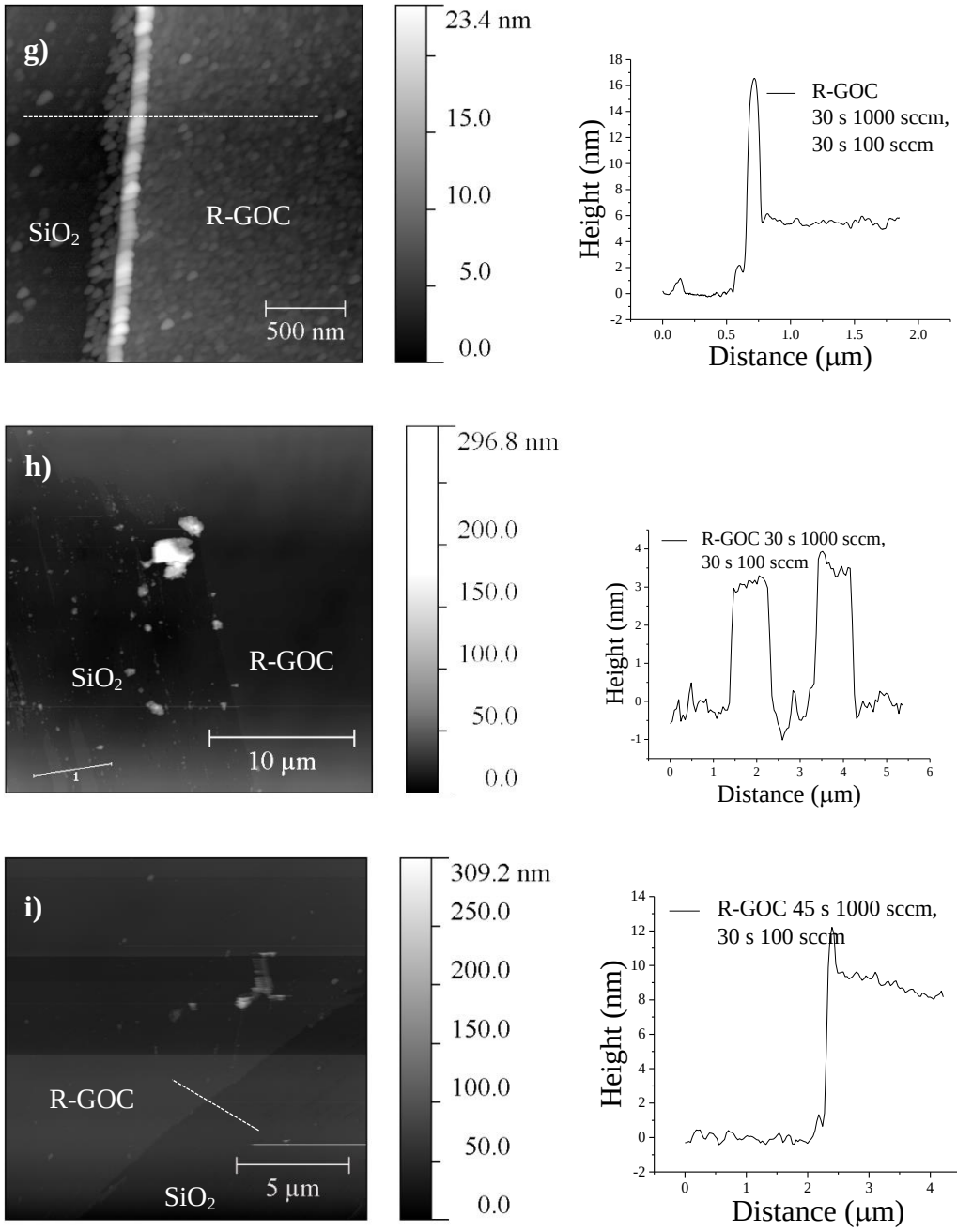
(3) Das, S.; Gulotty, R.; Sumant, A. V; Roelofs, A. All Two-Dimensional, Flexible, Transparent, and Thinnest Thin Film Transistor. *Nano Lett.* **2014**, *14*, 2861–2866.

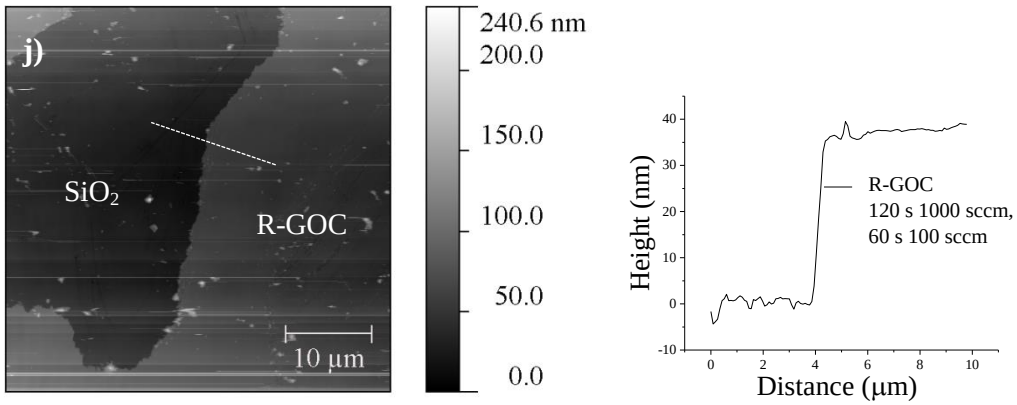
Appendices

Appendix A




d)
quartz
R-GOC
1 μm
67.1 nm
50.0
40.0
30.0
20.0
10.0
0.0
R-GOC
30 s 1000 sccm,
30 s 100 sccm
Height (nm)
Distance (μm)
e)
R-GOC
quartz
2 μm
49.6 nm
40.0
30.0
20.0
10.0
0.0
R-GOC
45 s 1000 sccm,
30 s 100 sccm
Height (nm)
Distance (μm)
f)
quartz
R-GOC
2 μm
122.4 nm
100.0
80.0
60.0
40.0
20.0
0.0
R-GOC 120 s 1000 sccm, 60 s
100 sccm
Height (nm)
Distance (μm)


g)
SiO2
R-GOC
500 nm
23.4 nm
15.0
10.0
5.0
0.0
R-GOC
30 s 1000 sccm,
30 s 100 sccm
Height (nm)
Distance (μm)
h)
SiO2
R-GOC
10 μm
296.8 nm
200.0
150.0
100.0
50.0
0.0
R-GOC 30 s 1000 sccm,
30 s 100 sccm
Height (nm)
Distance (μm)
i)
R-GOC
SiO2
5 μm
309.2 nm
250.0
200.0
150.0
100.0
50.0
0.0
R-GOC 45 s 1000 sccm,
30 s 100 sccm
Height (nm)
Distance (μm)



Appendix A. AFM images of R-GOC films with varying deposition time on Cu substrate, then transferred to SiO_2 substrates (a-c), R-GOC films with varying deposition time deposited directly on quartz substrates (d-f), and R-GOC films with varying deposition time deposited directly on SiO_2 substrates (g-j).